

# Rotating Nuclear Rings and Extreme Starbursts in Ultraluminous Galaxies

D. Downes

Institut de Radio Astronomie Millimétrique, 38406 St. Martin d'Hères, France;  
downes@iram.fr

and

P. M. Solomon

Department of Physics and Astronomy, State University of New York,  
Stony Brook, NY 11794; psolomon@astro.sunysb.edu

to be published, **Astrophysical Journal**, Nov. 10, 1998

Received 28 June 1997 Accepted 12 June 1998

## ABSTRACT

New CO interferometer data show the molecular gas in IR ultraluminous galaxies is in rotating nuclear disks or rings. The CO maps yield disk radii, kinematic major axes, rotation speeds, enclosed dynamical masses, and gas masses. The CO brightness temperatures, the double peaked CO line profiles, the limits on thermal continuum flux from dust, and the constraint that the gas mass must be less than the dynamical mass, all indicate the CO lines are subthermally excited and moderately opaque ( $\tau = 4$  to 10). We fit kinematic models in which most of the CO flux comes from a moderate-density, warm, intercloud medium rather than self-gravitating clouds. Typical ring radii are 300 to 800 parsecs.

We derive gas masses not from a standard CO-to-mass ratio, but from a model of radiative transfer through subthermally excited CO in the molecular disks. This model yields gas masses of  $\sim 5 \times 10^9 M_{\odot}$ ,  $\sim 5$  times lower than the standard method, and a ratio  $M_{\text{gas}}/L'_{\text{CO}} \approx 0.8 M_{\odot}(\text{K km s}^{-1} \text{pc}^2)^{-1}$ . In the nuclear disks, we derive a ratio of gas to dynamical mass,  $M_{\text{gas}}/M_{\text{dyn}} \approx 1/6$  and a maximum ratio of gas to total mass surface density,  $\mu/\mu_{\text{tot}}$ , of  $1/3$ .

For the galaxies **VII Zw 31**, **Arp 193**, and **IRAS 10565+2448**, the CO position-velocity diagrams provide good evidence for rotating molecular rings with a central gap.

In addition to the rotating central rings or disks a new class of star formation region is identified which we call an extreme starburst. They have a characteristic size of only 100 pc. with about  $10^9 M_{\odot}$  of gas and an IR luminosity of  $\approx 3 \times 10^{11} L_{\odot}$  from recently formed OB stars. Four extreme starbursts are identified in the 3 closest galaxies in the sample including Arp 220, Arp 193 and Mrk 273. They are the most prodigious star formation events in the local universe, each representing about 1000 times as many OB stars as 30 Doradus.

In **Mrk 231**, the CO(2–1) velocity diagram along the line of nodes shows a  $1''.2$ -diameter inner disk and a  $3''$ -diameter outer disk. The narrow CO linewidth, the single-peak line profile, the equality of the major and minor axes, and the observed velocity gradients all imply the molecular disk is nearly face-on, yielding low optical and UV extinction to the AGN. Such a geometry means that the molecular disk cannot be heated by the AGN; the FIR luminosity of Mrk 231 is powered by a starburst, not the AGN.

In **Mrk 273**, the CO(1–0) maps show long streamers of radius 5 kpc( $7''$ ) with velocity gradients north-south, and a nuclear disk of radius 400 pc ( $0.6''$ ) with velocity gradients east-west. The nuclear disk contains a bright CO core of

radius 120 pc (0.2").

In **Arp 220**, the CO and 1.3 mm continuum maps show the two “nuclei” embedded in a central ring or disk at p.a.  $50^\circ$  and a fainter structure extending  $7''$  (3 kpc) to the east, normal to the nuclear disk. Models of the CO and dust flux indicate the two  $K$ -band sources contain high-density gas with  $n(\text{H}_2) = 2 \times 10^4 \text{ cm}^{-3}$ . There is no evidence that these sources really are the pre-merger nuclei. They are more likely to be compact, extreme starburst regions containing  $10^9 M_\odot$  of dense molecular gas and new stars, but no old stars. Most of the HCN emission arises in the two “nuclei”. The luminosity to mass ratios for the CO sources in Arp 220 are compatible with the early phases of compact starbursts. There is a large mass of molecular gas currently forming stars with plenty of ionizing photons, and no obvious AGN. The *entire* bolometric luminosity of Arp 220 comes from starbursts, not an AGN.

The CO maps show the gas in ultraluminous IR galaxies is in extended disks that cannot intercept all the power of central AGNs, even if they exist. We conclude that in ultraluminous IR galaxies — even in Mrk 231 that hosts a quasar — the far IR luminosity is powered by extreme starbursts in the molecular rings or disks, not by dust-enshrouded quasars.

*Subject headings:* galaxies: nuclei — galaxies: interstellar matter — galaxies: starburst — galaxies: ISM: dust, extinction — galaxies: individual (Arp 193, Arp 220, Mrk 231, Mrk 273, VII Zw 31) — radio lines: galaxies

## 1. INTRODUCTION

The infrared ultraluminous galaxies are recent galaxy mergers in which much of the gas in the former spiral disks has fallen into the center. The gas re-establishes rotational support at a radius of a few hundred parsecs. This is the same size scale as the Narrow Line Region in active galactic nuclei, and the rotating nuclear disks in some elliptical galaxies. During its infall from 5 kpc to 0.5 kpc, the high-density gas forms many massive stars, as in the early starbursts that formed the bulge stars in protogalaxies at high redshifts. The ultraluminous galaxies we observe in the local universe are re-enacting this primeval process, with a large part of the central mass in gas ready to turn into stars — and ready to fall into a black hole.

The large nuclear concentration of molecular gas in ultraluminous galaxies has been detected in the millimeter lines of CO by many groups during the past decade. Scaling to the signal strengths from Milky Way molecular clouds, however, soon led to a paradox for many of the sources — the estimated gas mass was equal to or larger than the dynamical mass indicated by the linewidths. For Arp 220, for example, Scoville et al. (1991) found that nearly all of the mass in the central few hundred parsecs was in the form of molecular gas. To resolve this dilemma, we showed that in the extreme environment in the central 600 pc of ultraluminous galaxies, much of the CO luminosity must come from an intercloud medium that fills the whole volume, rather than from clouds bound by self gravity, and therefore the CO luminosity traces the geometric mean of the gas mass and the dynamical mass, rather than just the gas mass (Downes, Solomon, & Radford 1993). This allows the nuclear disk gas to be overluminous in CO, relative to self-gravitating clouds in galactic spiral arms. The important linewidth for this calculation is the dynamical linewidth of the galaxy, not that of individual self-gravitating GMCs. The physical basis for estimating gas mass from the CO emission is therefore different from that in Milky Way GMCs. The Milky Way conversion factor is relevant for an ensemble of GMCs in an ordinary spiral galaxy, but not for the center of an ultraluminous galaxy.

In a subsequent survey paper on 37 ultraluminous galaxies observed with the IRAM 30 m telescope (Solomon et al. 1997), we derived the molecular gas mass by several methods. The minimum estimates of the gas mass, for optically thin CO, did indeed reduce the gas mass to much lower fractions of the dynamical mass. The true gas mass must be between the optically thin CO estimate and the dynamical mass, *both* of which are less than the gas mass derived with the Milky Way conversion factor for self-gravitating molecular clouds.

The significance of the lower molecular gas mass is twofold. First, it makes the gas mass smaller than the dynamical mass, as it must be. Second, it means the total molecular gas mass in ultraluminous galaxies is similar to, and not greater than, the molecular mass

in the disk of a gas-rich spiral. It is thus not necessary to force into the nuclear region all the gas in the galaxy —  $\text{H}_2$  and H I. The nuclear starbursts can be fed by pre-existing molecular gas that falls into the central few hundred parsecs from an original radius of a few kiloparsecs, and not from the outer H I disk.

These ideas show that the kinematics of the nuclear gas is critical to understanding both the evolution of ultraluminous galaxies and the molecular line formation. The CO emissivity per unit gas mass surface density is not constant, but varies with position in the nuclear disk. A more correct treatment requires radiative transfer modeling, with kinematic data from millimeter interferometers.

To carry out this next step in our study of molecular gas disks at the centers of IR ultraluminous galaxies, we made high-resolution CO maps with the IRAM interferometer. We chose sources from our CO survey, concentrating on the nearest ultraluminous galaxies in the northern sky, for which we already had accurate measurements of the total flux, linewidth, and radial velocity. The new observations give accurate positions, line and continuum fluxes at the interferometer resolution, images, directions of the kinematic major axes, and radii of the nuclear disks.<sup>1</sup> These radii and the velocity extrema give the enclosed dynamical mass. The velocity data allow modeling of the kinematics and the CO brightness temperature versus radius. For most sources, the CO data indicate the gas kinetic temperature is higher than in typical Galactic molecular clouds, but the CO is subthermally excited, turbulent, and warm, quite unlike the molecular clouds in galaxy-scale disks. At the positions of maximum CO intensity in the disks, the CO lines are moderately opaque, with optical depth  $\tau(1-0) \approx 4$  to 10, but in other parts of the disk, the CO lines can be optically thin. The result is that the molecular gas mass is about a factor of five lower than it would be if the CO emission came from self-gravitating clouds. The rest of the dynamical mass is accounted for by young stars that provide the luminosity and older stars that were already in the central bulge before the merger.

We argue that the bright spots in the ultraluminous galaxies are compact extreme starburst regions that occur in the dense gas traced by HCN and CS emission. They produce most of the HCN luminosity, and 1mm dust continuum while the more diffuse gas in the nuclear disks dominates the CO luminosity. These compact extreme starburst regions which we identify in Arp 193, Arp 220 and Mrk 273 are the most prodigious star formation events in the local universe. There are undoubtedly many more too compact to be resolved.

The plan of this paper is as follows. Section 2 describes the observations and summarizes the parameters obtained by direct measurement. Section 3 introduces our

---

<sup>1</sup>In this paper, distances are for  $H_0 = 75 \text{ km s}^{-1} \text{ Mpc}^{-1}$  and  $q_0 = 0.5$ .

model of a turbulent rotating disk and discusses the derivations of the rotation curve, disk radius, disk height, turbulent velocity, gas mass, and dynamical mass obtained by fitting the model disk to the data. Sections 4 through 8 present the results on the galaxies with CO(2–1) data, obtained with sub-arcsecond resolution. These galaxies are VII Zw 31, Mrk 231, Arp 193, Mrk 273, and Arp 220. Section 9 gives the results on five additional ultraluminous galaxies mapped in CO(1–0) only. Section 10 discusses the source sizes, gas masses, the ratio of gas mass to dynamical mass, and the mass of young stars needed to power the starburst. Section 11 contains our conclusions.

## 2. OBSERVATIONS AND RESULTS

CO(1–0) and (2–1) were observed with the IRAM interferometer on Plateau de Bure, France (Guilloteau et al. 1992). Three to four configurations of the four 15 m antennas gave baselines from 24 to 410 m for VII Zw31, Mrk 231, Mrk 273, and Arp 220, and 24 to 288 m for the other sources. The SIS mixers had receiver temperatures of 60 – 80 K, and operated single sideband at 3 mm and double sideband at 1.3 mm with system temperatures of 200 and 400 K, respectively. The spectral correlator covered a 500 MHz band at 2.5 MHz resolution, giving velocity ranges of  $1300 \text{ km s}^{-1}$  at  $7 \text{ km s}^{-1}$  resolution at 3 mm, and  $700 \text{ km s}^{-1}$  at  $3.4 \text{ km s}^{-1}$  resolution at 1.3 mm. For analysis, we smoothed the data to 20 and  $40 \text{ km s}^{-1}$ . Amplitude and phase were calibrated relative to quasars and the flux scale was adopted from same-epoch measurements of quasars and planets with the interferometer and the IRAM 30 m telescope. The beamwidths (FWHM) were  $1''$  to  $3''$  at CO(1–0) and  $0''.5$  to  $1''$  at CO(2–1). Table 1 summarizes the observing parameters.

Table 2 lists CO source positions and integrated CO line fluxes from the interferometer. We also list the CO line fluxes from the 30 m telescope (Radford, Solomon, & Downes 1991a; Solomon et al. 1997). Table 3 lists sizes from Gaussian fits to the CO visibilities. Sources observed in CO(1–0) and (2–1) had the same sizes in both lines. The visibility fits are independent of the synthesized beam or the CLEAN algorithm, and there is no need to deconvolve an apparent size on a map. The phase calibration can broaden a source due to the baseline error, varying as  $2\pi\lambda/D$  times the angle between the source and its phase calibrator ( $\lambda =$  wavelength,  $D =$  baseline). For sources and calibrators in this paper, the broadening is  $< 0.1$  beamwidth. After correcting for atmospheric decorrelation, we obtained sizes  $< 0''.2$  for the quasar calibrator sources.

## 3. DISK MODELS

### 3.1. Geometry of Nuclear Disks from Kinematic Data

CO surveys of our Galaxy show most of the gas in the inner  $R < 5$  kpc is in  $\sim 6000$  giant molecular clouds (GMCs) of diameter  $\sim 50$  pc and  $\text{H}_2$  density  $150 \text{ cm}^{-3}$ . In an ultraluminous IR galaxy merger, these clouds fall into the central  $R \sim 500$  pc, forming a disk of height  $\sim 50$  pc. Because the GMCs' density is too low to stabilize them against tidal shear at the merger's center, and because the new volume is ten times smaller than the original volume of all the GMCs in the galactic disk, the GMCs lose their identity and blend into a continuous medium with a mean  $\text{H}_2$  density  $\sim 10^3 \text{ cm}^{-3}$ . We therefore modeled the nuclear disks as a continuous medium rather than an ensemble of individual clouds.

We used the CO spectral data to estimate how much of the gas was in a high-density, inner ring or disk and how much in a lower-density, outer disk. To simulate the observed spectra and position-velocity diagrams, we modified a model for rotating disks developed by A. Dutrey (see Dutrey, Guilloteau, & Simon 1994). This model has an inner disk of high-density gas between radii  $R_{\min}$  and  $R_1 = R_{\min} + \Delta R$ , and an outer disk of lower-density gas between radii  $R_{\min}$  and  $R_{\max}$ . The  $\text{H}_2$  density between  $R_{\min}$  and  $R_{\max}$  is

$$n(R) = n_0 A \exp \left[ -4 \ln 2 \left( \frac{R - R_{\min}}{\Delta R} \right)^2 \right] + n_0 R^\alpha \quad , \quad (1)$$

where the inner disk is the Gaussian of width  $\Delta R$  (FWHM), and the outer disk is the power law. We fit the outer disks with constant density ( $\alpha = 0$ ). Our beams cannot distinguish between a ring and a filled disk, so for most sources, we took  $R_{\min} = 0$ . Because of the radiative transfer through the rotating, inclined disk, the predicted CO map looks like a ring, even if there is gas in to  $R = 0$ . For the galaxies VII Zw 31, Arp 193, and IRAS 10565+2448, the position-velocity diagrams are better fit with ring models, with  $R_{\min} = R_0$ , rather than filled disk models. Table 4 gives the source geometry, derived as follows:

*Line of nodes:* The visibility fits in individual spectral channels gave position offsets vs. velocity, which showed the direction of the kinematic major axis. We checked the angle of the line of nodes from channel maps and isovelocity contour maps. Errors are  $\pm 10^\circ$ .

*Rotation curve turnover radius  $R_0$ :* In the data, the position-velocity diagrams along the kinematic major axis often have two peaks near the source center. In our models, twin peaks occur near the points where the rotation curve turns over and becomes flat. The observed offsets of the two intensity peaks on the major axis were tried as first guesses for the rotation curve turnover radii  $R_0$ . Model fits converged close to these values. In angular units, the uncertainties are  $\sim \pm 0''.1$ . In our models,  $R_0$  is the projected radius with the largest gas column density at the same line-of-sight velocity, and the highest flux. For most of the sources, the solid angle inside this zone is too small to affect the maps, even if the

gas is really in a filled disk rather than a ring.

*Inner disk half-intensity radius,  $R_1 = R_{\min} + \Delta R$ :* In our models, most of the CO flux comes from the high-density inner disk. The extent of the central double peak in the position-velocity diagrams constrained the radial width  $\Delta R$ , which we varied until the model position-velocity diagrams matched the data. The uncertainty in  $\Delta R$  is  $\sim \pm 0''.2$

The *outer radius,  $R_{\max}$ ,* of the low-density disk was taken to be the observed CO maximum extent on the line of nodes.

*Disk thickness  $H$ :* Along the  $z$ -axis perpendicular to the equatorial plane, the gas volume density  $n(z)$  near  $z = 0$  was approximated by a gaussian with full width to half-maximum  $H$ . For a disk with a flat rotation curve, the disk's thickness can be estimated with the Mestel formula (Mestel 1963; see also Binney & Tremaine 1987):

$$H(R) = 1.4 \sigma(R) \left( \frac{R}{V_{\text{rot}}} \right) \left[ 1 + \frac{\rho_{\text{gas}}}{\rho_1} \left( 1 - \frac{H}{2R} \right) \right]^{-0.5}, \quad (2)$$

where  $\sigma$  is the 1-D velocity dispersion (assumed independent of  $z$ ) and  $\rho_1(R)$  is the total mass density (gas plus stars) in an equivalent sphere with a flat rotation curve. This equivalent density, in  $M_{\odot} \text{pc}^{-3}$ , is related to the rotation velocity, in  $\text{km s}^{-1}$ , through the usual integral for dynamical mass,  $\rho_1(R) = 18.5(V_{\text{rot}}/R)^2$ . We dropped the second-order term and estimated the disk thickness as

$$H \approx 1.4 \sigma(R) \left( \frac{R}{V_{\text{rot}}} \right) \left[ 1 + \frac{\rho_{\text{gas}}}{18.5} \left( \frac{R}{V_{\text{rot}}} \right)^2 \right]^{-0.5}, \quad (3)$$

where  $H$  and  $R$  are in pc,  $V_{\text{rot}}$  is in  $\text{km s}^{-1}$ ,  $\rho_{\text{gas}}$  is in  $M_{\odot} \text{pc}^{-3}$ . Because the velocity dispersion decreases with distance from the center, our model disk thickness tends to a constant value. In reality, the molecular disks are warped and twisted, and their shape depends on the merger's infall history.

### 3.2. Rotation Curves

We combined our density models with rotation curves that reproduced the observed channel maps, position-velocity diagrams, spectral profiles, interferometer visibilities, and line intensities. We took the rotation velocity to be

$$V_{\text{rot}}(R) = V_0 \left( \frac{R}{R_0} \right)^{\beta}, \quad (4)$$

with  $\beta = 1$  for  $R < R_0$  and  $\beta = 0$  for  $R_0 \leq R \leq R_{\max}$ , that is, the curve rises from the center and flattens after  $R_0$ . Most of the derived values of  $R_0$  are smaller than our beam, so more elaborate rotation curves are not justified for now.



For the *inclination*,  $i$ , we started from the major/minor axis ratio of the integrated CO source, with  $i = \cos^{-1}(\text{minor}/\text{major})$ , and then varied the inclination to match the position-velocity data and to ensure the derived gas mass was less than the dynamical mass. The nuclear rings or disks may not be circular; they may be elliptical, analogous to  $x_2$  orbits at the center of a barred galaxy. The inclination  $i$  listed in Table 5 should be interpreted in the sense  $\sin i = \sin I \cos \phi$ , where  $I$  is the true inclination of the disk relative to face-on, and  $\phi$  is the azimuth of the major axis of the ellipse, if there is one. With our current beams, we cannot tell the difference between circular and elliptical orbits.

For the *rotation velocity*,  $V_0$ , we first guessed the apparent speed,  $V_0 \sin i$ , to be half the velocity range of the twin CO peaks on the major axis. The best fits were close to these values, giving 200 to 300  $\text{km s}^{-1}$  (corrected for inclination) on the flat part of the curve (Table 5). This is an equivalent circular velocity if the orbits are elliptical.

The *turbulent velocity*,  $\Delta V$ , of the gas was taken from the model fit, not from the observed line profiles, which include both turbulent broadening and the rotational velocity gradient in the beam. Rotation alone cannot explain the observed profiles. We need a local, turbulent line broadening as well. The models actually constrain this parameter rather well. We assumed the local line broadening had the form

$$f(V - V_0) = \exp \left[ - \left( \frac{V - V_0}{\Delta V} \right)^2 \right] \quad (5)$$

where  $\Delta V$  is the local line halfwidth to the  $1/e$  level ( $\Delta V = 0.6 \times \text{FWHM} = 1.4\sigma$ , where  $\sigma$  is the r.m.s. velocity dispersion along the line of sight). The radiative transfer model included the local linewidth at each point and the rotational velocity versus radius. We iterated the model fits until the local turbulence and the rotational velocity gradient — convolved with our beam — matched the observed position-velocity diagrams and the observed line profiles. Turbulent velocities  $\Delta V$  that fit the data were 30 to 140  $\text{km s}^{-1}$ , with some of the position-velocity diagrams indicating lower turbulence at greater radii from the nucleus. At the rotation curve turnover point  $R_0$ , the values of  $\Delta V$  correspond to local FWHM linewidths of 70 to 230  $\text{km s}^{-1}$ , so the nuclear disks are highly turbulent.

### 3.3. CO line parameters

After deriving sizes and velocities from the data, we adjusted our models to match the observed CO line intensities. As a first guess, we set the gas kinetic temperature equal to the dust temperature derived from blackbody fits to the IRAS fluxes. At the gas densities in our models, collisions cannot raise the CO excitation temperature to the gas kinetic temperature, nor populate the CO levels thermally. Instead, there are

different excitation temperatures for each transition. The line brightness temperatures, excitation temperatures, and gas kinetic temperatures are in the sense  $T_b < T_{\text{ex}} < T_{\text{kin}}$ , with  $T_{\text{ex}}(2-1) < T_{\text{ex}}(1-0)$ . We therefore assumed the CO level populations were determined by the local gas kinetic temperature, density, and velocity gradient, and we calculated, with an escape probability program, CO column densities per unit velocity width for a local velocity gradient of  $1 \text{ km s}^{-1} \text{ pc}^{-1}$  and a  $[\text{CO}/\text{H}_2]$  abundance of  $8 \times 10^{-5}$ , both typical of Milky Way molecular clouds. For these values, the escape probability method yields the following non-LTE excitation temperatures  $T_{\text{ex}}$ :

$$T_{\text{ex}}(1-0) = 0.186 n^{0.622} T_{\text{kin}}^{0.240} \quad (6)$$

$$T_{\text{ex}}(2-1) = 0.117 n^{0.678} T_{\text{kin}}^{0.247} \quad , \quad (7)$$

where  $n$  is the  $\text{H}_2$  number density in  $\text{cm}^{-3}$ , and  $T_{\text{kin}}$  is the gas kinetic temperature in K. These formulae are valid for  $50 < T_{\text{kin}} < 150 \text{ K}$  and  $100 < n < 3000 \text{ cm}^{-3}$ .

We then calculated the radiative transfer on the lines of sight through the disk (eqs. 7 & 8 of Dutrey et al. 1994), convolved the computed map with our beam, and adjusted the parameters to match the observed brightness temperatures. Highest CO opacity occurs at the rotation curve turnover radius,  $R_0$ , which yields the largest column density at the same line-of-sight velocity. Table 6 gives the best-fit model CO(1–0) excitation temperatures and gas densities, and Tables 7 and 8 give the model CO(1–0) and (2–1) line opacities and Rayleigh-Jeans brightness temperatures. We also ran models for higher density gas, with excitation temperatures closer to the kinetic temperatures, but these models gave too much CO and dust flux, and did not reproduce the position velocity diagrams.

At the rotation curve turnover radius  $R_0$ , our models yield CO(1–0) opacities of 2 to 8. These mean opacities apply to smoothly distributed gas. The model of subthermal excitation yields the observed CO(2–1)/(1–0) ratios of 0.6 to 1.0 (Radford et al. 1991a). In the lower-density, outer disks detected in these sources, the volume-averaged densities in the model are too low to yield detectable CO lines. For these outer disks, our model must be corrected with an area filling factor for molecular clouds, as in CO maps of disks of normal galaxies. For the mean values for the outer disks in Table 6, we adopted a volume filling factor of 0.1, an area filling factor of 0.3, and local gas densities 10 times higher than the volume-averaged values listed in the Table.

### 3.4. Gas Mass and Dynamical Mass

We used the CO parameters to estimate the gas mass and the dynamical mass *vs.* radius (Table 9). After we found a density law that reproduced the observed brightness

temperatures, we integrated over the source to get the gas mass. These masses are for a  $[\text{CO}/\text{H}_2]$  abundance of  $8 \times 10^{-5}$ , as in molecular clouds in our Galaxy. For the sources observed here, it is difficult to lower the model CO abundance below the Milky Way value. Keeping the same CO line intensity at a lower CO abundance would force us to make the gas mass bigger than the dynamical mass, invalidating the model.

The dynamical masses were taken to be  $RV_{\text{rot}}^2/G$ , where  $V_{\text{rot}}$  is the rotation speed listed in Table 5. Most of the sources have flat rotation curves, so the dynamical mass increases linearly with radius. Table 9 lists the ratio of gas mass to dynamical mass in the inner, high-density disk alone (to the radius  $R_1$  in Table 4) and in the inner and outer disks together (to the radius  $R_{\text{max}}$  in Table 4). Relative to our assumed Hubble constant, the gas mass scales as  $H_0^{-2}$ , the dynamical mass as  $H_0^{-1}$  and their ratio as  $H_0^{-1}$ .

We also list in Table 9 the maximum ratio of gas to total (gas + stars) surface density in our models. We calculated the ratio of gas to total mass surface density,  $\mu/\mu_{\text{tot}}$ , in 15 bins in radius, and found maximum values of  $\sim 1/3$  to  $1/4$ , midway between the rotation curve turnover radius  $R_0$  and the half-intensity radius  $R_1$ . The models in this paper are for the distributed gas, but there is also denser gas in star-forming cores that give rise to HCN and CS lines. Most of the CO flux comes from the distributed medium, but our gas masses may have to be corrected upward to allow for the cores, depending on future interferometer results in the dense-gas tracer lines. We return to this point in the Discussion section.

### 3.5. Dust Continuum Flux

We used the model gas mass to predict the dust flux, from

$$S(\nu_{\text{obs}}) = (1 + z)\kappa(\nu_r)MD_L^{-2}B(\nu_r, T_d) \quad , \quad (8)$$

where  $S$  is the dust continuum flux density,  $\nu_{\text{obs}}$  and  $\nu_r$  are the observed and rest-frame frequencies,  $M$  is the *gas* mass,  $D_L$  is the luminosity distance,  $B$  is the Planck function, and  $T_d$  is the dust temperature. We took the dust temperatures from our fits to the IRAS fluxes (Solomon et al. 1997) — the same as the gas temperatures in Table 6 — and we used a dust mass absorption coefficient  $\kappa(\nu_r) = 0.1 \times \nu^n$ , where  $\nu_r$  is in THz,  $\kappa$  is in  $\text{cm}^2 \text{gm}^{-1}$  of interstellar matter, and we took the index  $n = 1.5$ . At 230 GHz, this absorption coefficient is  $\kappa = 0.011 \text{ cm}^2 \text{ gm}^{-1}$  of interstellar matter, or, for a gas-to-dust mass ratio of 100,  $\kappa_d = 1.1 \text{ cm}^2 \text{ gm}^{-1}$  of dust, as in previous estimates for dense molecular clouds (see Krügel & Siebenmorgen 1994, their Fig. 12). The predicted thermal fluxes from dust are then

$$S(\nu_{\text{obs}}) = 6.4 \times 10^{-7}(1 + z)M D_L^{-2} T_d \nu_r^{2+n} \quad , \quad (9)$$

where flux density  $S$  is in Jy, gas mass  $M$  is in  $M_{\odot}$ , luminosity distance  $D_L$  is in Mpc, dust temperature  $T_d$  is in K, and rest frequency  $\nu_r$  is in THz. The predicted thermal dust fluxes at 2.6 and 1.3 mm are compared with the observed fluxes in Table 10.

Four sources, VII Zw 31, Mrk 231, Mrk 272, and Arp 220, were observed in both the CO(1–0) and (2–1) lines, and on the longest baselines of 410 m. Because we have better angular resolution for these sources, we discuss them in more detail than our other sources.

#### 4. VII Zwicky 31

This source, catalogued by Zwicky (1971), was identified by Fairclough (1986) as an ultraluminous IR galaxy. Its optical surface brightness profiles resemble those of elliptical galaxies and its optical line ratios fit a starburst rather than an AGN (Djorgovski, de Carvalho, & Thompson 1990). Sage & Solomon (1987) found this source had one of the highest known CO luminosities and deduced that the molecular gas was a large part of the dynamical mass. Scoville et al. (1989) showed the CO source had a radius  $< 3.8$  kpc.

The CO maps of the galaxy VII Zw 31 are the best evidence in our sample for a rotating ring. Models that best fit the data are those with a minimum ring radius  $R_{\min}$  in eq.(1) equal to  $R_0 = 290$  pc. Filled-disk models, with  $R_{\min} = 0$ , give poorer fits, with much less contrast. In  $40 \text{ km s}^{-1}$ -wide channel maps, the CO peak migrates from south to north with increasing velocity (Fig. 1). The source is resolved east-west, perpendicular to the kinematic major axis. This indicates the source is inclined, but more face-on than edge-on. Our modeling gives a good fit to the data for a ring inclined at  $20^\circ$  to face-on. Figure 2 shows the maps of integrated intensity and isovelocity contours across the source in both CO lines. The total CO(1–0) flux measured with the interferometer is equal to the flux obtained at the 30 m telescope (Radford et al. 1991a). At CO(2–1), the source is partially resolved out, and the flux from the interferometer is only half the single-dish flux. In channels off the CO line, the continuum flux is  $< 2 \text{ mJy}$  at 109 GHz and  $< 10 \text{ mJy}$  at 221 GHz. This limit on any thermal dust flux is consistent with the gas mass of  $1.1 \times 10^{10}$  deduced from the CO luminosity, for a dust temperature  $< 50$  K.

The CO velocity contours in Fig. 2 indicate the north-south velocity gradient. In the position-velocity diagrams (Fig. 3) there is a  $200 \text{ km s}^{-1}$  velocity shift over  $4''$  north-south. The model in the Tables reproduces well the observed diagrams, the CO profiles across the source, the channel maps, and the observed line intensities. The CO spectra (Fig. 4) have twin peaks separated by  $\pm 70 \text{ km s}^{-1}$ . The blue and redshifted CO peaks are respectively  $0''.65$  south and north of the source centroid. The line profiles are remarkably

symmetric along the north-south kinematic major axis. The CO line of nodes differs from the northwest-southeast dust lane found by Djorgovski et al. (1990) on a  $10''$  scale by subtracting a model from their optical images.

## 5. Markarian 231

The Seyfert I galaxy Markarian 231 has an IR luminosity of  $3.3 \times 10^{12} L_{\odot}$  (e.g., Sanders et al. 1987). Most of the power is emitted at the center of a major galaxy merger which has tidal tails extending over 75 kpc (Cutri, Rieke, & Lebofsky 1984; Hutchings & Neff 1987; Sanders et al. 1987). Optical spectroscopy indicates stars formed in the past 1 Gyr over a widespread region (10–15 kpc). In this large extranuclear region the H $\alpha$  emission comes from shocks rather than stellar photoionization (e.g., Hamilton & Keel 1987; Lipari, Colina, & Macchetto 1994). The best previous CO study is that by Bryant & Scoville (1996), who found an east-west velocity gradient in the CO source. Our higher-sensitivity results have a factor of two better resolution than their study, and not only confirm the velocity gradient, but also distinguish the inner and outer disks in the position-velocity diagrams.

### 5.1. CO in Mrk 231’s molecular disk

In contrast to the large optical extent, the CO source is very compact, on a scale twenty times smaller in radius. In  $40 \text{ km s}^{-1}$  channel maps in CO(1–0) and (2–1), the line peak shifts from west to east with increasing velocity (Fig. 5). The gradient is clearly shown on the CO isovelocity maps (Fig. 6). The CO(2–1) intensity contours (Fig. 6) are symmetric and only slightly broader than the beam. The CO(2–1) position-velocity diagram along the line of nodes (Fig. 7) shows an inner nuclear disk of diameter  $1''.2$  (radius 460 pc) and a  $3''$  outer disk with a lower velocity gradient. The asymmetric CO(2–1) line profiles  $0''.4$  from the center of the galaxy (Fig. 8) are a characteristic signature of a rotating nuclear disk. The maximum linewidth in both CO lines is  $190 \text{ km s}^{-1}$  FWHM, which is narrow for ultraluminous galaxies.

The CO data imply the molecular disk is face-on, for three reasons. 1) The CO major and minor axes are nearly equal, indicating an inclination  $i \leq 20^\circ$ . 2) To reproduce the single-peaked CO profile, narrow CO linewidth, and observed velocity gradients, our model disks must be within  $20^\circ$  of face-on. For  $i \geq 20^\circ$  to face-on, the gas mass would exceed the dynamical mass. 3) The CO does not absorb the nuclear continuum source at any velocity. This agrees with the CO disk being face-on, leaving the Seyfert I nucleus unobscured. For

$i = 10^\circ$  to face-on, the true rotation velocity would be  $345 \text{ km s}^{-1}$ , the same as we deduce for Arp 220. If the disk were even more face-on, the observed velocity gradient would imply a rotation speed  $> 400 \text{ km s}^{-1}$ , higher than in all the other galaxies in our sample, which seems unlikely. We adopt  $i = 10^\circ$  and  $V_{\text{rot}} = 345 \text{ km s}^{-1}$ , although the kinematic data alone would also allow a rotation velocity of  $250 \text{ km s}^{-1}$ .

In CO, we do not detect the gas emitting in the 1667 MHz OH megamaser with  $760 \text{ km s}^{-1}$  linewidth (Staveley-Smith et al. 1987). nor do we detect anything at the IR source  $3''.5$  south of the nucleus, to a limit of  $5 \text{ mJy}$  in  $40 \text{ km s}^{-1}$  channels (see also Bryant & Scoville 1996). Armus et al. (1994) interpreted the southern IR source as the nucleus of the merger partner, but recent HST images show this feature to be a dense arc of star-forming knots (Surace et al. 1998). In any case, it is very weak in both CO and the mm continuum.

In the center of Mrk 231, the AGN is detected by centimeter wavelength VLBI as a variable, nonthermal radio continuum source with a size  $< 1 \text{ pc}$  (Preuss & Fosbury 1983; Neff & Ulvestad 1988; Lonsdale, Smith, & Lonsdale 1993; Taylor et al. 1994). New VLBA images at 1.4 GHz resolve this nonthermal source into a nuclear core with pc-scale lobes. Carilli, Wrobel & Ulvestad (1998) subtracted their VLBA map from a VLA map and found an  $0''.4$  nonthermal nuclear disk source that emits half the nuclear flux, the rest coming from the core and the pc-scale lobes.

At millimeter wavelengths, outside the CO line channels, we detect an unresolved (size  $< 0''.1$ ) nonthermal, mm continuum source at the nucleus, which is probably the nonthermal VLBA core. The mm continuum source and the CO centroid both coincide with the 8.44 GHz continuum source (Condon et al. 1991).

## 5.2. Mrk 231's Luminosity: 2/3 Starburst, 1/3 AGN

The CO kinematic data for the central 1 kpc of Mrk 231 and our model of a face-on disk show the far-IR luminosity comes from a starburst, not a black hole accretion disk. We assume the central UV-to-FIR continuum has three components: the visible and UV continuum is blackbody flux from the AGN accretion disk, the  $2\mu\text{m}$  peak is blackbody flux from a dusty AGN torus, and the far-IR peak is blackbody flux from the molecular disk. The extinction to the accretion disk is low,  $A_V = 2 \text{ mag}$ , because both the dusty torus and the larger-scale molecular disk are face-on.

*The accretion disk's luminosity* may be derived from the UV and visible fluxes and the extinction to the Seyfert I nucleus. The UV fluxes measured by IUE and HST are  $2 \times 10^{-15} \text{ erg s}^{-1} \text{ cm}^{-2} \text{ \AA}^{-1}$  (Schmidt & Miller 1985; Hutchings & Neff 1987; Smith et al.

1995). A blackbody with this flux, corrected for a UV extinction of 5 mag (Smith et al. 1995) and a distance of 170 Mpc, has a UV luminosity of  $4 \times 10^{11} L_{\odot}$ . For an accretion disk temperature of 20000 to 30000 K, as in the models of Malkan & Sargent (1982) and Sanders et al. (1989), the blackbody peaks at 2000 to 1000 Å, and has a radius of  $1 \times 10^{-3}$  pc. This result is consistent with the optical continuum, which has  $A_V = 2$  mag and an intrinsic magnitude  $M_V = -25.1$  (luminosity  $5 \times 10^{11} L_{\odot}$ ; Boksenberg et al. 1977).

*The dusty torus' luminosity* may be derived from the near-IR continuum. As in other Seyfert I galaxies, the  $2\mu\text{m}$  bump is well fit by a 1470 K blackbody, close to the dust sublimation point (Kobayashi et al. 1993). The flux at the  $2\mu\text{m}$  bump,  $9.3 \times 10^{-11} \text{ erg s}^{-1} \text{ cm}^{-2} \mu\text{m}^{-1}$ , corrected for an IR extinction of 0.2 to 0.6 mag (Krabbe et al. 1997), implies a blackbody luminosity of  $(3 \text{ to } 4) \times 10^{11} L_{\odot}$ , and a radius of 0.18 pc. The compact 10 to  $25 \mu\text{m}$  source in Mrk 231 (Matthews et al. 1987; Keto et al. 1992; Miles et al. 1996) arises farther out in the dusty torus, where the dust temperature is  $\sim 200$  K, at a radius of  $\sim 10$  pc from the AGN. This dusty torus is heated by the AGN. If its thickness is equal to its radius, then the torus absorbs half the AGN's power, so the AGN's total luminosity is 6 to  $9 \times 10^{11} L_{\odot}$ , the same as estimated from the optical and UV flux.

*The molecular disk's FIR luminosity* may be derived from the IRAS fluxes, and is  $2 \times 10^{12} L_{\odot}$  (e.g., Solomon et al. 1997). The molecular disk has a dust optical depth close to unity at  $100 \mu\text{m}$  and causes the deep  $10\mu\text{m}$  silicate absorption (Allen 1976; Rieke 1976; Roche, Aitken, & Whitmore 1983). The blackbody radius calculated from the FIR luminosity is 200 pc, half the measured size of the molecular disk. The molecular disk receives some heat from the dusty torus. With the thickness-to-radius ratio in our CO model, it would intercept half of the power, or  $2 \times 10^{11} L_{\odot}$  of re-processed radiation from the AGN. Since this is only 10% of the FIR luminosity, most of the FIR luminosity of Mrk 231 must come from the starburst in the molecular ring or disk. A similar model was used by Rigopoulou, Lawrence, & Rowan-Robinson (1996) to fit the FIR continuum spectrum.

Our CO model fit gives a gas mass of  $3.1 \times 10^9 M_{\odot}$  — equal to the mass of all the molecular gas in the Milky Way — in a high-density disk between  $R = 76$  and 850 pc. There is another  $0.9 \times 10^9 M_{\odot}$  of gas in a lower density outer disk extending to a radius of 1.7 kpc. The high-density molecular disk is the region observed in  $\text{H}_2$  at  $2 \mu\text{m}$  by Krabbe et al. (1997). The brightest  $\text{H}_2$  line is 200 pc from the nucleus, in the molecular disk, so the low  $2 \mu\text{m}$  extinction on the line of sight to the nucleus itself does not apply to the  $\text{H}_2$  flux.

Our conclusion that most of Mrk 231's FIR luminosity comes from a starburst can be checked for consistency (Table 11). We assume the new stars in the burst,  $M_{\text{new}\star}$ , yield  $L_{\text{FIR}}/M_{\text{new}\star} \approx 500 L_{\odot} M_{\odot}^{-1}$ , a luminosity ratio that can be attained in a fast starburst (Leitherer & Heckman 1995). Dividing this ratio into the FIR luminosity yields  $M_{\text{new}\star}$ ,

from which we then calculate  $M_{\text{old}\star} = M_{\text{dyn}} - M_{\text{gas}} - M_{\text{new}\star}$ , where  $M_{\text{old}\star}$  is the mass of old stars in the nuclear bulge before the merger. For the region  $R \leq 460$  pc in Mrk 231, the rotation velocity inferred from our CO data yields a dynamical mass  $M_{\text{dyn}}(< 460 \text{ pc}) = 12.7 \times 10^9 M_{\odot}$ , and our CO model yields  $M_{\text{gas}} = 1.8 \times 10^9 M_{\odot}$ . The consistency check then yields  $M_{\text{old}\star} = 7.1 \times 10^9 M_{\odot}$ , which is about the same as the mass of old stars in a similar radius in the Milky Way (e.g., Oort 1977). Because of our assumed  $L/M$ , the derived stellar masses in the starburst and the bulge are uncertain by at least a factor of two. Our point is simply that with a starburst powering the FIR luminosity, all the gas and stellar masses are quite plausible. In summary, we think Mrk 231’s black hole accretion disk emits  $\sim 1 \times 10^{12} L_{\odot}$ , or  $\sim 30\%$  of the total bolometric luminosity. Most of the luminosity,  $\sim 2 \times 10^{12} L_{\odot}$ , comes from the starburst in the molecular ring or disk.

## 6. Arp 193

The ultraluminous merger Arp 193 shows two tidal tails in the visible and the near IR (Smith et al. 1995, 1996). The IR images show a single, elongated nucleus, but cm-radio continuum maps show two sources separated by  $1''$ . Strong lines of Br $\gamma$  and H $_2$  are seen in  $K$  band (Goldader et al. 1995). The near-IR continuum is dominated by young supergiants formed in the merger-induced starburst. Previous CO line ratio studies indicated sub-thermal CO excitation and moderate densities (Radford et al. 1991). Our detection of HCN in Arp 193 indicated, however, that large amounts of dense gas were also present (Solomon, Downes, & Radford 1992).

The CO(2–1) emission is nearly unresolved in individual  $20 \text{ km s}^{-1}$  channels, with temperatures up to 8 K (Fig. 9). The CO intensity and isovelocity contour maps (Fig. 10) reveal a rotating disk with a line of nodes at the same orientation as the optical isophotes in the center of the merger. The position-velocity diagrams and CO spectra (Figs. 11 and 12) along the line of nodes have the characteristic signature of a rotating ring, with two peaks near the rotation curve turnover radius, as in VII Zw 31 and IRAS 10565+24. Models that best fit the data are those with a minimum ring radius  $R_{\text{min}}$  in eq.(1) equal to  $R_0 = 220$  pc. As in VII Zw 31, filled-disk models, with  $R_{\text{min}} = 0$ , give poorer fits, with much less contrast. The centroid of the CO source coincides with the main radio continuum peak on the 8.4 GHz map by Condon et al. (1991). The strongest CO peak is  $1''$  to the southeast of the centroid, and peaks at  $-120 \text{ km s}^{-1}$  (relative to 225.282 GHz). It is nearly unresolved on our maps, coincides with a secondary radio continuum peak. This hot, compact, southeast CO core in Arp 193 is responsible for the large difference in the CO(2–1)/(1–0) ratio in the blue and redshifted sides of the line profiles we observed at the 30 m telescope (Radford et



al. 1991) . This region is hotter and denser than the disk and has properties similar to a huge molecular cloud core.

This compact southeast core is one of several sources we identify in this study as *Extreme Starburst Regions* (see Section 8 on Arp 220 for a detailed discussion). Using the observed CO luminosity, linewidth, radius, and temperature, we can estimate the gas mass, dynamical mass and far IR luminosity of the core. The results, summarized in Table 12, indicate an object with a gas mass  $\sim 6 \times 10^8 M_\odot$ , a luminosity of  $\sim 2 \times 10^{11} L_\odot$ , and about  $\sim 1 \times 10^9 M_\odot$  of newly formed stars.

## 7. Markarian 273

The galaxy Markarian 273 has at least one Seyfert 2 nucleus with optical linewidths of  $700 \text{ km s}^{-1}$  (e.g., Sargent 1972; Koski 1978). There is evidence for two Seyfert 2 nuclei (Asatrian, Petrosian, & Börngen 1990), and two nuclei are seen on IR images (Armus et al. 1992; Majewski et al. 1993; Knapen et al. 1997). Centimeter radio maps show a  $0''.3$  northwest peak coinciding with the CO, and a weaker  $0''.2$  southeast peak with no CO or IR counterpart (Ulvestad & Wilson 1984; Schmelz, Baan, & Haschick 1988; Sopp & Alexander 1991; Condon et al. 1991). There is also an 18 cm VLBI source of 16 mJy (Lonsdale et al. 1993; Smith, Lonsdale, & Lonsdale 1998a). The best previous CO study is by Yun & Scoville (1995), who observed the source with a  $2''$  beam and found a component extended north-south as well as an unresolved nuclear component. Our higher-resolution CO maps also show the extended structure, but now resolve the nuclear source into a nuclear disk oriented east-west, and a very compact core embedded in the nuclear disk.

### 7.1. Extended molecular gas and nuclear disk in Mrk 273

The extended gas is best traced in the CO(1–0) channel maps, blueshifted to the south and redshifted to the north (Fig. 13a). The CO at  $+250$  to  $+350 \text{ km s}^{-1}$  runs in an arc from  $3''$  to  $7''$  (2 to 5 kpc) north of the nucleus (Fig. 14). This extended gas also appears in the maps of CO(1–0) integrated intensity and isovelocity contours (Fig. 15a). The CO(1–0) lines are weaker and narrower in the northern arc than in the nuclear disk (Fig. 16). The arc has 4% of the CO(1–0) flux of Mrk 273, so if gas mass is proportional to CO flux, then the northern arc has a gas mass of  $1 \times 10^8 M_\odot$ . Figure 17a is the CO position-velocity cut in declination, through the nucleus. The narrow-line emission extends  $7''$  (5 kpc) south at  $0 \text{ km s}^{-1}$  and  $7''$  north at  $+300 \text{ km s}^{-1}$ . It is tempting to speculate that the streamers are

bringing molecular gas into the center. The north-south extent of the streamers on our CO map agrees with that on the map by Yun & Scoville (1995). While those authors deduced a line of nodes at p.a.  $30^\circ$ , our isovelocity contour maps show there are two perpendicular kinematic systems. In the extended gas the velocity gradient is north-south, and in the nuclear disk it is east-west.

The  $2''$  nuclear disk with its compact core are best seen in the CO(2–1) channel maps, made with a  $0''.6$  beam (Fig. 13b). The nuclear disk kinematics are shown in the CO(2–1) map (Fig. 15b), where the isovelocity contours trace the east-west velocity gradient of the nuclear disk over a 1 kpc diameter. Figure 17b is the CO position-velocity diagram of the nuclear disk in right ascension. The broad nuclear disk line has a full width to half maximum of  $380 \text{ km s}^{-1}$ , and its velocity centroid changes from  $-300$  to  $+200 \text{ km s}^{-1}$  over  $0''.5$  from west to east. This is a projected velocity gradient of  $1.5 \text{ km s}^{-1} \text{ pc}^{-1}$ , the same as deduced by Schmelz, Baan, & Haschick (1988) from H I absorption. Table 11 lists the stellar and gas masses that would be needed in a starburst in the Mrk 273 molecular disk if the  $L_{\text{FIR}}/M_{\text{new}\star}$  ratio is the same as we adopted in our starburst model of Mrk 231.

## 7.2. An Extreme Starburst Region in Mrk 273

The high-resolution CO(2–1) maps show a remarkable molecular-line source in the Mrk 273 nuclear disk — a bright,  $0.35'' \times < 0.2''$  CO core (Fig. 15b), that resembles the west nucleus of Arp 220. This is the most luminous extreme starburst region in our sample of 10 galaxies. It has an IR luminosity of about  $6 \times 10^{11} L_\odot$ , generated in a region with a radius of only 120 pc and a current molecular mass of  $1 \times 10^9 M_\odot$  (Table 12). To put this in perspective, the entire molecular core has a radius about 5 times that of an IR luminous Milky Way GMC (for example, W51) but with about 3,000 times the molecular mass and  $\approx 10^5$  times the IR luminosity from OB stars.

This core has a broad CO line with a zero-intensity width of  $1060 \text{ km s}^{-1}$ , the same as the OH megamaser (Staveley-Smith et al. 1987). It coincides with the northwest extended continuum peak at 8.44 GHz, which has a size  $0''.32 \times 0''.18$  (Condon et al. 1991), the same as the compact CO. The radio spectrum is nonthermal, with a spectral index of  $-0.6$ . The thermal dust emission dominates the spectrum above 350 GHz (Chini et al. 1989; Rigopoulou et al. 1996). At the CO core, we detect continuum fluxes of  $11 \pm 2 \text{ mJy}$  at 111 GHz and  $8 \pm 2 \text{ mJy}$  at 225 GHz. Extrapolation of the synchrotron and thermal dust spectra indicates the dust contributes 50% of the flux at 1.3 mm and  $< 10\%$  at 3 mm. The extended nonthermal continuum emission coincident with a high mass of dust and gas leaves little doubt that this region is powered by star formation.

## 8. Arp 220

The center of the ultraluminous galaxy Arp 220 has two radio continuum and two IR sources  $1''.0$  apart that are interpreted as merger nuclei. These are not exactly the same objects in the radio and the IR, because both of the east and west IR nuclei are four times larger ( $0''.8$ ) than the radio sources ( $0''.2$ ) (Condon et al. 1991; Graham et al. 1990; Majewski et al. 1993; Miles et al. 1996; Scoville et al. 1998). The  $K$ -band continuum is starlight associated with the nuclei, and is best seen on the HST NICMOS images (Scoville et al. 1998). These images resolve the eastern IR nucleus into a strong NE and weaker SE component, the latter of which coincides with the eastern radio continuum component and the eastern OH masers (Diamond et al. 1989). The two radio sources are extended and nonthermal, and are produced by supernovae in the most active star-forming regions. The  $1.3$  and  $1.6\ \mu\text{m}$  [Fe II] lines in the west source indicate iron evaporated from dust in shocks (Armus et al. 1995a; van der Werf & Israel 1998). The best previous CO study is that by Scoville, Yun, & Bryant (1997), who derived the kinematics of the nuclear disk with a resolution of  $1''$ .

### 8.1. CO and dust emission from the two nuclei of Arp 220

Our CO(2–1) and 1.3mm continuum maps (Fig. 18a) show two compact sources embedded in more extended emission. The continuum fluxes at 1.3mm are due to dust, because they are well above the extrapolated radio synchrotron spectra (Fig. 20). The different appearance of the dust continuum and the CO maps is a temperature effect. At 1.3mm the dust is optically thin and its flux varies as the column density and the dust temperature, while the CO flux is partly opaque, with flux varying with temperature at the surface, and partly optically thin, with flux varying inversely with CO excitation temperature. The Arp 220 molecular disk contributes strongly to the CO maps, while the warmer compact peaks dominate the dust continuum maps. From the 1.3mm dust flux alone, and for dust at 100 K and solar metallicity, we derive gas masses for Arp 220-west and -east of  $0.6$  and  $1.1 \times 10^9 M_{\odot}$ .

In *Arp 220-west*, the  $0''.3$  (100 pc) mm continuum dust source coincides within  $0''.1$  of the cm-continuum west peak, and the  $K$ -band west peak (Scoville et al. 1998). In the CO(2–1) channel maps (Fig. 19b), Arp 220-west appears as a strong source in the range  $-310$  to  $+210\ \text{km s}^{-1}$ , peaking at  $-110\ \text{km s}^{-1}$  ( $cz_{\text{l sr}} = 5340\ \text{km s}^{-1}$ ), with an *observed* CO(2–1) brightness temperature of 27 K, of which 10 K is from the more extended Arp 220 disk. The positive-velocity emission near Arp 220-west is centered at  $+80\ \text{km s}^{-1}$ , and appears in both the CO(2–1) channel maps and in a position-velocity cut at p.a.  $300^{\circ}$

(Fig. 22b). This positive-velocity emission has about 25% of the CO integrated intensity of the negative-velocity emission of Arp 220-west.

The dust continuum is centered between the negative and positive velocity emission, suggesting that Arp 220-west is a composite structure, with a kinematic axis nearly perpendicular to that of Arp 220’s main disk. At the negative velocity west core, the emission extends asymmetrically from  $-50$  to  $-400$   $\text{km s}^{-1}$  (Fig. 22b). At the positive velocity core, it runs from  $+50$  to  $+350$   $\text{km s}^{-1}$ . These extreme, asymmetric line profiles, confined to a small region, suggest possible radial flows along a *bar-like* structure, or immense high-velocity molecular *outflows* similar to those observed in high mass star formation regions. Molecular outflows are also the likely sites of the strong H<sub>2</sub> lines (Sturm et al. 1996) .

In *Arp 220-east*, the CO covers a wide velocity range. The negative-velocity gas at  $-230$  to  $-30$   $\text{km s}^{-1}$  is separated from Arp 220-west by  $0.''85$  at p.a.  $110^\circ$  — the same angle as the cm-radio continuum sources, the 18 cm OH masers, and the *K*-band SE peak (Scoville et al. 1998). The center velocity of this gas is  $cz_{\text{lsr}} = 5330$   $\text{km s}^{-1}$ , close to that of the OH megamasers and H<sub>2</sub>CO emission at the cm-radio east source (Baan & Haschick 1995; Lonsdale et al. 1998). There is also more extended, positive-velocity gas ( $0.''9$  FWHM) at  $130$  to  $290$   $\text{km s}^{-1}$ . It is  $1.''3$  from Arp 220-west at p.a.  $85^\circ$  — the same orientation as the *K*-band NE source (Scoville et al. 1998). This positive-velocity gas in Arp 220-east, at  $\sim +200$   $\text{km s}^{-1}$  ( $cz_{\text{lsr}} = 5650$   $\text{km s}^{-1}$ ), has the same velocity offset from Arp 220-west as the ionized gas seen in Br $\gamma$  and Pa $\beta$  (Larkin et al. 1995), and the weak OH masers at 1612 MHz (Baan & Haschick 1987). Its *observed* maximum CO(2–1) brightness temperature is 19 K, of which 4 K is from the extended Arp 220 disk. The 1.3 mm continuum from dust in Arp 220-east has a diameter of  $0.''6$  (205 pc) and is displaced by  $0.''3$  from the cm-radio east source. It falls in between the *K*-band NE and SE peaks on the images by Scoville et al. (1998), and in between the positive and negative-velocity CO. The kinematic data suggest that Arp 220-east has a steady progression of velocity between the CO peaks at  $5330$   $\text{km s}^{-1}$  and  $5650$   $\text{km s}^{-1}$ , along the same position angle (p.a.  $50^\circ$ ), and in the same sense of rotation as the main, larger-scale molecular disk of Arp 220 (Fig. 22c).

## 8.2. CO in the Arp 220 molecular disk

The molecular disk is best seen as an extended source in the CO(1–0) maps (Fig. 18b). The CO(2–1) maps also show this same extended source, when the compact peaks are subtracted. The disk has CO halfwidths of  $2.''0 \times 1.''6$  at p.a.  $50^\circ$ , with a line of nodes at this same position angle, blueshifted in the southwest and redshifted in the northeast,

as seen in the CO spectra along the major axis (Fig. 21). Our model fits yield a rotation curve turnover radius of 200 pc, a disk outer radius of 480 pc, and a disk rotation velocity of  $330 \text{ km s}^{-1}$  on the flat part of the rotation curve. The CO emission centroid of the molecular disk is  $\sim 0''.3$  east of the western nucleus. These parameters reproduce the position-velocity diagrams along the kinematic major axis (Fig. 22), and are similar to the values derived by Scoville et al. (1997) by a different algorithm. On a larger scale, CO can be traced in the  $8''$  diameter *outer disk* at the same position angle. The inner and outer disks both contain shocked gas, detected in the near-IR vibrational lines of  $\text{H}_2$  (van der Werf 1996).

The CO(1–0) maps also show an eastern streamer extending  $7''$  (3 kpc) perpendicular to the disk, in the range  $+45$  to  $+245 \text{ km s}^{-1}$ , curving in to the east nucleus with increasing velocity offset (Fig. 19a). This east streamer is most intense at  $85$  to  $165 \text{ km s}^{-1}$  (Fig. 18b). It may be material that is still falling into the center. Surprisingly, this CO streamer appears on the HST *V*-band image by Shaya et al. (1994). The CO inner and outer disks coincide with the prominent optical dust lane at  $50^\circ$  (Fig. 23a), while the CO east streamer coincides with the perpendicular dust lane in the optical image (Fig. 23b).

Our model fits to the CO position-velocity diagrams of the Arp 220 disk (Fig. 22) yield a much higher dynamical mass than estimates from the IR (e.g., Doyon et al. 1994; Shier, Rieke, & Rieke 1994, 1996; Larkin et al. 1995). From the masses in Table 9, we estimate  $M(< 350 \text{ pc}) = 8.8 \times 10^9 M_\odot$ , and  $M(< 600 \text{ pc}) = 1.5 \times 10^{10} M_\odot$ , three to four times higher than the IR estimates. The millimeter CO data and the  $2.3 \mu\text{m}$  CO bandhead absorption data yield different masses because the two IR nuclei do not lie on the line of nodes traced by the CO maps and because the near IR starlight is obscured and does not trace the full extent of the molecular disk.

The gas mass derived from both the dust and the CO implies a column density of  $1 \times 10^{24} \text{ cm}^{-2}$  and  $A_V \sim 1000 \text{ mag}$  through the disk, consistent with the dust having an opacity of unity at  $180 \mu\text{m}$  (Emerson et al. 1984; Scoville et al. 1991). The high opacity in the far IR may partly explain why the  $\text{C}^+$   $158 \mu\text{m}$  line is weak in Arp 220 (Fischer et al. 1998.). The ratios of fine structure lines observed by the *ISO* satellite yield an equivalent screen  $A_V \sim 45 \text{ mag}$  (Genzel et al. 1998). As is well known, a screen model gives only an extreme lower limit. The corresponding extinction when the emitting gas and dust are completely mixed is  $A_V \sim 1000 \text{ mag}$ , the same as we deduce from the column density derived from the CO maps.

Figure 24 shows our model of the molecular disk and the two “nuclei”. The CO disk is inclined  $40^\circ$  from face-on, Arp 220-west has a radius of 68 pc, and Arp 220-east has a radius of 110 pc. The disk thickness is 90 pc, which means the path to the near surface of the east and west K-band sources is 0 to 20 pc, which is why the two nuclei are visible at

all at  $K$  band. That is, although the visible extinction through the entire molecular disk is 1000 mag, the visible extinction to the near surfaces of the east and west sources is only about 50 mag, because of the shorter path. Our diagram is similar to that of Scoville et al. (1997; their Fig. 7), except our presentation is a view from the pole of the disk. In our model, the near side is north, the far side is south. This agrees with the optical colors, which are bluer on the north side of the dust lane (Shaya et al. 1994). Since the CO east nucleus is south of the major axis, it is on the far side. The CO disk or ring includes both nuclei but the nuclei are oriented east-west, and hence the difference in their line of sight velocities does not give the full rotation speed of the disk.

Our data and model have some important consequences for the interpretation of the Arp 220 nuclear sources.

1) The rotation curve of the CO disk indicates a dynamical mass of  $12 \times 10^9 M_\odot$  interior to 480 pc, which corresponds to the central bulge mass of a large spiral like the Milky Way.

2) The gas mass in each of the two extreme starburst “nuclei” is only  $6 \times 10^8 M_\odot$ . Their individual luminosities are  $\sim 3 \times 10^{11} L_\odot$ . (About half of the Arp 220 FIR luminosity comes from the molecular disk, not the two nuclei). With an L/M ratio of 1000, corresponding to a super-starburst in its initial phase, the mass of new stars in each nucleus would be only  $3 \times 10^8 M_\odot$ , sufficient to explain all the  $K$ -band continuum luminosity. The velocity dispersion of the CO in each of the two nuclei implies a dynamical mass of  $\sim 1 \times 10^9 M_\odot$ , about the same as our estimate of the sum of the gas and new stars.

3) Hence, there is no room left over for old stars in the two “nuclei” — they cannot be the relicts of the old nuclei of the pre-merger galaxies. Furthermore, there is no observational evidence — radio, infrared, or optical — that they contain old stars.

4) In any case, the masses of the two “nuclei” are negligible in comparison with the mass that controls the motion of the molecular disk. Furthermore, the two “nuclei” of Arp 220 have radial velocities indicating that they take part in the general disk rotation, i.e., they share the general rotation in the potential of the old bulge, and are dominated by *its* gravity, not their own.

5) In our interpretation, the two “nuclei” of Arp 220 are not the pre-merger nuclei at all. We think they are just large ensembles of pre-existing GMCs that have been strongly compressed on their infall into the old bulge potential as a result of the merger. The masses of these large, compressed gas structures can reach  $10^9 M_\odot$ , and the strong compression, in about one orbital period, leads to the extreme starbursts, with luminosities of a few times  $10^{11} L_\odot$ , from each compact 100-pc structure. These extreme starbursts power the ultraluminous galaxies. We are not seeing the birth of quasars.

### 8.3. Arguments for a starburst

What produces Arp 220’s luminosity? We think it’s stars, for three reasons: there is no obvious AGN, there are enough ionizing photons for a starburst, and there is enough dense molecular gas to make stars.

1. *Arp 220 has no AGN lines.* The mid-IR lines of [O IV] and [Ne V] are *not* detected (Sturm et al. 1996; Lutz et al. 1996). The Br $\alpha$  width of  $1300 \text{ km s}^{-1}$  reported by Depoy, Becklin, & Geballe (1987) as evidence for an AGN was not confirmed in later measurements (Goldader et al. 1995; Larkin et al. 1995).
2. *Arp 220 has no AGN in the radio continuum.* New VLBA maps (Smith et al. 1998b) indicate all the VLBI point sources are young radio supernovae in a dense medium, with radio luminosities comparable to SN1986J in NGC 891.
3. *The radio nuclei are extended starburst regions.* At centimeter wavelengths, their diameters are: west,  $0''.21 \times 0''.14$  ( $72 \times 48 \text{ pc}$ ) and east,  $0''.32 \times 0''.19$  ( $110 \times 64 \text{ pc}$ ) (Condon et al. 1991). The source extent, the low brightness at 5 GHz, and the high FIR-to-radio flux ratio all show the nonthermal radio continuum is starburst-dominated, not AGN-dominated (Sopp & Alexander 1991; Condon et al. 1991; Baan & Haschick 1995).
4. *Arp 220 is not a “warm” ultraluminous galaxy.* IR ultraluminous galaxies with an AGN, like Mrk 231, Mrk 1014, and 08572+3915, have warm mid-IR colors ( $f_{25}/f_{60} > 0.2$ ) and a bright, symmetric nucleus resembling a reddened QSO (Surace et al. 1998). Unlike these sources, Arp 220 has strong far-IR and weaker mid-IR flux ( $f_{25}/f_{60} = 0.08$ ). It has been argued that a QSO is hidden in Arp 220, but the silicate absorption depth at  $10 \mu\text{m}$  in Arp 220 (e.g., Smith, Aitken, & Roche 1989; Dudley & Wynn-Williams 1997) has been greatly overestimated, due to the strong PAH lines directly adjacent to the silicate feature (Genzel et al. 1998), so a deeply embedded AGN is not required.
5. *The diffuse OH megamasers do not indicate black holes.* A new VLBI study (Lonsdale et al. 1998) shows Arp 220 has two OH megamaser components in each nucleus, one diffuse and the other compact. The *diffuse* megamaser component arises in the extended starburst medium, and can be explained by IR pumping via photons absorbed in the  $35$  and  $53 \mu\text{m}$  lines of OH. The observed 9-Jy depth of the  $35 \mu\text{m}$  OH line can only be explained by absorption against an *extended* source (Skinner et al. 1997). The *compact* OH megamasers, probably collisionally pumped shocks, are currently the only evidence for possible AGNs in Arp 220 (Lonsdale et al. 1998), but it is hard to understand why such AGNs would have no associated radio continuum core-jet sources.

#### 8.4. The ratio of bolometric flux to ionizing flux resembles that in Sgr B2.

From the observed  $\text{Br}\gamma$  flux, Armus et al. (1995b) and Shier, Rieke, & Rieke (1996) estimated that  $\leq 10\%$  of Arp 220’s luminosity came from a starburst. Armus et al. noted, however, if they had underestimated the  $K$  band extinction, then a starburst could power the source. The higher near-IR extinction is indeed required by the high column densities found from the CO maps. From the radio free-free continuum, Scoville et al. (1991; 1997) claimed there were not enough ionizing photons for a starburst to power Arp 220. We think this expectation was wrong, because galactic star-forming regions like W49, W51, and Sgr B2 have FIR luminosities greatly exceeding the Lyman luminosities derived from their radio fluxes. In compact HII regions like W3(OH), or in our galactic center, the FIR excess is a factor of  $\sim 20$  (e.g., Zylka et al. 1995).

In H II regions with densities  $> 10^3 \text{ cm}^{-3}$ , most of the Lyman photons heat dust rather than ionizing the gas (Jennings 1975; Panagia 1977; Fazio 1978; Mezger 1985), so the Lyman photon rate derived from the radio flux is only a lower limit. We may estimate this lower limit to Arp 220’s Lyman continuum photon flux from the continuum at 113 GHz, which includes 15 mJy from the synchrotron spectra and 13 mJy from dust (Fig. 20). This leaves 13 mJy as optically thin free-free flux, and implies a Lyman continuum photon rate  $> 1 \times 10^{55} \text{ s}^{-1}$ . Similar lower limits come from the  $\text{H}92\alpha$  radio recombination line (Zhao et al. 1996), and the low-frequency turnover of the radio spectra of the two nuclei (Fig. 20), due to free-free absorption in ionized gas with an emission measure of  $10^8 \text{ cm}^{-6} \text{ pc}$  and a mass of  $5 \times 10^7 M_{\odot}$  (Sopp & Alexander 1991).

For comparison, in the galactic giant H II region and molecular cloud Sgr B2, the FIR power is 10 times the ionizing luminosity derived from the radio (Gatley et al. 1978). Sgr B2 resembles Arp 220’s molecular gas in column density, strong molecular lines, and far-IR opacity, but no one has ever claimed Sgr B2’s FIR excess proves it is powered by a black hole. Arp 220 and Sgr B2 both have the same ratio of FIR flux (in  $\text{W m}^{-2}$ ) to radio free-free flux (in Jy), and hence the same FIR excess. So our lower limit on Arp 220’s ionizing flux, scaled by the Sgr B2 template, yields exactly Arp 220’s FIR luminosity of  $1.2 \times 10^{12} L_{\odot}$ , and is indeed compatible with a starburst. Similar conclusions are reached by Genzel et al. (1998) from *ISO* line data on the ionizing flux.

#### 8.5. Arp 220 has plenty of gas for a starburst.

Our models yield gas masses of  $0.6 \times 10^9 M_{\odot}$  for Arp 220-west,  $1 \times 10^9 M_{\odot}$  for Arp 220-east, and  $3 \times 10^9 M_{\odot}$  for the disk to  $R_2 = 1.2 \text{ kpc}$  (Table 9). The total gas mass



is  $5 \times 10^9 M_\odot$ , about 6 times lower than previous estimates with a standard ratio of gas mass to CO luminosity. Our value agrees with the gas mass of  $3.5 \times 10^9 M_\odot$  obtained by Sturm et al. (1996) from the  $H_2$  lines at 6.9 and  $17 \mu\text{m}$ , although this latter value depends sensitively on the assumed temperature. Our method differs from that of Scoville, Yun, & Bryant (1997), who assumed all the dynamical mass is in gas, rather than stars, thereby forcing their model CO disk to be only 16 pc thick at  $R = 250$  pc, and to have a *mean* density of  $1.5 \times 10^4 \text{cm}^{-3}$ . Because we do not assume all the mass is gas, we derive a disk thickness of 80 pc and a lower mean density than Scoville et al. Our higher-resolution data indicate the gas density is highest at the two nuclei, not at the center of the molecular disk as in the model of Scoville et al., and our value for the total gas mass is therefore a factor of two lower than their estimate.

Even the lower molecular gas mass, however, is about the same as in the entire disk of a gas-rich spiral! It is enough gas for a huge nuclear starburst. In the Arp 220 inner disk, the gas surface density is 100 times the peak value in the Milky Way 4-kpc molecular ring and more than 20 times the surface density in the inner few hundred pc of our Galaxy. To estimate the *stellar* mass in the nuclear bulge, we adopted a global luminosity to starburst mass ratio in the Arp 220 disk of  $300 L_\odot M_\odot^{-1}$ , based on starburst  $L/M$  ratios from the models of Leitherer & Heckman (1995). This gives a estimate of the mass in newly-formed stars from the current merger-induced starbursts. Subtracting this mass and the gas mass from the dynamical mass then gives an rough estimate of the mass in old, pre-merger stars. The resulting bulge mass is  $8 \times 10^9 M_\odot$  within  $R = 480$  pc (Table 11), about the same as in a large galaxy like our own (e.g., Oort 1977). The starburst interpretation thus implies that old stars are a significant part of the dynamical mass.

### 8.6. Arp 220-west has 25% of the total luminosity.

The CO lines, the 1.3 mm dust flux, and the cm-radio continuum all suggest the currently most active starburst is Arp 220-west. Its radius of 68 pc and dust temperature of 75 to 80 K imply a blackbody luminosity of  $3 \times 10^{11} L_\odot$ , or about 25% of Arp 220's total IR luminosity of  $1.3 \times 10^{12} L_\odot$ , as expected from the  $R^2 T_d^4$  ratio of the west and disk sources. This estimate also agrees with the fraction of the mid-IR flux absorbed by the  $35 \mu\text{m}$  OH line at  $5320 \text{km s}^{-1}$  (Skinner et al. 1997), the velocity of Arp 220 west. If the Lyman continuum scales as FIR luminosity, then Arp 220-west has 1000 times the ionizing flux of 30 Doradus, which is  $10^{52}$  photons  $\text{s}^{-1}$  (Kennicutt & Chu 1994), from 2400 OB stars in a region of comparable size (Parker 1993). Because Arp 220-west is small and the dynamical time scale is short, its starburst must be younger (age  $5 \times 10^6$  yr) than that in

the larger Arp 220 disk. The initial phase of a compact starburst can be highly luminous, reaching  $L/M$  ratios of  $1000 - 3000 L_{\odot} M_{\odot}^{-1}$  (see models in Leitherer & Heckman 1995). Our estimate of the total mass (from the CO linewidth) and the gas mass (from the CO luminosity), suggests that in Arp 220-west, 50 to 60% of the original gas mass has already turned into the new stars in the current, extreme starburst (Table 12).

## 9. SOURCES OBSERVED IN CO(1–0) ONLY

We observed these sources with lower resolution and thus our kinematic models are less precise. All these sources show the same phenomena as the previous group of sources, however, with velocity gradients and line profiles that suggest rotating rings or disks.

### 9.1. 00057+4021

The galaxy IRAS 00057+4021 has not been well studied, despite its high luminosity of  $L_{\text{IR}} = 4 \times 10^{11} L_{\odot}$ , and its OH megamaser (Kazès, Mirabel, & Combes 1988). The  $R$ -band image by Armus, Heckman, & Miley (1987) shows a  $60''$  (48 kpc) southeast-northwest disk with a tidal tail stretching a further  $45''$  (36 kpc) southeast. In contrast to the optical light, the CO source is quite compact. Most of the molecular gas is in a  $1''.1 \times < 0''.6$  core source. The CO has wider lines ( $140 \text{ km s}^{-1}$  FWHM) and is more intense on the southeast side of the line of nodes than on the northwest (Fig. 25). The continuum flux from the CO source is  $< 10 \text{ mJy}$  at 110 GHz. This limit on the thermal dust flux is consistent with the gas mass of  $9 \times 10^8 M_{\odot}$  deduced from our model fits to the CO.

In the position-velocity diagram along the line of nodes at p.a.  $135^{\circ}$  the CO line has a velocity range of  $300 \text{ km s}^{-1}$  over a diameter of  $3''$  (Fig. 25). The CO lines are blue-shifted in the northwest and redshifted in the southeast. In strips parallel to the kinematic major axis the CO spectra show the double-peak behavior of a rotating disk or ring. To the southeast, the CO profile is steep toward the red, and gently sloping toward the blue. To the northwest, the profile is reversed. The nuclear velocity gradient in CO has the same major axis as the larger-scale optical isophotes. The position-velocity data and the spectra both indicate another, lower-intensity (0.5 K) disk with a broad linewidth ( $200 \text{ km s}^{-1}$ ) in the same region as the brighter, high-density disk.

## 9.2. 02483+4302

The galaxy IRAS 02483+4302 is a merger with a tidal tail extending  $90''$  to the west. The merger has two nuclei separated by  $3''.8$  east-west. In optical lines, nucleus *A* (west) has a Seyfert 2 spectrum, nucleus *B* (east) has a LINER spectrum. The optically more intense nucleus *A* appears to belong to an elliptical galaxy plowing through the disk of a former spiral containing nucleus *B* (Kollatschny et al. 1991). The optical continuum of nucleus *B* comes partly from hot stars (Womble et al. 1990).

The CO (Table 2) coincides with nucleus *B*, supporting the idea that this was originally a gas-rich spiral. Our CO position also agrees within  $0.5''$  of the 13 mJy source seen at 5 GHz (Crawford et al. 1996). At 109 GHz, the continuum flux from the CO source is  $< 10$  mJy. This limit on the thermal dust flux is consistent with the gas mass deduced from the CO. In velocity channels  $40 \text{ km s}^{-1}$  wide, the CO source is very compact. Figure 26 shows the maps of CO integrated intensity and isovelocity contours across the source. The CO has a north-south velocity gradient, with a kinematic major axis perpendicular to the optical tidal tail extending west from the merger nuclei.

In strips parallel to the kinematic major axis the CO spectra show the symmetric behavior of a rotating disk or ring. In the south, the CO profile is steep toward the blue and gently sloping toward the red. In the north, the profile is reversed. The position-velocity diagram along the line of nodes shows a gradient of  $200 \text{ km s}^{-1}$  over  $0''.9$  in declination (Fig. 26). The narrow CO linewidth and the low optical extinction to the nucleus both suggest the molecular disk around nucleus *B* is face-on.

The CO source, at  $z = 0.05144$ , ( $cz_{\text{lsr}} = 15420 \text{ km s}^{-1}$ ) and the quasar Q0248+430 at  $z = 1.311$  are separated on the sky by  $16''.9$  (the galaxy-quasar separation is incorrectly listed as  $3''.5$  by Burbidge (1996) and by Hoyle & Burbidge (1996)). The tidal tail that extends  $> 80$  kpc from the two merger nuclei crosses the quasar at a projected distance of 15.4 kpc from the CO source. At this position, low-density atomic gas in the tidal tail is seen in absorption against the quasar in the Na I D and Ca II H and K lines at  $z = 0.0515$  and 0.0523, with linewidths  $< 150 \text{ km s}^{-1}$  (Womble et al. 1990). There are two other absorption systems, in Mg II, at  $z = 0.394$  and 0.451, from the halos of other, more distant galaxies on the line of sight to the quasar (Womble et al. 1990; Sargent & Steidel 1990; Borgeest et al. 1991). After correcting for the primary beam, we derived the quasar’s continuum flux to be 190 mJy at 110 GHz in June-October 1994. Toward the quasar, our data at  $20 \text{ km s}^{-1}$  resolution do not show any CO(1–0) absorption within  $\pm 600 \text{ km s}^{-1}$  of the center frequency (Table 1), to a limit of 30 mJy, or 15% of the quasar’s millimeter continuum flux. This range includes the  $z = 0.0523$  ( $cz = 15300 \text{ km s}^{-1}$ ) redshift seen in absorption against the quasar in Na I and Ca II. If the absorbing atomic gas extends 0.3 to 3 kpc on the line of

sight, the width of the tidal tail on optical images, then the column densities derived from the Na I and Ca II lines by Womble et al. (1990) imply H I densities of  $1 - 10 \text{ cm}^{-3}$ , too low for any gas to be in molecular form.

### 9.3. 10565+2448

The main optical and near IR peak of IRAS 10565+2448 has strong Br  $\gamma$  lines (Goldader et al. 1995) and H II region-type line ratios (Armus, Heckman, & Miley, 1989, 1990; Veilleux et al. 1995). Murphy et al. (1996) suggest this merger is a triple galaxy system. On their  $r$  band image there is a secondary source on a tidal tail,  $26''$  (20 kpc) northeast of the main peak, at the same redshift. A third object with unknown redshift is  $7.9''$  (6.2 kpc) southeast of the main peak. In our 500 MHz band we detect no CO toward the other two  $r$ -band sources, to a limit of  $20 \text{ mJy beam}^{-1}$  in  $20 \text{ km s}^{-1}$  channels. At centimeter wavelengths, there is extended emission and an unresolved, nonthermal core (Condon et al. 1991; Crawford et al. 1996).

Figure 27 shows the maps of CO integrated intensity, isovelocity contours, and CO linewidth. The peak of the  $2''.3 \times 1''.7$  CO source coincides with the compact cm-radio continuum core. Along the line of nodes, the CO line profiles are very symmetric, with well-defined blueshifted peaks in the east and redshifted peaks in the west (Fig. 28). Together with VII Zw 31 and Arp 193, the galaxy 10565+2448 is one of the best examples of a rotating ring in our sample. In the position-velocity diagram (Fig. 29), there are two prominent peaks, and a velocity shift of  $180 \text{ km s}^{-1}$  over the central  $1''$  in R.A. Models that best fit the data are those with a minimum ring radius  $R_{\text{min}}$  in eq.(1) equal to  $R_0 = 230 \text{ pc}$ . As with VII Zw 31 and Arp 193, filled-disk models, with  $R_{\text{min}} = 0$ , give poorer fits, with much less contrast. The CO ring must be nearly face-on, because of the small separation ( $80 \text{ km s}^{-1}$ ) of the twin peaks, the narrow CO linewidth ( $140 \text{ km s}^{-1}$  FWHP), and the small extent of the integrated CO intensity on the kinematic major axis. Unlike Arp 220 or VII Zw 31, there is not much CO in an outer disk beyond the nuclear ring of 10565+2448.

### 9.4. 17208–0014

The ultraluminous galaxy 17208–0014 has  $L_{\text{IR}} = 2.2 \times 10^{12} L_{\odot}$  and an optical and near-IR line spectrum that indicates H II region-type excitation and high reddening (Martin et al. 1989; Kim et al. 1995; Goldader et al. 1995; Veilleux et al. 1995). Images at  $r$ -band ( $6550 \text{ \AA}$ ) show two tidal tails from a merger (Melnick & Mirabel 1990; Murphy et al. 1996).

The innermost parts of the two tails, extending north and east to radii  $> 20$  kpc are nicely shown in the  $r$ -band image by Sanders & Kim (in Solomon et al. 1997). At  $2''.9$  (2.2 kpc) southeast of the nucleus, the  $r$  band and  $I$  band ( $0.82 \mu\text{m}$ ) images show a secondary peak on a tidal tail. The  $K$ -band ( $2.2 \mu\text{m}$ ) surface brightness has an  $r^{1/4}$  profile out to a radius of 10 kpc, as in elliptical galaxies, probably due to the merger. The nucleus has a size of  $1''.8 \times 1''.4$  in  $K$  band and appears single, which suggests a completed merger (Zenner & Lenzen 1993; Murphy et al. 1996). The nucleus also has one of the strongest known OH megamasers, with  $10^3 L_{\odot}$  in the 1667 MHz OH line, and a radio continuum source of size  $0''.32 \times 0''.26$  ( $220 \times 270$  pc; Martin et al. 1989).

Figure 30 shows the maps of CO(1–0) integrated intensity and isovelocity contours. The CO source has a size of  $1''.8 \times 1''.6$ , smaller than measured by Planesas, Mirabel, & Sanders (1991), and about the same size as the  $K$  band source. The centroid of the CO source (Table 2) agrees to within  $0''.2$  with the cm-radio continuum source (Martin et al. 1989). The isovelocity contours and the CO spectra show the molecular gas is blueshifted in the northwest and redshifted in the southeast. The position-velocity diagram (Fig. 30) indicates a strong velocity gradient with a change of  $400 \text{ km s}^{-1}$  over  $1''.5$  at p.a.  $120^\circ$ . We interpret this angle as the line of nodes of the nuclear disk. The CO spectrum at the peak of the source (Fig. 30) has a linewidth of  $375 \text{ km s}^{-1}$  FWHM, and  $700 \text{ km s}^{-1}$  to zero intensity. At the CO peak, there appears to be a weak continuum at the 5 mJy level.

## 9.5. 23365+3604

On  $R$ -band images, the ultraluminous galaxy 23365+3604 has two tidal tails, but only a single, blue nucleus (Klaas & Elsässer 1991; Murphy et al. 1996). The optical spectrum (e.g., Veilleux et al. 1995) is of the LINER type, with line ratios implying shock velocities of  $80 - 90 \text{ km s}^{-1}$  and pre-shock electron densities of  $1 - 10 \text{ cm}^{-3}$  in tenuous gas, as in old supernova remnants (Klaas & Elsässer 1991). In the nucleus, The [O III] line has a width of  $260 \text{ km s}^{-1}$  FWHM (Kim et al. 1995). The source has strong  $\text{Br}\gamma$  and  $\text{H}_2$  lines at  $2 \mu\text{m}$  (Goldader et al. 1995). In the 6 cm radio continuum, there is a secondary source extending  $1''$  south of the nucleus (Crawford et al. 1996).

In our  $40 \text{ km s}^{-1}$  channel maps, the CO source is compact in all channels over a range of  $320 \text{ km s}^{-1}$ . The CO source has a size of  $1''.0 \times 0''.9$ , with a peak  $2''$  south of the optical position listed by Klaas & Elsässer (1993). The gradient in the isovelocity contours is at p.a.  $135^\circ$ , and the CO spectra along this line of nodes show asymmetric profiles characteristic of a rotating ring or disk. Along this kinematic major axis, the position-velocity diagram shows a shift of  $300 \text{ km s}^{-1}$  over  $4''$  (Fig. 31).

## 10. DISCUSSION

### 10.1. Source sizes, gas masses from CO imaging, and the ratios $M_{\text{gas}}/L'_{\text{CO}}$ and $M_{\text{gas}}/M_{\text{dyn}}$

The main results of this study are the CO source sizes — the halfwidths of the integrated CO emission (Table 3), and the inner and outer disk radii from the model fits to the position-velocity diagrams and the channel maps (Table 4). The measured radii of the integrated CO correspond to the half-power radii  $R_1$  derived from the kinematic data. We had previously noted that for ultraluminous galaxies the CO(1–0) flux ( $\text{Jy km s}^{-1}$ ) was  $\sim 4$  times the  $100 \mu\text{m}$  flux (Jy), as expected from a blackbody model for the far IR (Downes, Solomon, & Radford 1993). We derived the dust temperature from the FIR fluxes, and took this to be the intrinsic CO brightness temperature. From the CO luminosity, we then predicted the mean radius,  $R_{\text{CO}}$ , for a spherical CO source (Solomon et al. 1997). Interestingly, the sizes measured with the interferometer are within a factor of two of the blackbody sizes. The radii  $R_0$  and  $R_1$  from our fits to the kinematic data (Table 4) bracket our single-dish estimate:  $R_0 < R_{\text{CO}} < R_1$ . The CO radii measured with the interferometer now allow us to better estimate the gas and dynamical masses (Table 9).

In the centers of ultraluminous galaxies, we find  $M_{\text{gas}}/L'_{\text{CO}} \approx 0.8 M_{\odot} (\text{K km s}^{-1} \text{ pc}^2)^{-1}$ , about 5 times lower than the standard value for self-gravitating molecular clouds. We had anticipated this result from single-dish data (Downes et al. 1993; Solomon et al. 1997), and it is now confirmed by the interferometer maps. We had earlier used the CO linewidths and radii from our blackbody model to obtain dynamical mass, which in turn led us to revise downward the gas masses from single-dish CO luminosities. We estimated a minimum gas mass by assuming optically thin CO. These estimates, which we labeled  $M_{\text{thin}}$  (Solomon et al. 1997), are within a factor 1.5 of the gas masses derived from our model fits to the interferometer data. Table 9 also lists the ratio of gas mass to dynamical mass, which is  $\sim 1/6$  in the inner, high-density disk, and  $1/10$  in the outer, low-density disks.

We showed earlier (Downes et al. 1993) that the  $M_{\text{gas}}/M_{\text{dyn}}$  and  $M_{\text{gas}}/L'_{\text{CO}}$  ratios are related by

$$\left(\frac{M_{\text{gas}}}{M_{\text{dyn}}}\right) = \left(\frac{M_{\text{gas}}}{L'_{\text{CO}}}\right)^2 \frac{1}{\alpha^2} \quad , \quad (10)$$

where, letting  $f \equiv M_{\text{gas}}/M_{\text{dyn}}$ , we have

$$M_{\text{gas}} = f^{0.5} \alpha L'_{\text{CO}} \quad . \quad (11)$$

The factor  $\alpha = Cn^{0.5}/T_b$ , where  $n$  is the mean  $\text{H}_2$  number density over the whole volume and  $T_b$  is the CO brightness temperature. In the units used here, the constant  $C = 2.6$  for a

sphere and  $\sim 1.0$  for a flared disk with thickness/radius ratio of 0.15, as in some of the disks in our sample. These equations depend only on gravity, and are independent of whether the gas is self-gravitating or not, or whether the CO lines are optically thick or thin.

The derived values for  $M_{\text{gas}}/M_{\text{dyn}}$  and  $M_{\text{gas}}/L'_{\text{CO}}$  are compatible with starbursts. Assume a starburst powers an ultraluminous IR galaxy, with  $L/M_{\text{new}\star} = 300 L_{\odot} M_{\odot}^{-1}$  for the new stars in the burst, all the power emerging in the IR. Such galaxies typically have  $L_{\text{IR}}/L'_{\text{CO}} = 200 L_{\odot} (\text{K km s}^{-1} \text{ pc}^2)^{-1}$ . Combining the two luminosity ratios gives

$$M_{\text{new}\star} = (2/3)L'_{\text{CO}} \quad , \quad (12)$$

or  $\sim 3 \times 10^9 M_{\odot}$  as the mass of new stars in the burst. Most galaxies prior to the merger would have had a rotation velocity  $\sim 250 \text{ km s}^{-1}$  at a radius of 500 pc, which implies an old stellar bulge about twice as massive as the newly-formed population. Since  $M_{\text{dyn}} = M_{\text{gas}} + M_{\text{new}\star} + M_{\text{old}\star}$ , we have from the previous equation that

$$M_{\text{dyn}} = M_{\text{gas}} + 2L'_{\text{CO}}. \quad (13)$$

Solving for the molecular gas mass yields

$$\frac{M_{\text{gas}}}{L'_{\text{CO}}} = (1 + \alpha^2)^{1/2} - 1 \quad . \quad (14)$$

This equation can be generalized to arbitrary mass ratios of the old and new stellar populations. For the Arp 220 disk, with a *mean*  $\text{H}_2$  density  $\sim 500 \text{ cm}^{-3}$  and  $\langle T_b \rangle = 20 \text{ K}$ , these equations predict  $\alpha \sim 1$ ,  $M_{\text{gas}}/M_{\text{dyn}} = 0.2$ , and  $M_{\text{gas}}/L'_{\text{CO}} = 0.4 M_{\odot} (\text{K km s}^{-1} \text{ pc}^2)^{-1}$ , close to the values derived from our model fits to the interferometer data. In other words, the starburst scenario is compatible with the derived ratios.

## 10.2. Dense gas traced by HCN and extreme starburst regions

There is another important gas component that is better traced by emission from high dipole moment molecules like HCN, rather than CO. The HCN emission requires densities  $n(\text{H}_2) > 10^4 \text{ cm}^{-3}$ . In giant molecular clouds in the disks of the Milky Way and normal spirals, the average HCN emission is weak with a typical ratio of  $L_{\text{HCN}}/L_{\text{CO}} = 1/20$  to  $1/40$  (Gao & Solomon 1998). In the Milky Way, HCN emission is strong only in cloud cores that form high-mass stars. We showed previously that ultraluminous galaxies have abnormally high HCN luminosities (Solomon, Downes, & Radford 1992), with  $L_{\text{HCN}}/L_{\text{CO}} = 1/4$  to  $1/8$ , indicating a higher fraction of the total molecular gas is in dense,  $> 10^4 \text{ cm}^{-3}$ , star-forming cores than in normal galaxies. The densities we derive for the smoothly distributed gas

in the rotating disks (see Table 6) are typically 10 times lower than that needed for HCN excitation, except for the extreme starburst regions Arp220-west, Arp220-east and the disk of Mrk231. The denser gas responsible for the HCN emission (and CS emission) is thus not adequately accounted for in most sources by the “diffuse” CO emitting component that fills the disk.

In Arp 220, the HCN lines we observed have the same velocities as the east and west “nuclei”, so it seems that the east and west “nuclei” alone account for most of the HCN emission. These dense, compact sources have a hydrogen column density of  $0.6 \times 10^{25} \text{ cm}^{-2}$  and mean density of  $20,000 \text{ cm}^{-3}$ , enough to thermalize the lower rotational levels of HCN by a combination of collisions and radiative trapping. Within the Arp 220 east and west sources, the HCN emission may thus have the same intrinsic brightness temperature as the CO(2–1) emission, namely, 50 K (Table 8). Using the sizes and linewidths from Tables 4 and 5, we estimate the HCN luminosity of these two regions alone to be  $L_{\text{HCN}} \approx 7 \times 10^8 \text{ K km s}^{-1} \text{ pc}^2$ , which is 3/4 of the observed total (Solomon, Downes, & Radford 1992). These two regions thus emit only 1/4 of the CO luminosity but most of the HCN luminosity. Their total gas mass of  $1.7 \times 10^9 M_{\odot}$  is already accounted for in the mass budget in Table 9. Thus for Arp 220, only a small increase in the mass budget would be enough to account for the HCN emission.

While some of the HCN emission undoubtedly comes from dense star forming molecular cores embedded in the (relatively) diffuse CO disks of ultraluminous galaxies, it is likely that high density, extreme starburst regions similar to Arp 220 east and west exist in most of the other ultraluminous galaxies in our sample, and are the real sources of most of the HCN emission. Arp 220 is the closest ultraluminous galaxy and has the best resolved structure. The second closest galaxy, Arp 193 (see section 6 and Figs. 10 and 11), also shows evidence of an extreme starburst in the southeast, that appears similar to the strong sources in Arp 220. We suggest that the high-density, extreme starburst regions are the source of much of the HCN luminosity but only a fraction of the CO luminosity. Most are beyond detection at our current resolution in CO emission since their size of  $\approx 100 \text{ pc}$  would be  $< 0''.14$  for all but two of the galaxies (see Table 3). These objects may then add about  $1 \times 10^9 M_{\odot}$ , or 25%, to the total gas mass in galaxies with very high HCN emission. This is less than we estimated in our 1992 paper. In line with this re-interpretation, we note that the galaxy VII Zw 31 has much weaker HCN emission than most of the others in our sample. It also has the largest CO disk, a lower ratio of  $L_{\text{FIR}}/L_{\text{CO}}$  (less star formation per solar mass of gas), and may not have any extreme starburst regions like Arp 220 east or west.



### 10.3. Stability of the molecular disks

The standard parameter for characterizing the stability against local, axisymmetric perturbations of a disk that is supported by differential rotation and random motion is

$$Q = \frac{\sigma_v \kappa}{\pi G \Sigma} \quad , \quad (15)$$

where  $\sigma_v$  is the one-dimensional random velocity dispersion,  $\kappa$  is the local epicyclic frequency, and  $\Sigma$  is the mass surface density. (Safronov 1960; Toomre 1964; Goldreich & Lynden-Bell 1965; for a recent review of the criterion applied to gravitationally coupled stars and gas in a disk, see Jog 1996). If  $Q$  is  $< 1$ , the structure is unstable, and large massive star clusters may form. We used our interferometer data on the sizes, turbulent velocities, rotation velocities, and mass surface densities to estimate the stability of the nuclear disks of the ultraluminous galaxies. In our model rotation curves, the epicyclic frequencies are  $\kappa \approx 2V/R = \text{constant}$  on the rising part of the rotation curve, and  $\kappa \approx \sqrt{2}V/R$  on the flat part of the rotation curve. The objects in our sample have high gas mass fractions and typically have  $Q_{\text{gas}} \leq 2$ , but  $Q_{s+g} < 1$  for stars plus gas (the regime in Fig. 1e of Jog 1996). For Arp 220, we obtain  $Q_{\text{gas}} = 2.2$  at  $R = 480$  pc for the gas alone, but  $Q \sim 1$  for the gas plus stars. For VII Zw 31, at a radius of  $R = 1100$  pc, we obtain  $Q = 1.1$  and  $0.9$  for these two masses. These values suggest the molecular disks of Arp 220 and VII Zw 31 are globally unstable against axisymmetric perturbations and will form massive star clusters.

Empirically, this instability in the central disks appears to produce one or more large clumps of dense molecular gas — the compact, nearly unresolved peaks on the CO maps. Table 12 lists some of these compact regions of dense molecular gas, which we identify with extreme starbursts. Their typical radius of 70 to 100 pc may be the scale on which the two-component (stars + gas) system becomes unstable. Their mean  $\text{H}_2$  density can reach  $2 \times 10^4 \text{ cm}^{-3}$ , and their mass appears to be  $\sim 1 \times 10^9 M_\odot$  of gas initially, which then forms  $\sim 10^6$  OB-type stars over  $10^7$  yr, or  $\sim 1000$  times the number of OB stars in 30 Doradus. The total luminosity of one of these extreme starburst regions is  $3 \times 10^{11}$  to  $1 \times 10^{12} L_\odot$ . The central disk of an ultraluminous IR galaxy typically contains two or three such extreme starburst regions at any given time. It is mainly these regions that provide the input power to the ultraluminous galaxies. They heat the dust in the central disks to typical temperatures of 75 K, (the blackbody fits to the colors measured by IRAS). Since the dust is opaque at  $100 \mu\text{m}$ , the disk radiates as a black body. The typical disk radius is 200 to 300 pc, and the Stefan-Boltzmann formula for the disk as a whole yields a luminosity of the order of  $10^{12} L_\odot$ , the typical output power of the ultraluminous galaxies. If these starbursts occur in the old, pre-merger nuclei, they change them considerably, creating a new cusp with a much greater density of stars. If the extreme starbursts occur slightly outside of the old pre-merger nuclei, they will form new nuclei – new cusps of high stellar density.

#### 10.4. Why stars outshine black holes

The CO disks’ radii of  $\sim 500$  pc and rotation speeds of  $\sim 300$  km s $^{-1}$  yield orbital periods of 10 Myr. If their FIR luminosity of  $\sim 10^{12} L_{\odot}$  comes from new stars, then our estimates of  $L_{\text{FIR}}/M_{\text{new}\star} = 300 L_{\odot} M_{\odot}^{-1}$  imply star forming rates of  $50 M_{\odot} \text{yr}^{-1}$ . The mass of gas plus new stars is  $\sim 6 \times 10^9 M_{\odot}$ , so in 10 rotations of the molecular disks, half the gas turns into new stars.

If part of the  $\sim 10^{12} L_{\odot}$  luminosity came from a black hole accretion disk radiating at  $L \sim 0.1 \dot{m}c^2$ , the accretion rate would be  $\sim 1 M_{\odot} \text{yr}^{-1}$ , so in 10 molecular disk rotations the black hole could only accrete  $\sim 1\%$  of the molecular gas. The other 99% of the gas would continue to form stars over this long period, outshining the black hole.

Alternatively, if the gas fell in faster and created a  $6 \times 10^9 M_{\odot}$  black hole in one or two orbital periods, then the accretion rate would be  $60 M_{\odot} \text{yr}^{-1}$ , and a standard Shakura & Sunyaev (1973) optically thick accretion disk, radiating at one-tenth the Eddington luminosity, would have a luminosity shooting up to  $10^{15} L_{\odot}$  — 1000 times more luminous than the IR ultraluminous galaxies and quasars in the local universe. If the gas fell in rapidly at an accretion rate of  $60 M_{\odot} \text{yr}^{-1}$ , but the luminosity stayed at  $10^{12} L_{\odot}$ , then the accretion disk’s radiative efficiency would be only  $L = 10^{-4} \dot{m}c^2$  — not any more efficient than producing energy from starbursts. Although it is unlikely that such a massive, high-density, accretion flow would be advection dominated (e.g., Rees 1982), if the flow were in this regime, then almost by definition, the accretion disk would not be a luminous object.

The model of rapid accretion to a black hole thus poses more problems than it solves. With a very high accretion rate of  $60 M_{\odot} \text{yr}^{-1}$ , why would the IR ultraluminous galaxies only have an output of  $10^{12} L_{\odot}$  if their power source were a black hole? Why aren’t they as luminous as the powerful quasars at high redshifts, since there is no shortage of fuel? Inversely, if the power source were a black hole accreting at a modest rate of  $1 M_{\odot} \text{yr}^{-1}$ , it would last for  $6 \times 10^9$  years and there would be many more ultraluminous galaxies than are observed. Since the source statistics indicate the ultraluminous phase in mergers lasts for  $\sim 10^8$  years, the more likely answer is that the gas is used up in forming stars – not quasars.

In summary, even in 10 rotations of the molecular disk, a black hole radiating  $10^{12} L_{\odot}$  at high efficiency could accrete only 1% of the molecular disk’s mass. So even though new stars convert matter into energy less efficiently than a standard accretion disk, they make up for this in ultraluminous IR galaxies by occurring in burst, in a 2000 times larger volume, with a 2000 times larger total mass than is available within the Bondi radius  $G M_{\text{bh}}/V^2$  of a supermassive black hole. The molecular disks probably survive for at least 10 rotations.

During this time, at most  $10^7 M_{\odot}$  is accreted to a black hole. The rest of the molecular gas forms stars.

## 11. CONCLUSIONS

1.) *Rotating disks:* At sub-arcsecond resolution, our CO maps of ultraluminous galaxies show rotating disks of molecular gas that has been driven into the centers of the mergers. The maps of Mrk 273 and Arp 220 also show large-scale streamers or tidal tails roughly perpendicular to the nuclear disks.

2.) *CO only moderately opaque:* Model fits show that the observed double-peaked CO spectra, and the peak-to-center contrast in the twin-peaked patterns in CO position-velocity diagrams, are produced by radiative transfer through the rotating disks, in CO that is only moderately opaque. The CO(1–0) opacities are 4 to 10 at the peaks, and lower elsewhere in the disks.

3.) *High turbulence in the molecular disks:* In the Arp 220 disk, the 1-D velocity dispersion of the molecular gas is  $\sigma = 100 \text{ km s}^{-1}$  (FWHM  $230 \text{ km s}^{-1}$ ). This high turbulence is one of the reasons why the CO is less opaque than in quiescent Milky Way molecular clouds. The turbulence also determines the disk thickness, and the heat input to the gas. The turbulent heat input,  $M_{\text{gas}}\Delta V^3/R$ , is  $\sim 10^9 L_{\odot}$ , the same as the output from the  $17 \mu\text{m}$  S(1) line of  $\text{H}_2$ , a principal cooling line (Sturm et al. 1996). The line luminosity is that expected from  $10^9 M_{\odot}$  of gas at  $\sim 100 \text{ K}$ .

4.) *Most of the CO luminosity comes from relatively “low-density” gas:* Except for the compact cores in Mrk 231, Mrk 273, and Arp 220, the molecular disks have true CO brightness temperatures  $\sim 20 \text{ K}$ . This is rather lower than the dust and gas kinetic temperatures, which are  $\sim 65$  to  $100 \text{ K}$ . This implies that the density over most of the molecular disk is relatively low ( $300$  to  $2000 \text{ cm}^{-3}$ ), giving subthermal excitation. The CO(2–1)/(1–0) ratios are also consistent with the CO being subthermally excited.

5.) *The CO lines in the molecular disks come from a continuous medium, not from self-gravitating (“virialized”) clouds:* At the densities of  $10^3 \text{ cm}^{-3}$  needed to explain the observed flux, low-density molecular clouds would be unstable against tidal shear in the rotating disks. Because we also detect high density tracers like HCN and CS, we estimate  $\sim 10\%$  of the gas is in highly opaque, high-density ( $10^5 \text{ cm}^{-3}$ ), self-gravitating clouds that are stable against tidal forces. In the outer disks, however, the CO emission may come from “normal” molecular clouds. In this outer disk gas, the volume filling factor would be  $\sim 0.1$ , the area filling factor 0.3, as in normal galactic disks.

6.) *Low dust flux consistent with lower molecular mass:* Only in Arp 220 is there significant thermal continuum flux from dust at 1.3 mm. The continuum in Mrk 231 at 3 and 1.3 mm is nonthermal. At 3 mm, no thermal continuum is detected from dust, to limits of  $\sim 2$  to 10 mJy, in accord with the gas masses obtained from CO, corresponding to a CO luminosity to gas mass conversion factor about 5 times lower than in self-gravitating clouds in the Milky Way.

7.) *Still lots of gas, nevertheless:* In spite of the “low” gas densities and CO line opacities, the derived gas mass is high; the mass of  $\approx 5 \times 10^9 M_{\odot}$  is equal to the mass of molecular clouds in a large gas rich spiral galaxy. Within the molecular disks, the ratio of gas mass to the enclosed dynamical mass is  $M_{\text{gas}}/M_{\text{dyn}} = 1/6$ . The ratio of gas to total mass surface density,  $\mu/\mu_{\text{tot}}$ , reaches a maximum value of 1/3 within the molecular disks. The ratio  $M_{\text{gas}}/L'_{\text{CO}}$  of gas mass to CO luminosity is about one-fifth of its value in self-gravitating molecular clouds. For the galaxies in this sample, typical ratios are  $M_{\text{gas}}/L'_{\text{CO}} = 0.8 M_{\odot}(\text{K km s}^{-1} \text{ pc}^2)^{-1}$ .

8.) *Extreme Starburst Regions:* Four extreme starbursts are identified in the 3 closest galaxies in the sample including Arp 220, Arp 193 and Mrk 273. They are the most prodigious star formation events in the local universe, each representing about 1000 times as many OB stars as 30 Doradus. They have a characteristic size of only 100 pc, with about  $10^9 M_{\odot}$  of gas and an IR luminosity of  $\approx 3 \times 10^{11} L_{\odot}$  from recently formed OB stars.

Arp 220 has 2 extreme starbursts. The integrated CO and 1.3 mm continuum maps of Arp 220 show two compact peaks. The west nucleus, at  $cz_{\text{lsr}} = 5340 \text{ km s}^{-1}$ , is the same as the cm-radio and IR west peak. the CO east gas at  $5330 \text{ km s}^{-1}$ , is associated with the cm-radio east peak and its OH megamasers. The CO east gas at  $5650 \text{ km s}^{-1}$  is associated with the ionized gas in the *K*-band east nucleus. The IR luminosity of the compact peaks in Arp 220 can be explained by extreme starbursts in their early phases. The cm-radio continuum, the CO intensity, and the 1.3 mm dust flux all suggest the currently most active starburst is the west peak. Arp 220 west also shows a complex velocity structure which may indicate a bar in formation or a huge molecular outflow. The mass of these compact regions is dominated by molecular gas and young stars, not by a bulge population.

9.) *Regions of dense molecular gas are regions of extreme starbursts:* We suggest that the HCN emission, which is very strong in most ultraluminous galaxies, originates in the high-density, extreme starburst regions similar to Arp 220 east and west. These regions are larger than ordinary GMCs, but are filled with molecular gas at a density usually found only in small cloud cores. They do not produce most of the CO luminosity, but they do emit most of the HCN luminosity. This explains the high HCN luminosity and directly relates the HCN emission to star formation, as we suggested previously (Solomon et al.

1992).

10.) *Ultraluminous galaxies are powered by starbursts, not AGNs:* The CO data show the gas in ultraluminous galaxies is in extended disks that cannot intercept all the power of central AGNs, if they exist. As a rule of thumb, if you can see the AGN in the UV/visible, then it is not heavily absorbed, and cannot be responsible for the far-IR/sub-mm luminosity. Furthermore, if the rotating molecular disks were very thin (30 pc) and extended all the way in to central AGNs, then their dust would be very hot, emitting most of their power at 10 to 20  $\mu\text{m}$ . In fact, most of the dust (and gas) observed in the ultraluminous IR galaxies is cool (70 K), emitting at 60 to 100  $\mu\text{m}$  — the usual temperature of dust in molecular clouds heated by starbursts. We conclude that in ultraluminous galaxies — even in Mrk 231 that hosts a quasar — the far IR luminosity is powered by extreme starbursts in the molecular disks, not by dust-enshrouded quasars.

We thank the telescope operators at Plateau de Bure and the IRAM staff astronomers for their help in taking the data, A. Dutrey for use of her disk modelling program, C.M. Walmsley for the escape probability program, and S. Guilloteau, R. Lucas, and J. Wink for help in data reduction. We also thank H. Ungerechts for re-measuring some CO fluxes at the IRAM 30 m telescope, and P. van der Werf, R. Genzel, and N. Scoville for helpful talks. We thank the referee for many helpful comments. P.M.S. is grateful for a Research Award from the Alexander von Humboldt Foundation and for a senior scientific fellowship from the North Atlantic Treaty Organization.

## REFERENCES

- Allen, D.A. 1976, *ApJ*, 207, 367
- Armus, L., Heckman, T.M., & Miley, G.K. 1987, *AJ*, 94, 831
- Armus, L., Heckman, T.M., & Miley, G.K. 1989, *ApJ*, 347, 727
- Armus, L., Heckman, T.M., & Miley, G.K. 1990, *ApJ*, 364, 471
- Armus, L., Mazzarella, J.M., Graham, J.R., Soifer, B.T., Neugebauer, G., Matthews, K., & Gaume, R.A. 1992, *BAAS*, 24, 728
- Armus, L., Surace, J.A., Soifer, B.T., Matthews, K., Graham, J.R., & Larkin, J.E. 1994, *AJ*, 108, 76
- Armus, L., Shupe, D.L., Matthews, K., Soifer, B.T., & Neugebauer, G. 1995a, *ApJ*, 440, 200
- Armus, L., Neugebauer, G., Soifer, B.T., & Matthews, K. 1995b, *AJ*, 110, 2610
- Asatryan, A.S., Petrosian, A.R., & Börngen, F. 1990, in *Paired and Interacting Galaxies*, ed. J.W. Sulentic, W.C. Keel, & C.M. Telesco, NASA CP-3098, (Washington DC: GPO), 201
- Baan, W.A., & Haschick, A.D. 1987, *ApJ*, 318, 139
- Baan, W.A., & Haschick, A.D. 1995, *ApJ*, 454, 745
- Baan, W.A., van Gorkom, J., Haschick, A.D., & Mirabel, F.I. 1987, *ApJ*, 313
- Becklin, E.E., & Wynn-Williams, C.G. 1987, in *Star Formation in Galaxies*, ed. C.J. Lonsdale Persson (NASA CP-2466; Washington, DC:GPO), 643
- Binney, J., & Tremaine, S. 1987, *Galactic Dynamics*, (Princeton:Princeton Univ. Press), 76
- Boksenberg, A., Carswell, R.F., Allen, D.A., Fosbury, R.A.E., Penston, M.V., & Sargent, W.L.W. 1977, *MNRAS*, 178, 451
- Borgeest, U., Dietrich, M., Hopp, U., Kollatschny, W., Schramm, K.J. 1991, *A&A*, 243, 93
- Bryant, P.M., & Scoville, N.Z. 1996, *ApJ*, 457, 678
- Burbidge, G. 1996, *A&A*, 309, 9
- Carico, D.P., Keene, J., Soifer, B.T., & Neugebauer, G. 1992, *PASP*, 104, 1086
- Carilli, C.L., Wrobel, J.M., & Ulvestad, J.S. 1998, *AJ*, 115, 928
- Chini, R., Krügel, E., Kreysa, E., & Gemünd, H.P. 1989, *A&A*, 216, L5
- Condon, J.J., Huang, Z.P., Yin, Q.F., & Thuan, T.X. 1991, *ApJ*, 378, 65
- Crawford, T., Marr, J., Partridge, B., & Strauss, M.A. 1996, *ApJ*, 460, 225

- Cutri, R.M., Rieke, G.H., & Lebofsky, M.J. 1984, *ApJ*, 287, 566
- Depoy, D.L., Becklin, E.E., & Geballe, T.R. 1987, *ApJ*, 316, L63
- Diamond, P.J., Norris, R.P., Baan, W.A., & Booth, R.S. 1989, *ApJ*, 340, L49
- Djorgovski, S., de Carvalho, R.R., & Thompson, D.J. 1990, *AJ*, 99, 1414
- Downes, D., Solomon, P.M., & Radford, S.J.E. 1993, *ApJ*, 414, L13
- Doyon, R., Wells, M., Wright, G.S., Joseph, R.D., Nadeau, D., & James, P.A. 1994, *ApJ*, 437, L23
- Dudley, C.C., & Wynn-Williams, C.G. 1997, *ApJ*, 488, 720
- Dutrey, A., Guilloteau, S., & Simon, M. 1994, *A&A*, 286, 149
- Eales, S.A., Wynn-Williams, C.G., & Duncan, W.D. 1989, *ApJ*, 339, 859
- Emerson, J.P., et al. 1984, *Nature*, 311, 237
- Fairclough, J.H. 1986, *MNRAS*, 219, 1p
- Fazio, G.G. 1978, in *Infrared Astronomy*, ed. G. Setti & G.G. Fazio, Reidel, Dordrecht, 25
- Fischer, J., et al. 1998, in *ISO to the Peaks*, ed. M. Kessler & M. Perry, ESTEC, Noordwijk, in press
- Gao, Yu, & Solomon, P.M. 1998, in preparation
- Gatley, I., Becklin, E.E., Werner, M.W., & Harper, D.A. 1978, *ApJ*, 220, 822
- Genzel, R., et al. 1998, *ApJ*, 498, 579
- Goldader, J.D., Joseph, R.D., Doyon, R., & Sanders, D.B. 1995, *ApJ*, 444, 97
- Goldreich, P., & Lynden-Bell, D. 1965, *MNRAS*, 130, 125
- Graham, J.R., Carico, D.P., Matthews, K., Neugebauer, G., Soifer, B.T., & Wilson, T.D. 1990, *ApJ*, 354, L5
- Guilloteau, S., et al. 1992, *A&A*, 262, 624
- Hamilton, D., & Keel, W.C. 1987, *ApJ*, 321, 211
- Hoyle, F., & Burbidge, G. 1996, *A&A*, 309, 335
- Hutchings, J.B., & Neff, S.G. 1987, *AJ*, 92, L14
- Jennings, R.B. 1975, in *H II Regions and Related Topics*, ed. T.L. Wilson & D. Downes (Berlin: Springer) 137
- Jog, C.J. 1996, *MNRAS*, 278, 209
- Kazès, I., Mirabel, I.F., & Combes, F. 1988, *IAU Circ.* 4629

- Kennicutt, R.C., & Chu, Y.H. 1994, in *Violent Star Formation from 30 Doradus to QSOs*, ed. G. Tenorio-Tagle, Cambridge: Cambridge Univ. Press, 1
- Keto, E., Ball, R., Arens, J., Jernigan, G., & Meixner, M. 1992, *ApJ*, 387, L17
- Kim, D.C., Sanders, D.B., Veilleux, S., Mazzarella, J.M., & Soifer, B.T. 1995, *ApJS*, 98, 129
- Klaas, U., & Elsässer, H. 1991, *A&AS*, 90, 33
- Klaas, U., & Elsässer, H. 1993, *A&AS*, 99, 71
- Knapen, J.H., Laine, S., Yates, J.A., Robinson, A., Richards, A.M.S., Doyon, R., & Nadeau, D. 1997, *ApJ*, in press
- Kobayashi, Y., Sato, S., Yamashita, T., Shiba, H., & Takami, H. 1993, *ApJ*, 404, 94
- Kollatschny, W., Dietrich, M., Borgeest, U., & Schramm, K.J. 1991, *A&A*, 249, 57
- Koski, A.T. 1978, *ApJ*, 223, 56
- Krabbe, A., Colina, L., Thatte, N., & Kroker, H. 1997, *ApJ*, 476, 98
- Krügel, E., & Siebenmorgen, R. 1994, *A&A*, 288, 929
- Larkin, J.E., Armus, L., Knop, R.A., Matthews, K., & Soifer, B.T. 1995, *ApJ*, 452, 599
- Leitherer, C., & Heckman, T.M. 1995, *ApJS*, 96, 9
- Lipari, S., Colina, L., & Macchetto, F. 1994, *ApJ*, 427, 174
- Lonsdale, C.J., Smith, H.E., & Lonsdale, C.J. 1993, *ApJ*, 405, L9
- Lonsdale, C.J., Diamond, P.J., Smith, H.E., & Lonsdale, C.J. 1998, *ApJ*, 493, L13
- Lutz, D., et al. 1996, *A&A*, 315, L137
- Majewski, S.R., Hereld, M., Koo, D.C., Illingworth, G.D., & Heckman, T.M. 1993, *ApJ*, 402, 125
- Malkan, M.A., & Sargent, W.L.W. 1982, *ApJ*, 254, 22
- Martin, J.M., Bottinelli, L., Dennefeld, M., Gouguenheim, L., & Le Squeren, A.M. 1989, *A&A*, 208, 39
- Matthews, K., Neugebauer, G., McGill, T., & Soifer, B.T. 1987, *AJ*, 94, 297
- Melnick, J., & Mirabel, I.F. 1990, *A&A*, 231, L19
- Mestel, L. 1963, *MNRAS*, 126, 553
- Mezger, P.G., 1985, in *Birth & Infancy of Stars*, ed. R. Lucas, A. Omont, & R. Stora, Elsevier, Amsterdam, 31
- Miles, J.W., Houck, J.R., Hayward, T.L., & Ashby, M.L.N. 1996, *ApJ*, 465, 191



- Murphy, T.W., Armus, L., Matthews, K., Soifer, B.T., Mazzarella, J.M., Shupe, D.L., Strauss, M.A., & Neugebauer, G. 1996, AJ, 111, 1025
- Neff, S.G., & Ulvestad, J.S. 1988, AJ, 96, 841
- Norris, R.P. 1988, MNRAS, 230, 345
- Norris, R.P., Baan, W.A., Haschick, A.D., Booth, R.S., & Diamond, P.J. 1985, MNRAS, 213, 821
- Oort, J.H. 1977, ARAA, 15, 295
- Panagia, N. 1977, in *Infrared & Submillimeter Astronomy*, ed. G.G. Fazio, Reidel, Dordrecht, 43
- Parker, J.W. 1993, AJ, 106, 560
- Planesas, P., Mirabel, I.F., & Sanders, D.B. 1991, ApJ, 370, 172
- Preuss, E., & Fosbury, A.E. 1983, MNRAS, 204, 783
- Radford, S.J.E., Solomon, P.M., & Downes, D. 1991a, ApJ, 368, L15
- Radford, S.J.E., et al. 1991b, in *Dynamics of Galaxies and Their Molecular Cloud Distributions*, ed. F. Combes & F. Casoli (Dordrecht:Kluwer), 303
- Rees, M.J., 1982, in *The Galactic Center*, ed. G.R. Riegler & R.D. Blandford, Am. Inst. of Physics Conf. Proc. 83, (New York:AIP), 166
- Rieke, G.H. 1976, ApJ, 210, L5
- Rigopoulou, D., Lawrence, A., & Rowan-Robinson, M. 1996, MNRAS, 278, 1049
- Roche, P.F., Aitken, D.K., & Whitmore, B. 1983, MNRAS, 205, 21P
- Safronov, V.S. 1960, Ann d'Ap, 23, 979
- Sage, L.J., & Solomon, P.M. 1987, ApJ, 321, L103
- Sanders, D.B., Young, J.S., Scoville, N.Z., Soifer, B.T., & Danielson, G.E. 1987, ApJ, 312, L5
- Sanders, D.B., Phinney, S., Neugebauer, G., Soifer, B.T., & Matthews, K. 1989, ApJ 347, 29
- Sargent, W.L.W. 1972, ApJ, 173, 7
- Sargent, W.L.W., & Steidel, C.C. 1990, ApJ, 359, L37
- Schmelz, J.T., Baan, W.A., & Haschick, A.D. 1988, ApJ, 329, 142
- Schmidt, G.D., & Miller, J.S. 1985, ApJ, 290, 517

- Scoville, N.Z., Sanders, D.B., Sargent, A.I., Soifer, B.T., & Tinney, C.G. 1989, *ApJ*, 345, L25
- Scoville, N.Z., Sargent, A.I., Sanders, D.B., & Soifer, B.T. 1991, *ApJ*, 366, L5
- Scoville, N.Z., Yun, M.S., & Bryant, P.M. 1997, *ApJ*, 484, 702
- Scoville, N.Z., Evans, A.S., Dinshaw, N., Thompson, R., Rieke, M., Schneider, G., Low, F.J., Hines, D., Stobie, B., Becklin, E., & Epps, H. 1998, *ApJ*, 492, L107
- Shakura, N.I., & Sunyaev, R.A. 1973, *A&A*, 24, 337
- Shaya, E.J., Dowling, D.M., Currie, D.G., Faber, S.M., & Groth, E.J. 1994, *AJ*, 107, 1675
- Shier, L.M., Rieke, M.J., & Rieke, G.H. 1994, *ApJ*, 433, L9
- Shier, L.M., Rieke, M.J., & Rieke, G.H. 1996, *ApJ*, 470, 222
- Skinner, C.J., Smith, H.A., Sturm, E., Barlow, M.J., Cohen, R.J., & Stacey, G.J. 1997, *Nature*, 386, 472
- Smith, C.H., Aitken, D.K., & Roche, P.F. 1989, 241, 425
- Smith, D.A., Herter, T., Haynes, M.P., Beichman, C.A., Gautier, T.N. 1995, *ApJ*, 439, 623
- Smith, D.A., Herter, T., Haynes, M.P., Beichman, C.A., Gautier, T.N. 1996, *ApJS*, 104, 217
- Smith, H.E., Lonsdale, C.J., Lonsdale, C.J., 1998a, *ApJ*, 492, 137
- Smith, H.E., Lonsdale, C.J., Lonsdale, C.J., & Diamond, P.J., 1998b, *ApJ*, 493, L17
- Smith, P.S., Schmidt, G.D., Allen, R.G., & Angel, J.R.P. 1995, *ApJ*, 444, 146
- Solomon, P.M., Downes, D., Radford, S.J.E., 1992, *ApJ*, 387, L55
- Solomon, P.M., Downes, D., Radford, S.J.E., & Barrett, J.W. 1997, *ApJ*, 478, 144
- Sopp, H.M., & Alexander, P. 1991, *MNRAS*, 251, 112
- Staveley-Smith, L., Cohen, R.J., Chapman, J.M., Pointon, L., Unger, S.W. 1987, *MNRAS*, 226, 689
- Sturm, E., et al. 1996, *A&A*, 315, L133
- Surace, J.A., Sanders, D.B., Vacca, W.D., Veilleux, S., & Mazzarella, J.M. 1998, *ApJ*, 492, 116
- Taylor, G.B., Vermeulen, R.C., Pearson, T.J., Readhead, A.C.S., Henstock, D.R., Browne, I.W.A., & Wilkinson, P.N. 1994, *ApJS*, 95, 345
- Toomre, A. 1964, *ApJ*, 139, 1217
- Ulvestad, J.S., & Wilson, A.S. 1984, *ApJ*, 278, 544

- van der Werf, P.P. 1996, in *Cold Gas at High Redshift*, ed. M.N. Bremer, H.J.A. Röttgering, & C.L. Carilli, (Kluwer: Dordrecht), 37
- van der Werf, P.P., & Israel, F. 1998, in preparation.
- Veilleux, S., Kim, D.C., Sanders, D.B., Mazzarella, J.M., & Soifer, B.T. 1995, *ApJS*, 98, 171
- Womble, D.S., Junkkarinen, V.T., Cohen, R.D., & Burbidge, E.M. 1990, *AJ*, 100, 1785
- Woody, D.P., et al. 1989, *ApJ*, 337, L41
- Yun, M.S., & Scoville, N.Z. 1995, *ApJ*, 451, L45
- Zenner, S., & Lenzen, R. 1993, *A&AS*, 101, 363
- Zhao, J.H., Anantharamaiah, K.R., Goss, W.M., & Viallefond, F. 1996, *ApJ*, 472, 54
- Zwicky, F. 1971, *Catalogue of Selected Compact Galaxies and Post-Eruptive Galaxies*, Guemlingen, Switzerland
- Zylka, R., Mezger, P.G., Ward-Thompson, D., Duschl, W.J., & Lesch, H. 1995, *A&A*, 297, 83

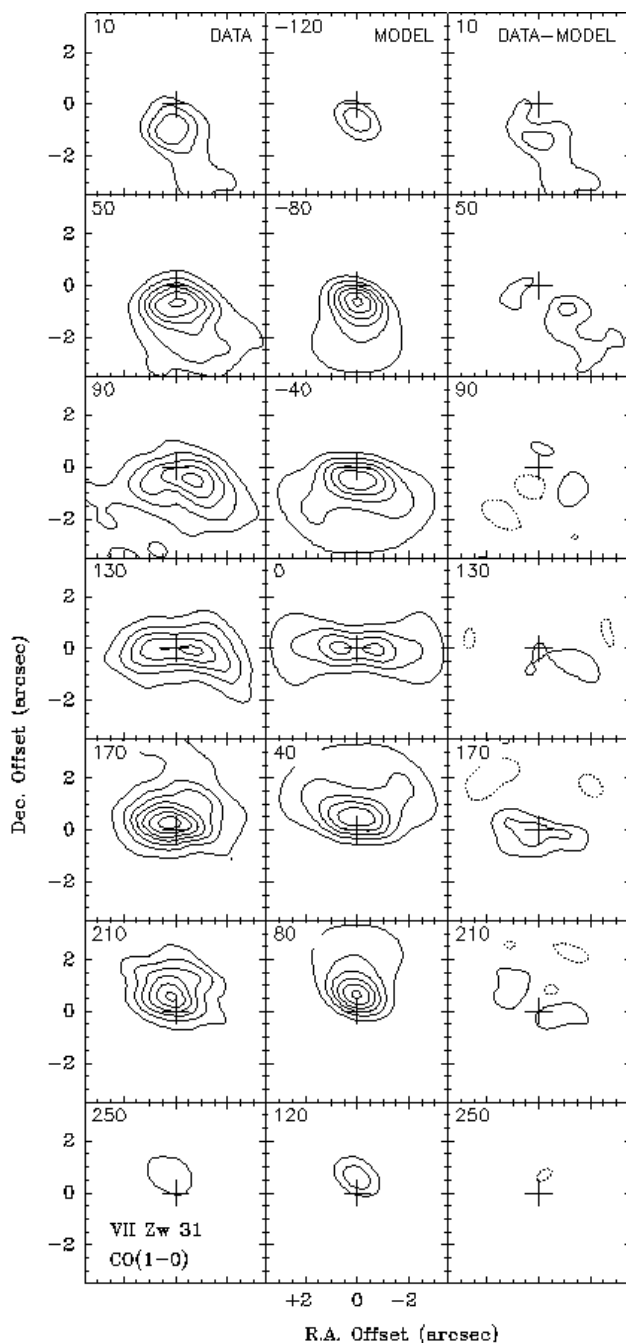


Fig. 1.— **VII Zw 31** : *left*: CO(1–0) in  $40 \text{ km s}^{-1}$  channels. Radial velocities ( $\text{km s}^{-1}$ , upper left of each box) are relative to  $109.380 \text{ GHz}$  ( $c z_{\text{lsr}} = 16147 \text{ km s}^{-1}$ ). Contour unit:  $11 \text{ mJy beam}^{-1}$ , with  $T_b/S = 88 \text{ K/Jy}$ . Beam =  $1''.4 \times 0''.8$ . The cross at (0,0) is  $05^{\text{h}}16^{\text{m}}46.^{\text{s}}51$ ,  $79^{\circ}40'12.''8$  (J2000). *middle*: Maps from the model, with same contours and resolution as the data. *right*: Data minus model, with same contour unit.

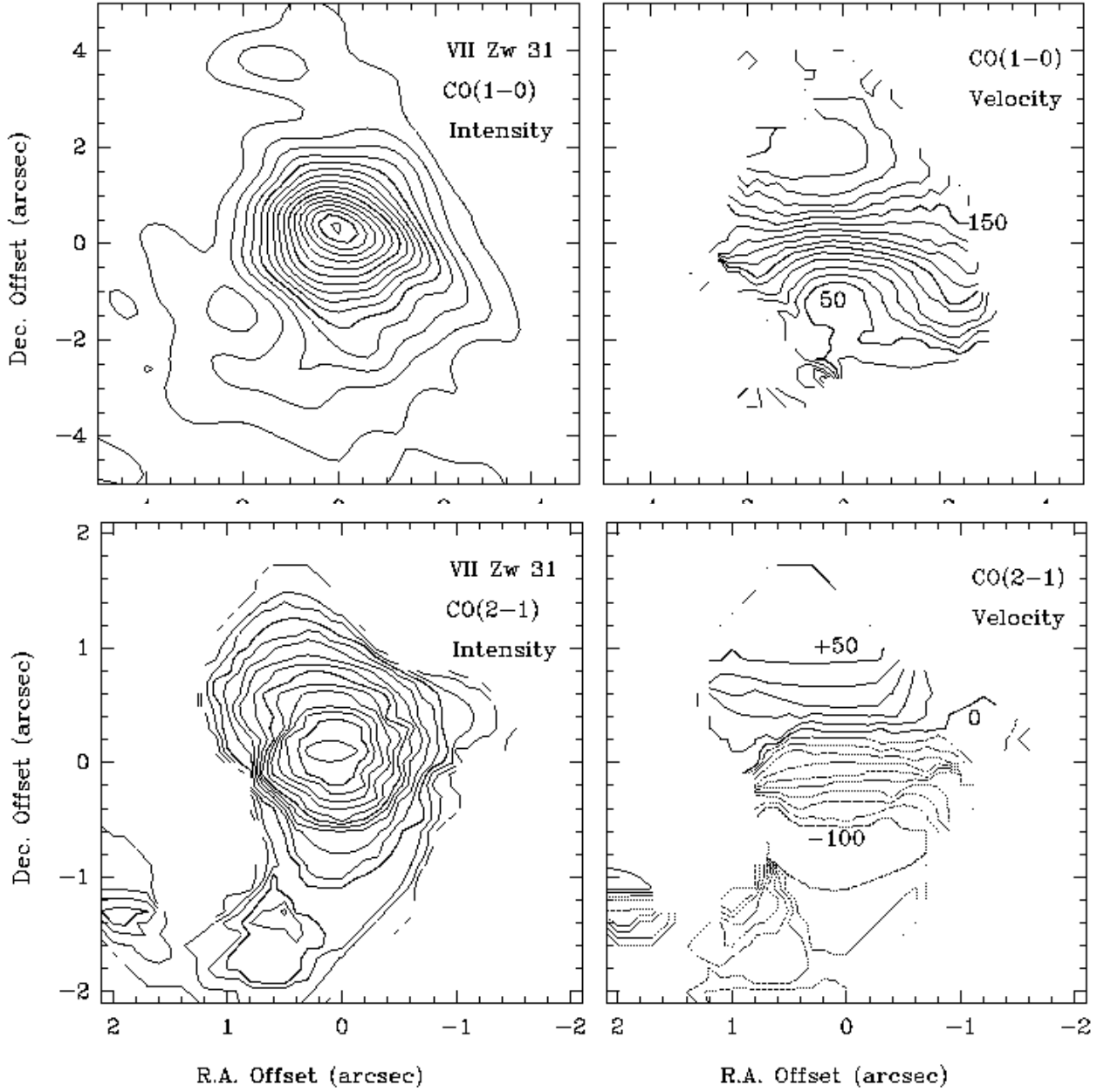


Fig. 2.— **VII Zw 31** : *upper left*: CO(1-0) integrated over  $(-40, +260 \text{ km s}^{-1})$ . Beam  $= 1''.4 \times 0''.8$ . Contour step  $1.2 \text{ Jy beam}^{-1} \text{ km s}^{-1}$ , with  $T_b/S = 88 \text{ K/Jy}$ . *upper right*: Velocity contours in steps of  $10 \text{ km s}^{-1}$  relative to  $109.380 \text{ GHz}$  ( $c z_{\text{lsr}} = 16147 \text{ km s}^{-1}$ ). Labels are in  $\text{km s}^{-1}$ . *lower left*: CO(2-1) integrated over  $(-140, +80 \text{ km s}^{-1})$ . Beam  $1''.1 \times 0''.8$ . Contours: 2 to 16 by 1, in units of  $1.6 \text{ Jy beam}^{-1} \text{ km s}^{-1}$ , with  $T_b/S = 30 \text{ K/Jy}$ . *lower right*: Velocity contours in steps of  $10 \text{ km s}^{-1}$  relative to  $218.650 \text{ GHz}$  ( $c z_{\text{lsr}} = 16300 \text{ km s}^{-1}$ ). Labels are in  $\text{km s}^{-1}$ . Center position in all maps is  $05^{\text{h}}16^{\text{m}}46.^{\text{s}}51, 79^{\circ}40'12.''5$  (J2000).

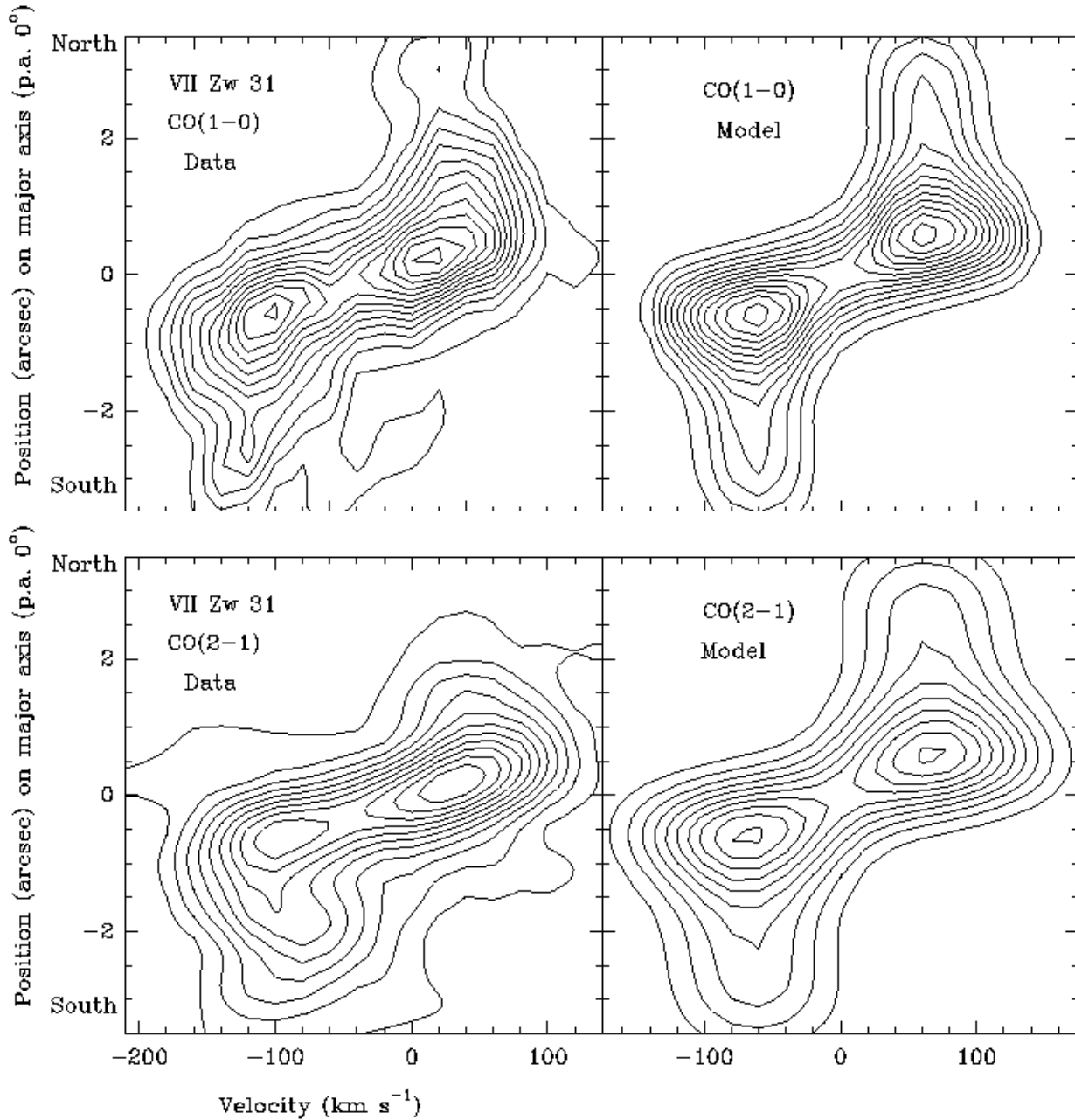


Fig. 3.— **VII Zw 31** : Position-velocity cuts in declination, with zero position at  $05^{\text{h}}16^{\text{m}}46.^{\text{s}}51$ ,  $79^{\circ}40'12.''5$  (J2000). *upper left*: CO(1–0) in  $1''.4 \times 0''.8$  beam. Contour step:  $6 \text{ mJy beam}^{-1}$ , with  $T_b/S = 88 \text{ K/Jy}$ . Velocity is relative to  $109.380 \text{ GHz}$  ( $c z_{\text{lsr}} = 16147 \text{ km s}^{-1}$ ). *upper right*: Predicted CO(1–0) from the model, with same contours and resolution as for the data. *lower left*: CO(2–1) in  $1''.1 \times 0''.8$  beam. Contours: 8 to 90, in steps of  $4.9 \text{ mJy beam}^{-1}$ , with  $T_b/S = 30 \text{ K/Jy}$ . Velocity is relative to  $218.650 \text{ GHz}$  ( $c z_{\text{lsr}} = 16300 \text{ km s}^{-1}$ ). *lower right*: Predicted CO(2–1) from the model, with same contours and resolution as for the data.

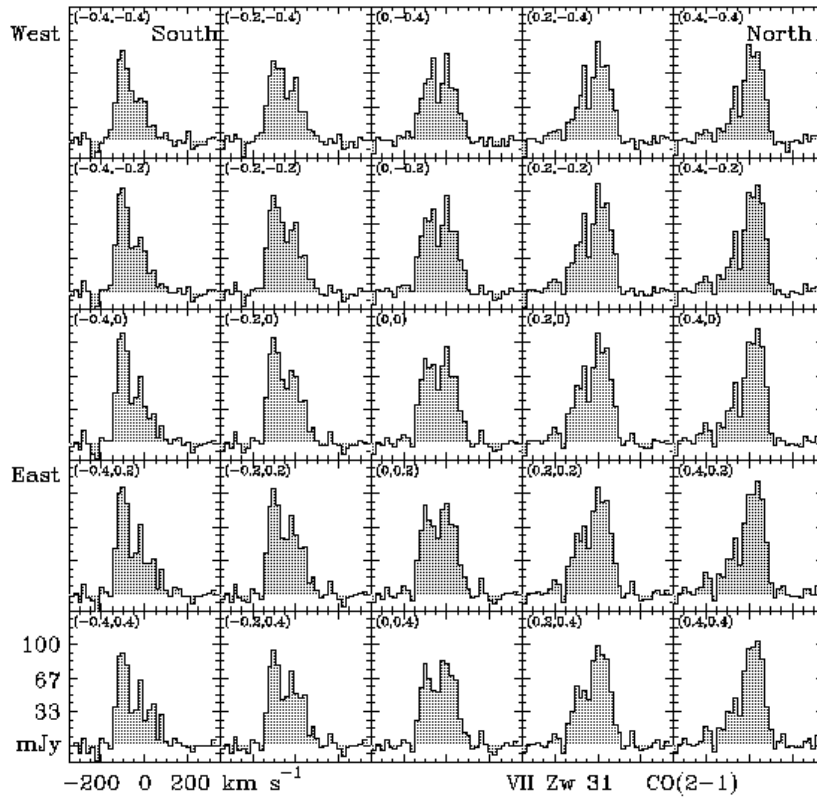
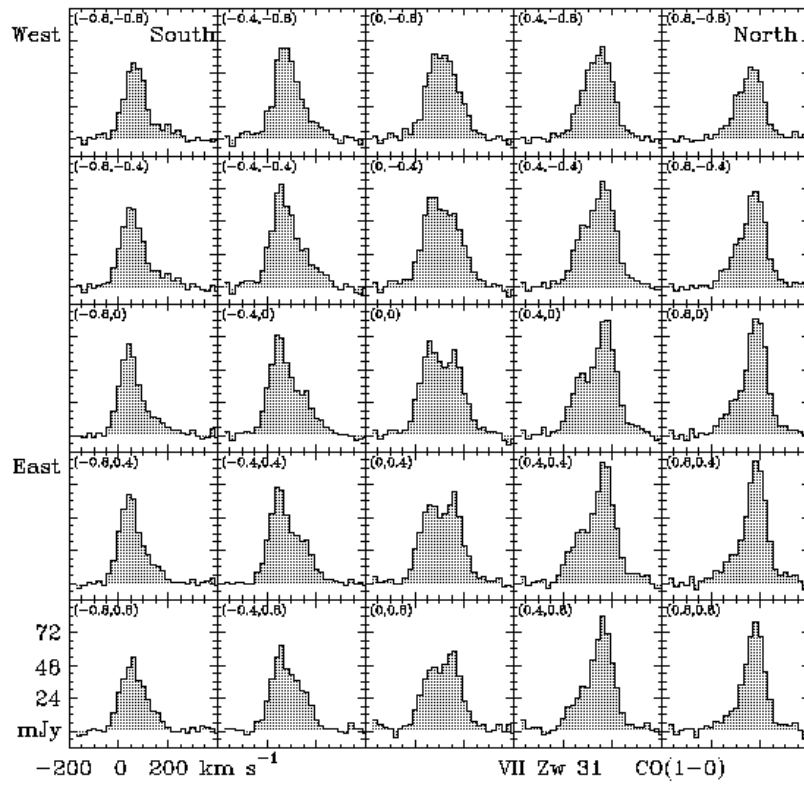


Fig. 4.— **VII Zw 31** : (a), *upper*: CO(1–0) spectra vs. radial velocity relative to 109.380 GHz ( $cz_{\text{lsr}} = 16147 \text{ km s}^{-1}$ ). In the upper left of each box are offsets (arcsec) on the kinematic major and minor axes. Beam =  $1''.4 \times 0''.8$ , with  $T_b/S = 88 \text{ K/Jy}$ .  
(b), *lower*: CO(2–1) spectra vs. radial velocity relative to 218.650 GHz ( $cz_{\text{lsr}} = 16300 \text{ km s}^{-1}$ ). In the upper left of each box are offsets (arcsec) on the kinematic major and minor axes. Beam  $1''.1 \times 0''.8$ . The (0,0) position in both diagrams is  $05^{\text{h}}16^{\text{m}}46.^{\text{s}}51, 79^{\circ}40'12.''5$  (J2000).



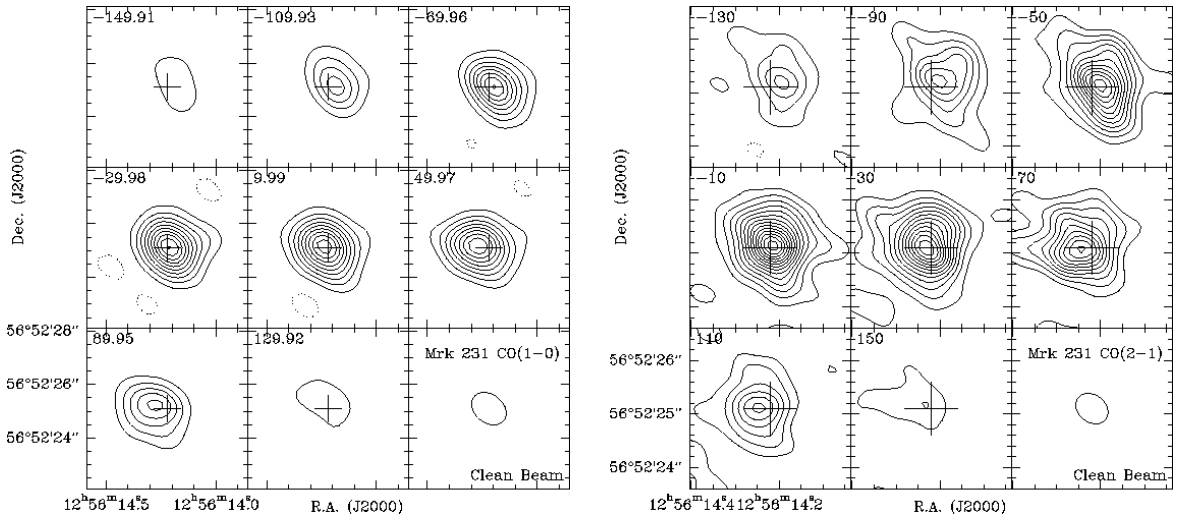


Fig. 5.— **Mrk 231** : (a), left: CO(1–0) in  $40 \text{ km s}^{-1}$  channels. A  $63 \text{ mJy}$  continuum point source has been subtracted at the CO centroid (cross). Radial velocities ( $\text{km s}^{-1}$ , upper left of each box) are relative to  $110.602 \text{ GHz}$  ( $cz_{\text{lsr}} = 12656 \text{ km s}^{-1}$ ). Contour unit:  $20 \text{ mJy beam}^{-1}$ . Beam =  $1''.3 \times 1''.1$  (lower right) with  $T_b/S = 70 \text{ K/Jy}$ .

(b), right: CO(2–1) in  $40 \text{ km s}^{-1}$  channels. A  $36 \text{ mJy}$  continuum point source has been subtracted at the CO centroid (cross). Radial velocities ( $\text{km s}^{-1}$ , upper left of each box) are relative to  $221.204 \text{ GHz}$  ( $cz_{\text{lsr}} = 12650 \text{ km s}^{-1}$ ). Contour unit:  $25 \text{ mJy beam}^{-1}$ . Beam =  $0''.7 \times 0''.5$  (lower right) with  $T_b/S = 75 \text{ K/Jy}$ .

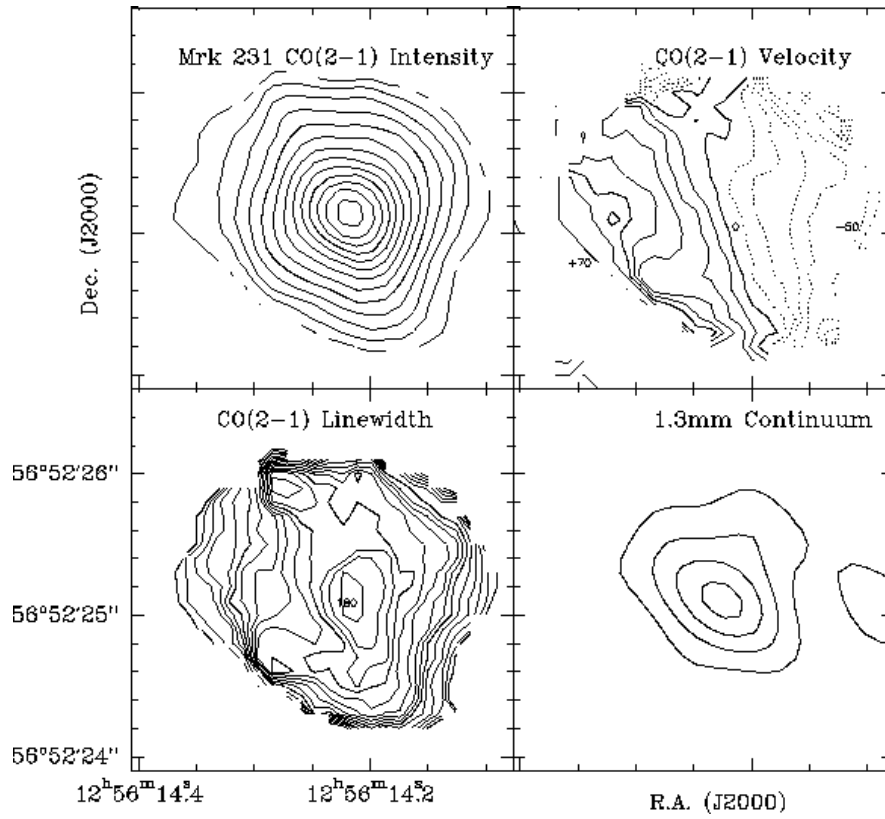
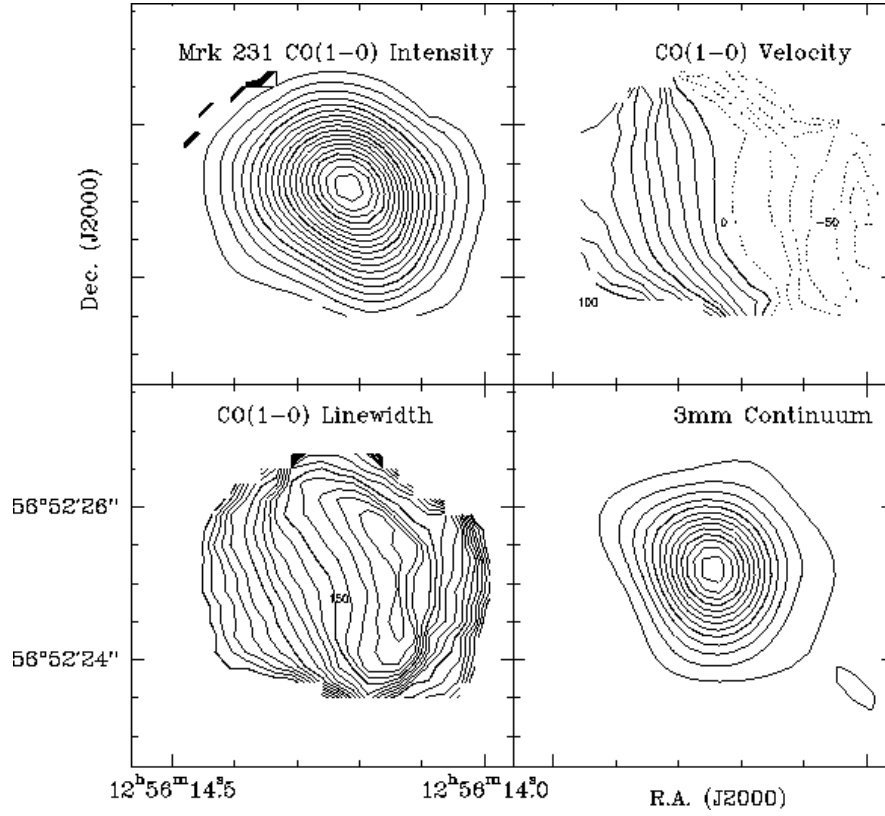


Fig. 6.— **Mrk 231** :

— *upper*: CO(1–0) integrated intensity, velocity, linewidth (FWHM), and the 3 mm continuum. The continuum source has been subtracted from the CO data. Integration limits:  $(-180, +200 \text{ km s}^{-1})$ . Beam =  $1''.3 \times 1''.1$ . Contours:

*integrated CO*: 1 to 18 by 1, in units of  $2 \text{ Jy beam}^{-1} \text{ km s}^{-1}$ , with  $T_b/S = 70 \text{ K/Jy}$ ;

*CO velocity*:  $-60$  to  $+100 \text{ km s}^{-1}$ , in steps of  $10 \text{ km s}^{-1}$  relative to  $110.602 \text{ GHz}$  ( $cz_{\text{lsr}} = 12656 \text{ km s}^{-1}$ ). Labels are in  $\text{km s}^{-1}$ ;

*CO linewidth*:  $50$  to  $190 \text{ km s}^{-1}$  in steps of  $10 \text{ km s}^{-1}$ . Labels are in  $\text{km s}^{-1}$ .

*3 mm continuum*: 1 to 13 by 1, in units of  $4 \text{ mJy}$ .

— *lower*: CO(2–1) integrated intensity, velocity, linewidth (FWHM), and the 1.3 mm continuum. The continuum source has been subtracted from the CO data. Integration limits:  $(\pm 180 \text{ km s}^{-1})$ . Beam =  $0''.7 \times 0''.5$ . Contours:

*integrated CO*: 1 to 13 by 1, in units of  $5 \text{ Jy beam}^{-1} \text{ km s}^{-1}$ , with  $T_b/S = 75 \text{ K/Jy}$ ;

*CO velocity*:  $-60$  to  $+70 \text{ km s}^{-1}$ , in steps of  $10 \text{ km s}^{-1}$  relative to  $221.204 \text{ GHz}$  ( $cz_{\text{lsr}} = 12650 \text{ km s}^{-1}$ ). Labels are in  $\text{km s}^{-1}$ ;

*CO linewidth*:  $50$  to  $180 \text{ km s}^{-1}$  in steps of  $10 \text{ km s}^{-1}$ . Labels are in  $\text{km s}^{-1}$ .

*1.3 mm continuum*: 1 to 4 by 1, in units of  $8 \text{ mJy}$ .

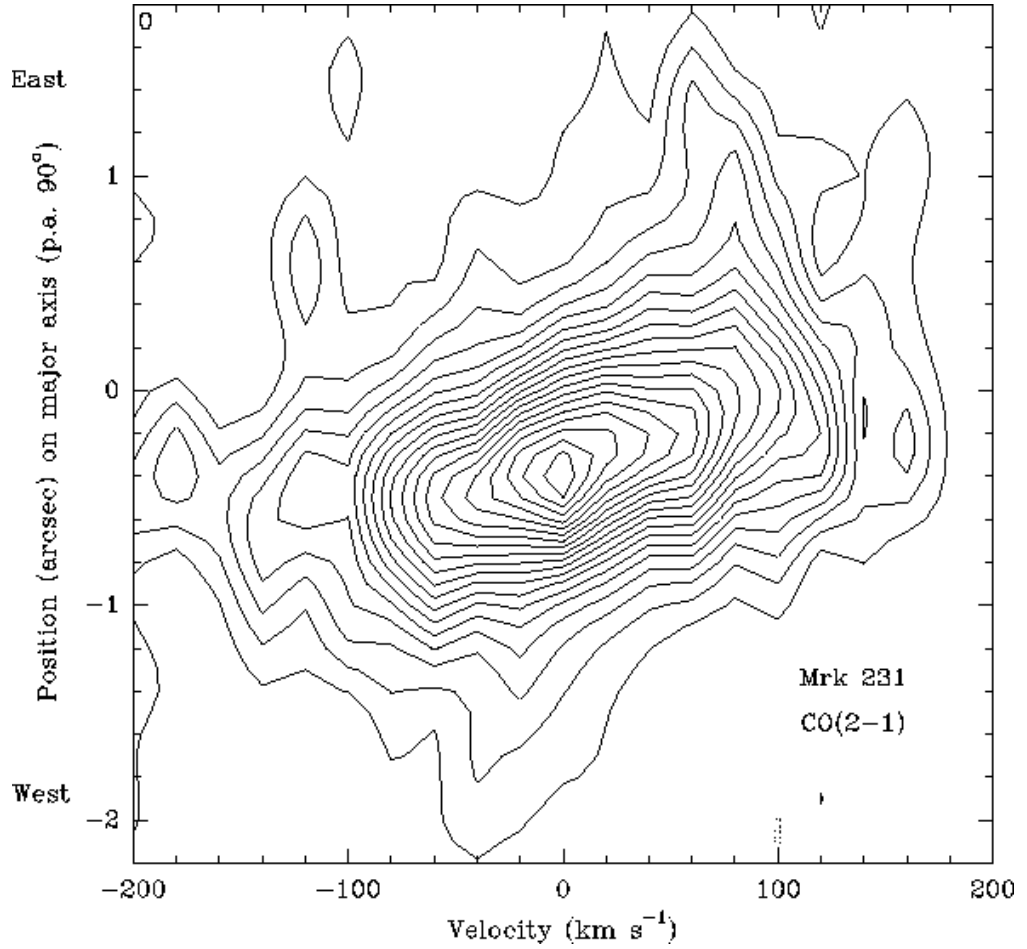


Fig. 7.— **Mrk 231** : CO(2-1) position-velocity diagram along the line of nodes (p.a.  $90^\circ$ ). Contour levels are 1 to 19, in units of  $20 \text{ mJy beam}^{-1}$ , with  $T_b/S = 75 \text{ K/Jy}$ . Beam =  $0''.7 \times 0''.5$ . The (0,0) position is  $12^{\text{h}}56^{\text{m}}14.^{\text{s}}260$ ,  $56^\circ52'25.''13$  (J2000). Velocity is relative to  $221.204 \text{ GHz}$  ( $cz_{\text{lsr}} = 12650 \text{ km s}^{-1}$ ). The continuum source has been subtracted from the CO data.

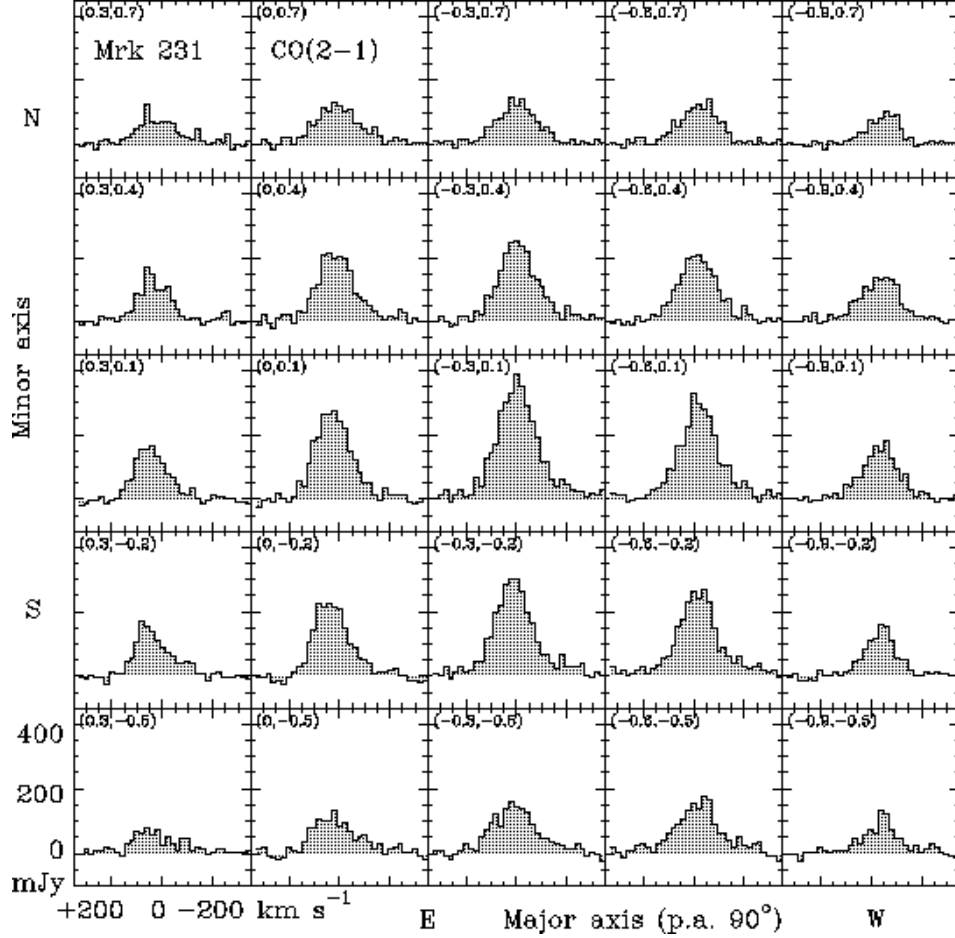


Fig. 8.— **Mrk 231** : CO(2–1) spectra vs. radial velocity relative to 221.204 GHz ( $c z_{\text{lsr}} = 12650 \text{ km s}^{-1}$ ; the velocity scale is reversed to emphasize the symmetry of the profiles). In the upper left of each box are offsets (arcsec) on the kinematic major and minor axes. The (0,0) position is  $12^{\text{h}}56^{\text{m}}14.^{\text{s}}260, 56^{\circ}52'25.''13$  (J2000). Beam =  $0''.7 \times 0''.5$ , with  $T_b/S = 75 \text{ K/Jy}$ . The continuum source has been subtracted from the CO data.

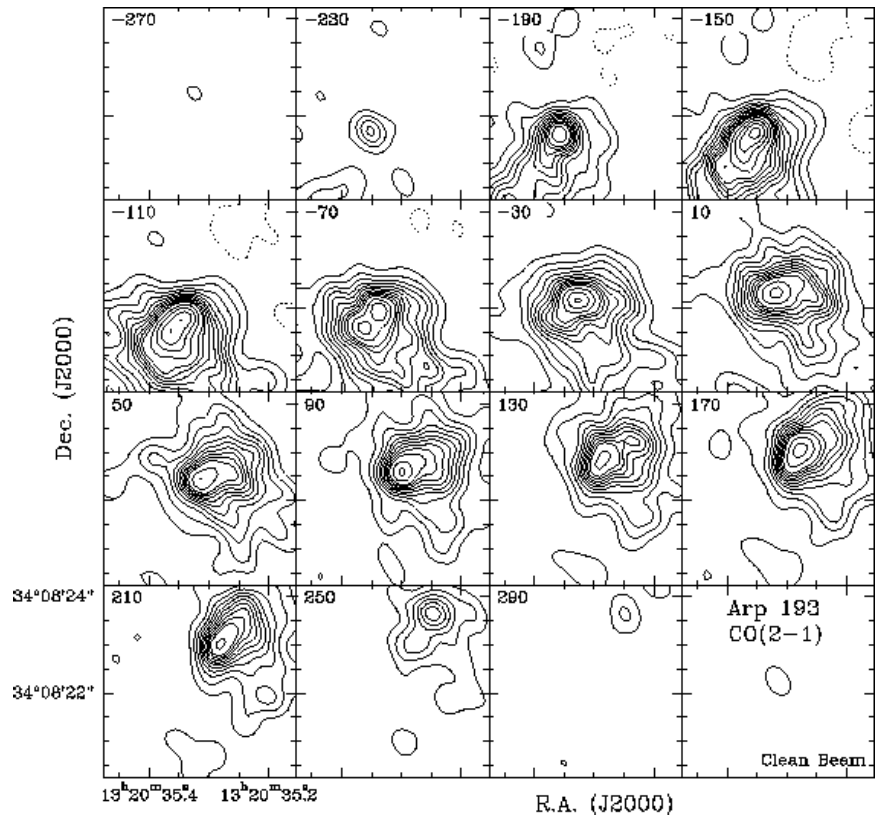
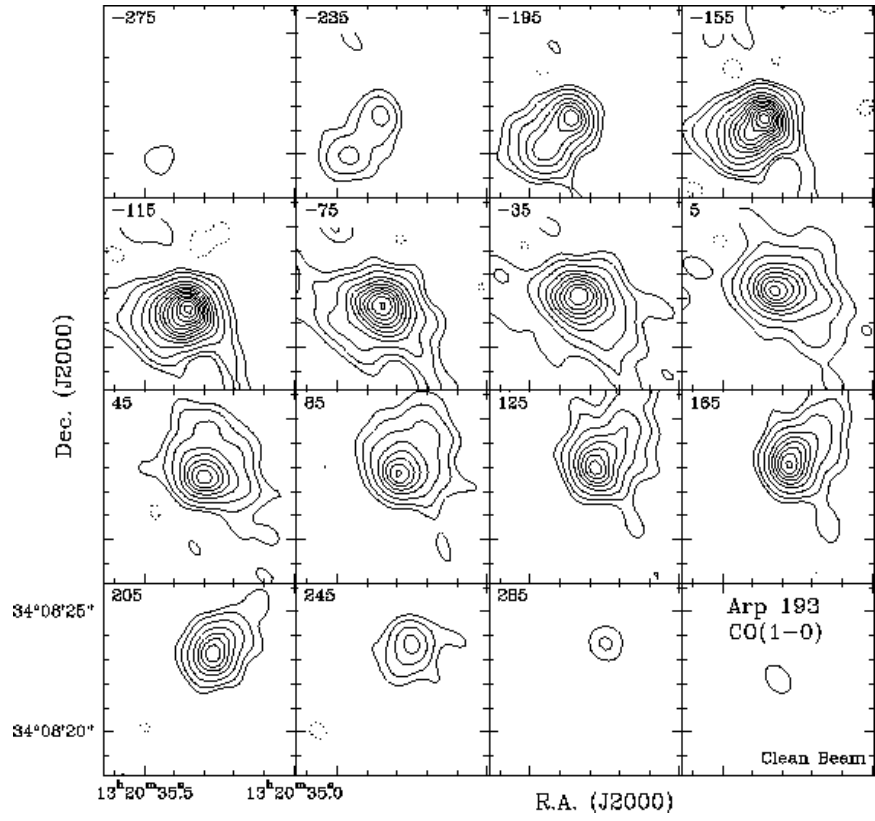


Fig. 9.— **Arp 193** :

— *upper*: CO(1–0) maps in  $40 \text{ km s}^{-1}$  channels. Radial velocities ( $\text{km s}^{-1}$ , upper left of each box) are relative to  $112.641 \text{ GHz}$  ( $cz_{\text{lsr}} = 7000 \text{ km s}^{-1}$ ). Contour unit:  $-5, 5, 10$ , then  $20$  to  $170$  by  $15 \text{ mJy beam}^{-1}$ . Beam =  $1''.3 \times 0''.9$  with  $T_b/S = 83 \text{ K/Jy}$ .

— *lower*: CO(2–1) maps in  $40 \text{ km s}^{-1}$  channels. Radial velocities ( $\text{km s}^{-1}$ , upper left of each box) are relative to  $225.282 \text{ GHz}$  ( $cz_{\text{lsr}} = 6994 \text{ km s}^{-1}$ ). Contour interval  $-10, 10$  to  $100$  in steps of  $10$ , then  $10$  to  $180$  in steps of  $20 \text{ mJy beam}^{-1}$ . Beam =  $0''.6 \times 0''.4$  with  $T_b/S = 84 \text{ K/Jy}$ .

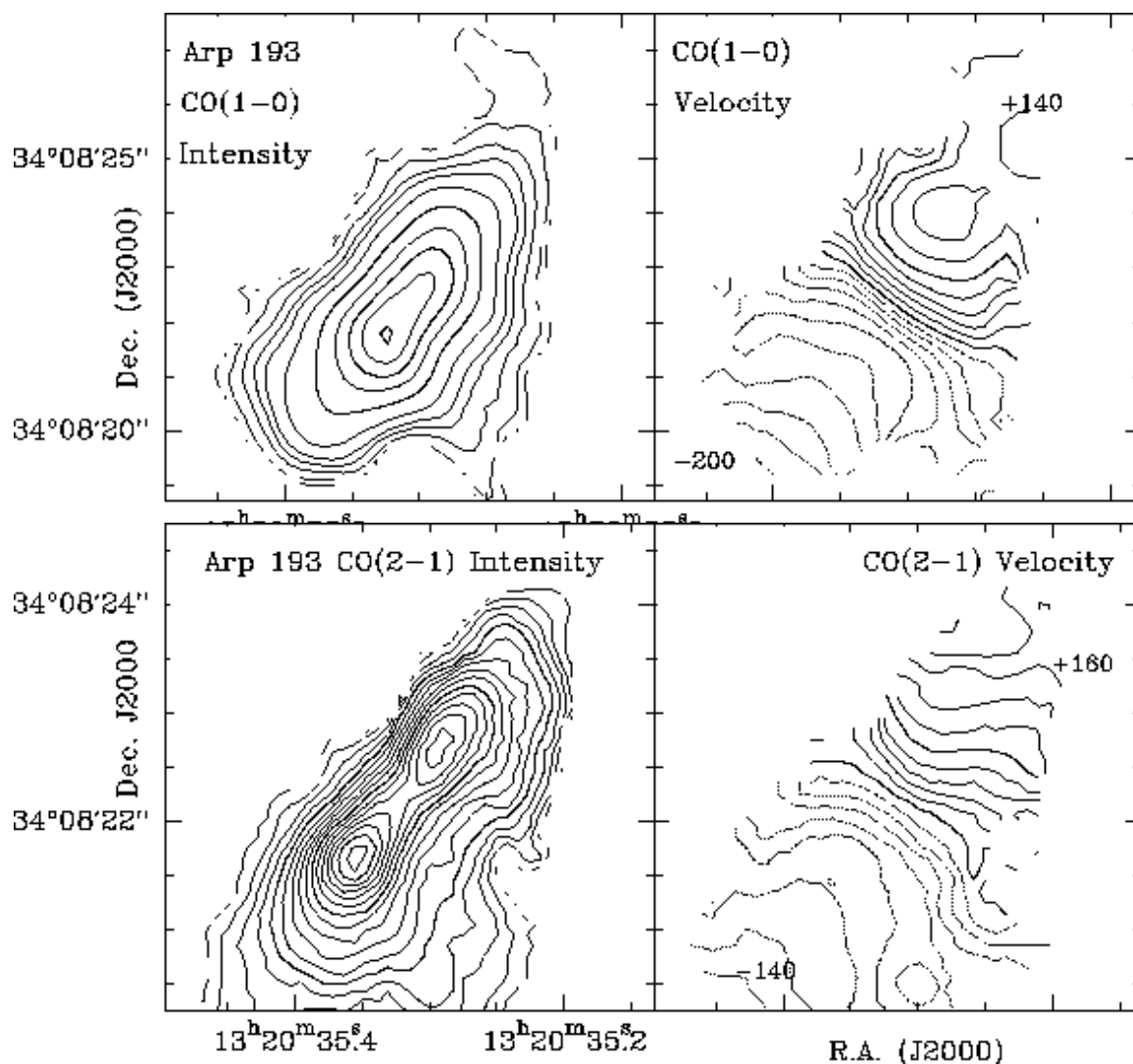


Fig. 10.— **Arp 193** : *Upper left*: CO(1-0) integrated from  $-245$  to  $+270$   $\text{km s}^{-1}$ . Beam =  $1''.3 \times 0''.9$ . Contours: 0.5, 1, 2, 3, 4, 6, then 10 to 45 by  $5 \text{ Jy beam}^{-1} \text{ km s}^{-1}$ , with  $T_b/S = 83 \text{ K/Jy}$ . *Upper right*: Velocity contours in steps of  $20 \text{ km s}^{-1}$  relative to  $112.641 \text{ GHz}$  ( $cz_{\text{lsr}} = 7000 \text{ km s}^{-1}$ ). Labels are in  $\text{km s}^{-1}$ . *Lower left*: CO(2-1) integrated from  $-210$  to  $+270 \text{ km s}^{-1}$ . Beam =  $0''.6 \times 0''.4$ . Contour step  $2 \text{ Jy beam}^{-1} \text{ km s}^{-1}$ , with  $T_b/S = 84 \text{ K/Jy}$ . *Lower right*: Velocity contours in steps of  $20 \text{ km s}^{-1}$  relative to  $225.282 \text{ GHz}$  ( $cz_{\text{lsr}} = 6994 \text{ km s}^{-1}$ ). Labels are in  $\text{km s}^{-1}$ ;



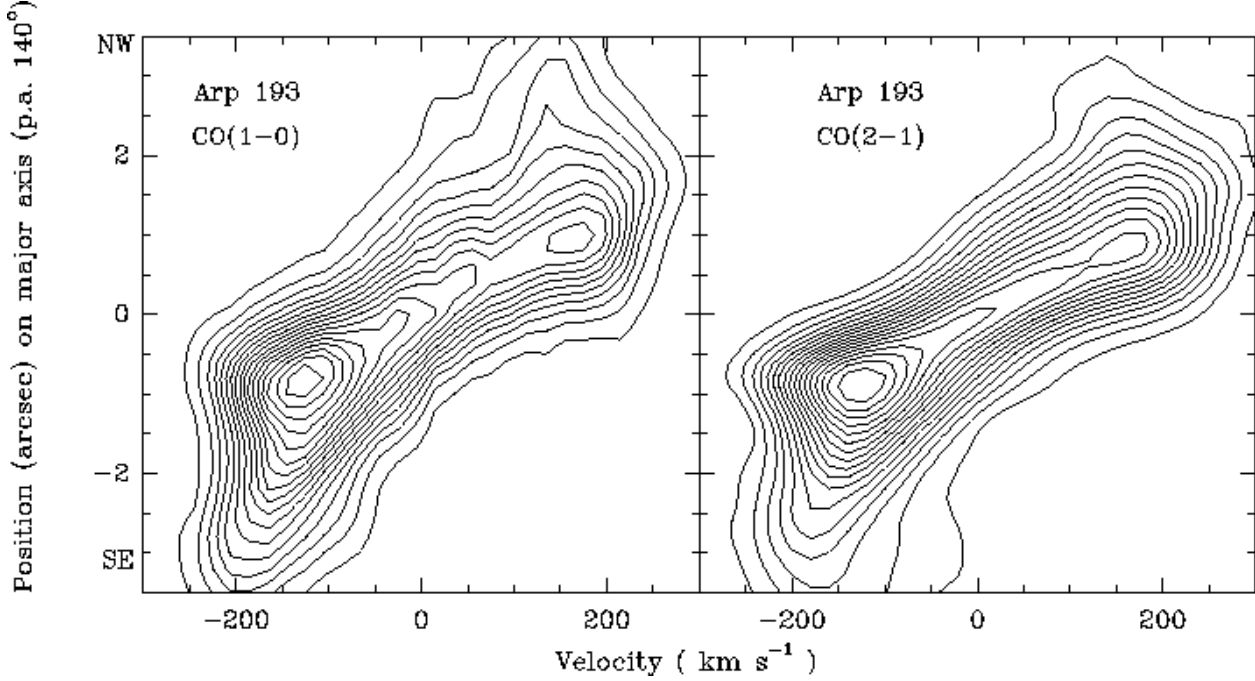


Fig. 11.— **Arp 193** : CO position-velocity diagrams along the line of nodes (p.a.  $140^\circ$ ), *left*: CO(1-0), contour unit  $10 \text{ mJy beam}^{-1}$ , with  $T_b/S = 83 \text{ K/Jy}$ . Beam =  $1''.3 \times 0''.9$ . Velocity is relative to relative to  $112.641 \text{ GHz}$  ( $cz_{\text{lsr}} = 7000 \text{ km s}^{-1}$ ). *right*: CO(2-1), contour unit  $10 \text{ mJy beam}^{-1}$ , with  $T_b/S = 84 \text{ K/Jy}$ . Beam =  $0''.6 \times 0''.4$ . Velocity is relative to relative to  $225.282 \text{ GHz}$  ( $cz_{\text{lsr}} = 6994 \text{ km s}^{-1}$ ). The (0,0) position in both diagrams is  $13^{\text{h}}20^{\text{m}}35.^{\text{s}}315, 34^\circ08'22.''20$  (J2000).

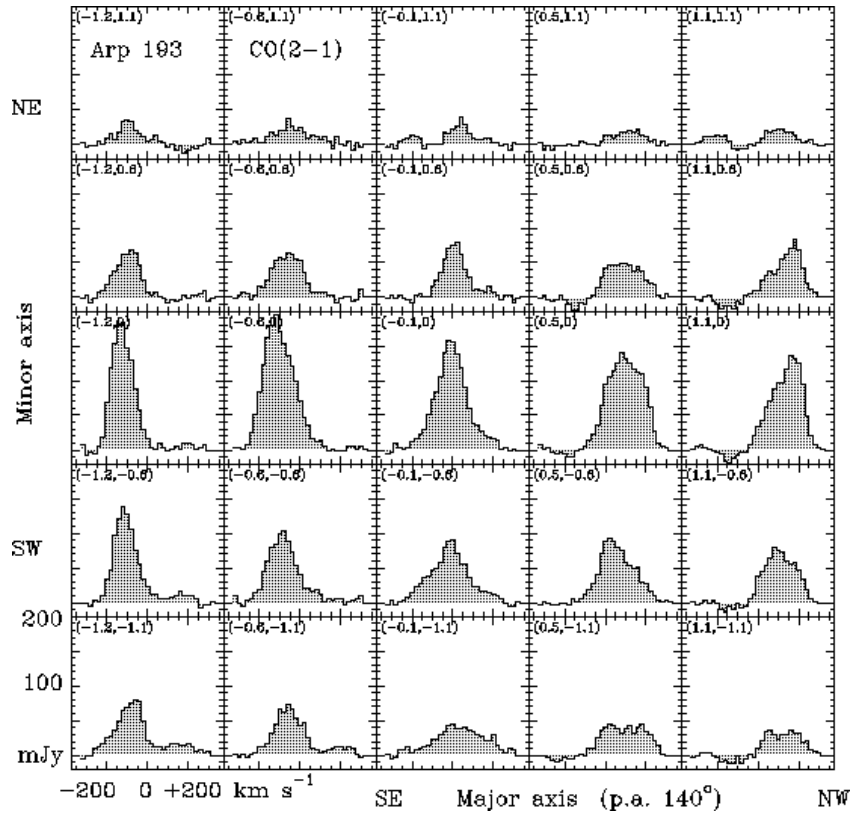
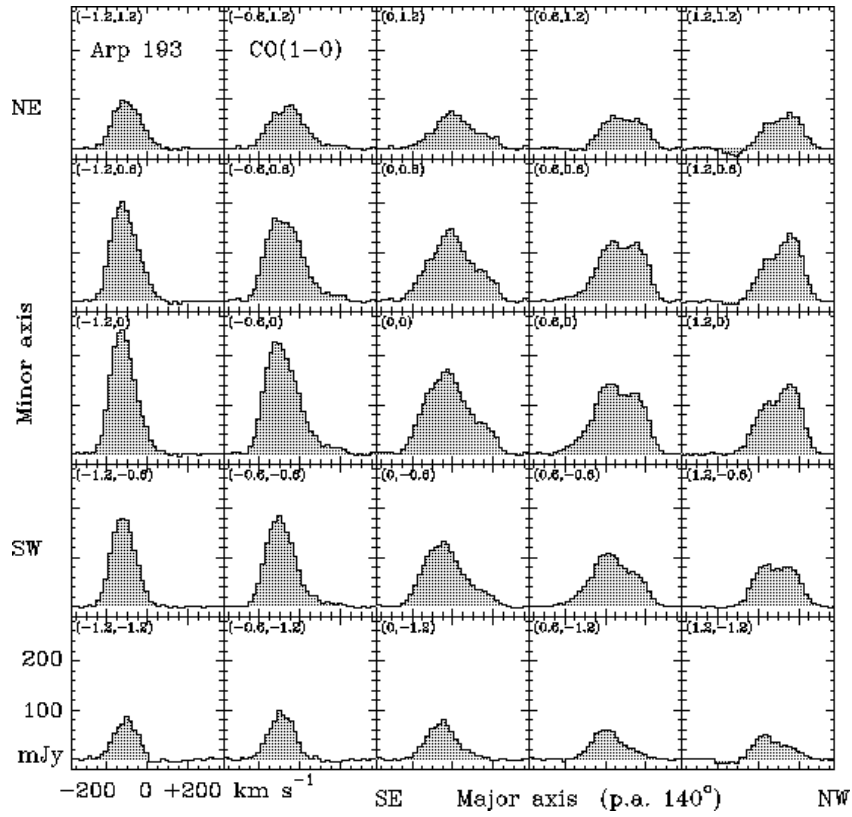


Fig. 12.— **Arp 193** : *upper*: CO(1–0) spectra. In each box vertical axis is CO intensity and horizontal axis is radial velocity relative to 112.641 GHz ( $cz_{\text{lsr}} = 7000 \text{ km s}^{-1}$ ). In the upper left of each box are offsets (arcsec) on the kinematic major and minor axes. Beam smoothed to  $1''.7 \times 1''.6$ .  
*lower*: CO(2–1) spectra. Beam =  $0''.6 \times 0''.4$ . Velocity is relative to relative to 225.282 GHz ( $cz_{\text{lsr}} = 6994 \text{ km s}^{-1}$ ). The (0,0) position in both diagrams is  $13^{\text{h}}20^{\text{m}}35.^{\text{s}}315$ ,  $34^{\circ}08'22.''20$  (J2000).

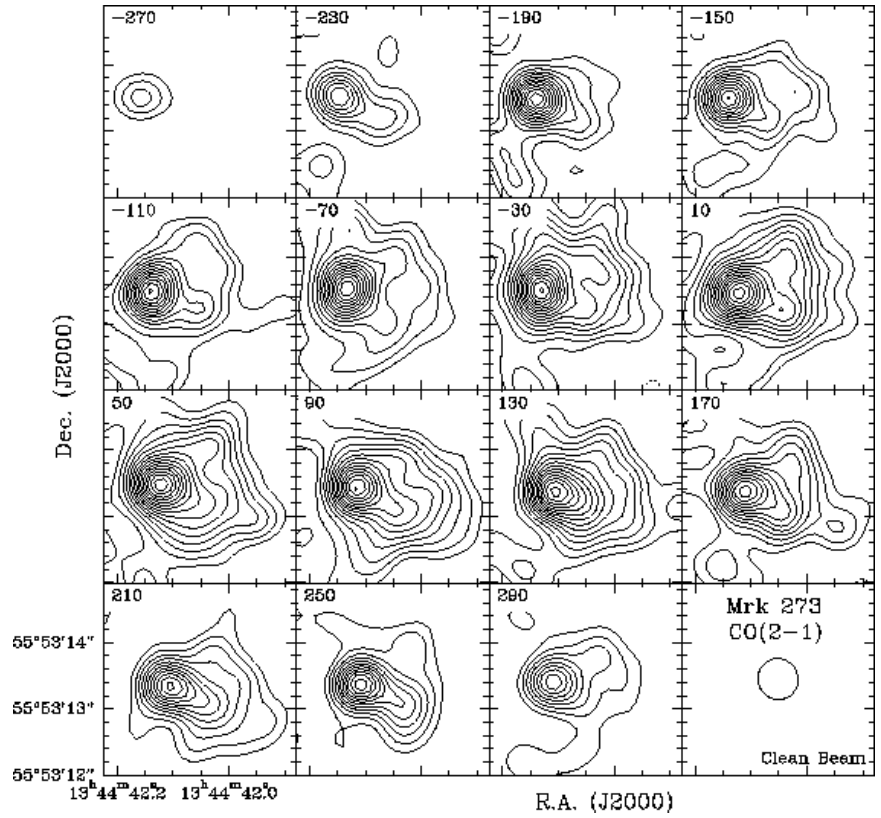
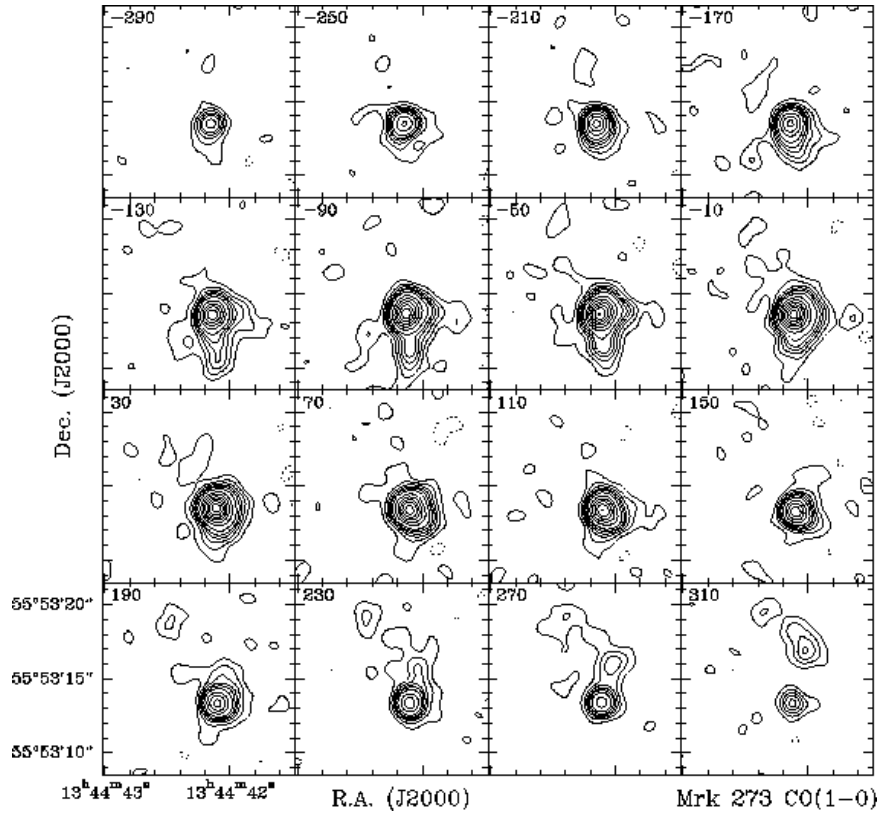


Fig. 13.— **Mrk 273** :

*a)* CO(1–0) maps in  $40 \text{ km s}^{-1}$  channels. Radial velocities ( $\text{km s}^{-1}$ , upper left of each box) are relative to  $111.076 \text{ GHz}$  ( $cz_{\text{lsr}} = 11323 \text{ km s}^{-1}$ ). Contour unit:  $-3, +3$  to  $15$  by  $5$ , then  $20$  to  $80$  by  $10 \text{ mJy beam}^{-1}$ , negative contours are dashed, zero contour omitted. Beam =  $1''.4 \times 1''.3$  with  $T_b/S = 56 \text{ K/Jy}$ .

*b)* CO(2–1) maps in  $40 \text{ km s}^{-1}$  channels. Radial velocities ( $\text{km s}^{-1}$ , upper left of each box) are relative to  $222.176 \text{ GHz}$  ( $cz_{\text{lsr}} = 11283 \text{ km s}^{-1}$ ). Contour interval  $10$  to  $85$ , in steps of  $5 \text{ mJy beam}^{-1}$ . Beam =  $0''.6$  with  $T_b/S = 66 \text{ K/Jy}$ .

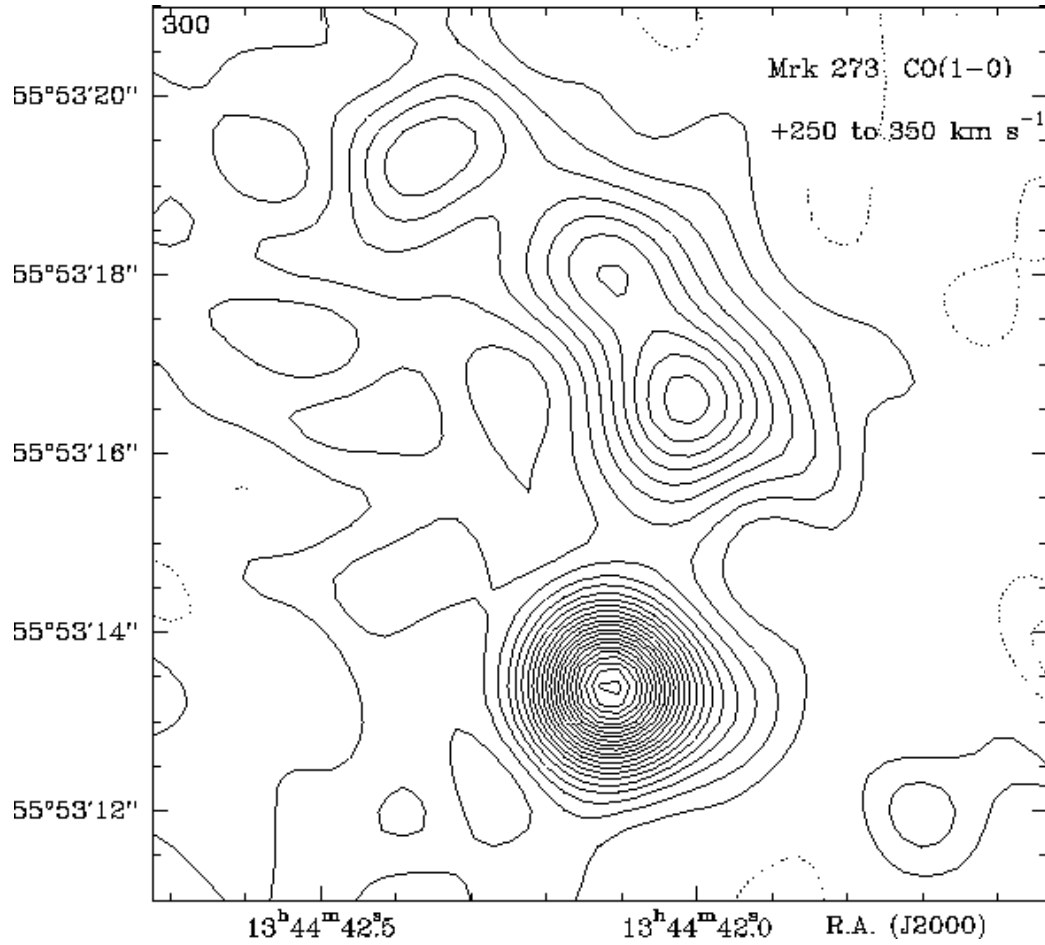


Fig. 14.— **Mrk 273** : CO(1-0), integrated over 250 to 350 km s<sup>-1</sup>, relative to 111.076 GHz ( $cz_{\text{lsr}} = 11323 \text{ km s}^{-1}$ ). Beam =  $1''.4 \times 1''.3$  with  $T_b/S = 56 \text{ K/Jy}$ . Contour step 1 mJy beam<sup>-1</sup>, negative contours are dashed, zero contour omitted.

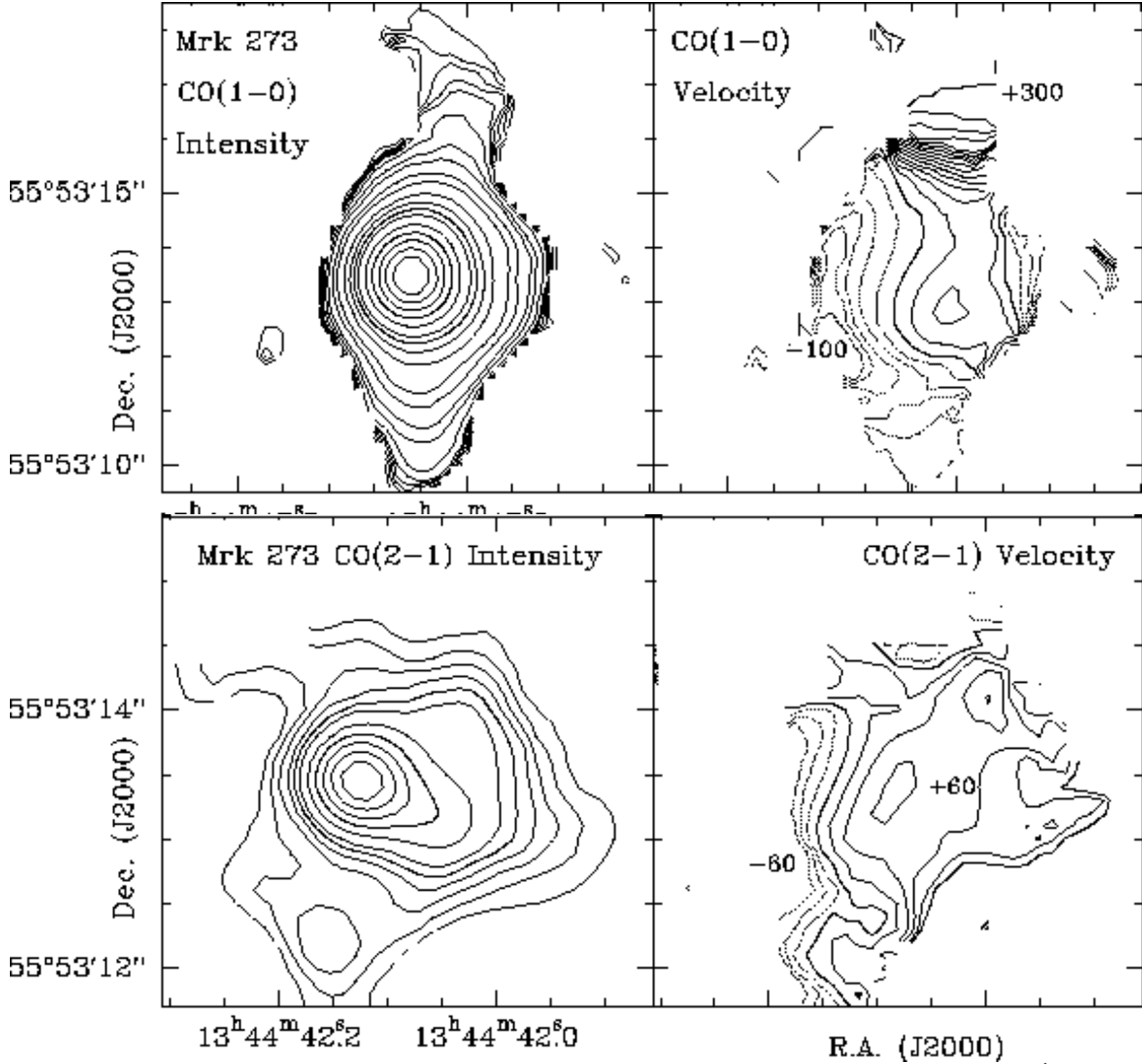


Fig. 15.— **Mrk 273** : *Upper left*: CO(1-0) integrated over  $\pm 340 \text{ km s}^{-1}$ . Beam =  $1''.4 \times 1''.3$ . Contours: 0.3 to 0.7 by 0.1, then 1, 1.5, 2, 3, 4, 6, then 8 to 36 by  $4 \text{ Jy beam}^{-1} \text{ km s}^{-1}$ , with  $T_b/S = 56 \text{ K/Jy}$ . *Upper right*: Velocity contours in steps of  $20 \text{ km s}^{-1}$  relative to  $111.076 \text{ GHz}$  ( $cz_{\text{lsr}} = 11323 \text{ km s}^{-1}$ ). Labels are in  $\text{km s}^{-1}$ ; *Lower left*: CO(2-1) integrated over  $\pm 300 \text{ km s}^{-1}$ . Beam =  $0''.6 \times 0''.6$ . Contours: 2, 4, 6, then 8 to 32 in steps of  $4 \text{ Jy beam}^{-1} \text{ km s}^{-1}$ , with  $T_b/S = 66 \text{ K/Jy}$ . *Lower right*: Velocity contours in steps of  $20 \text{ km s}^{-1}$  relative to  $222.176 \text{ GHz}$  ( $cz_{\text{lsr}} = 11283 \text{ km s}^{-1}$ ). Labels are in  $\text{km s}^{-1}$ .

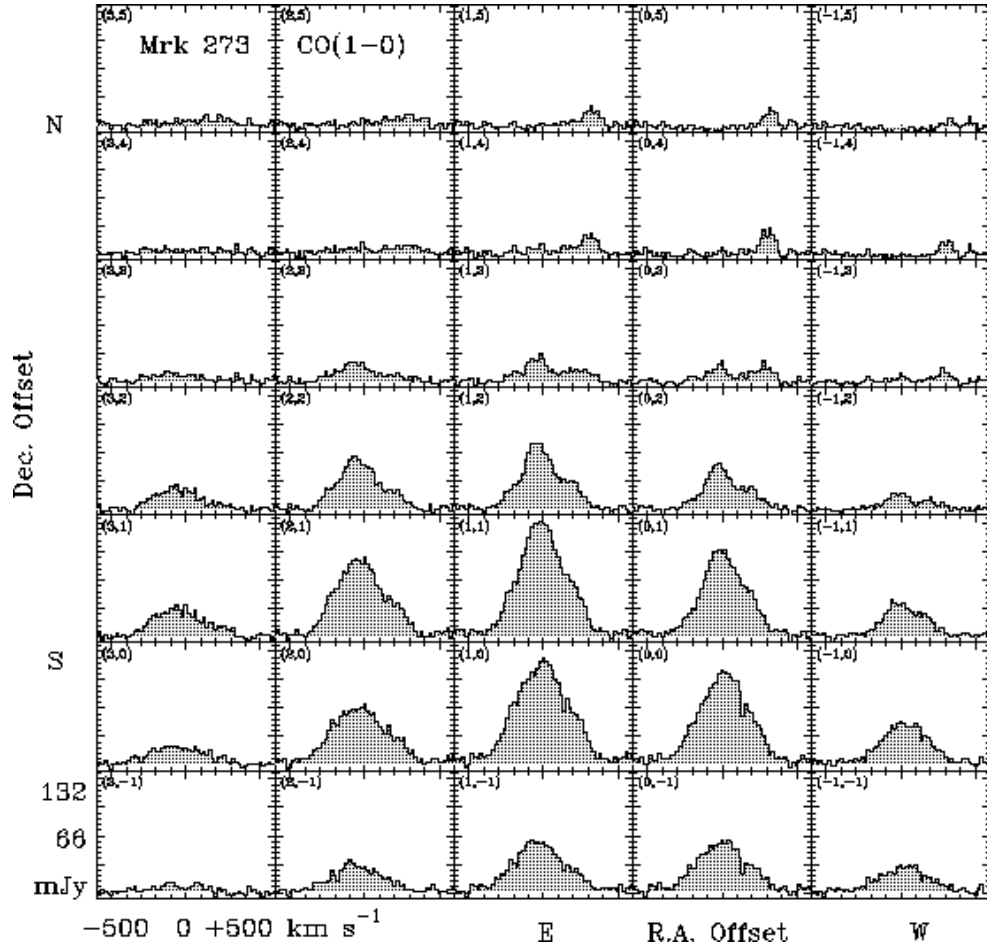


Fig. 16.— **Mrk 273** : CO(1–0) spectra. In each box vertical axis is CO intensity, horizontal axis is radial velocity relative to 111.076 GHz ( $c z_{\text{LSR}} = 11323 \text{ km s}^{-1}$ ). In the upper left of each box are R.A. and Dec. offsets (arcsec); the (0,0) position is  $13^{\text{h}}44^{\text{m}}42.^{\text{s}}01, 55^{\circ}53'13.''0$  (J2000). Beam =  $2''.9 \times 2''.1$ , with  $T_b/S = 16 \text{ K/Jy}$ .



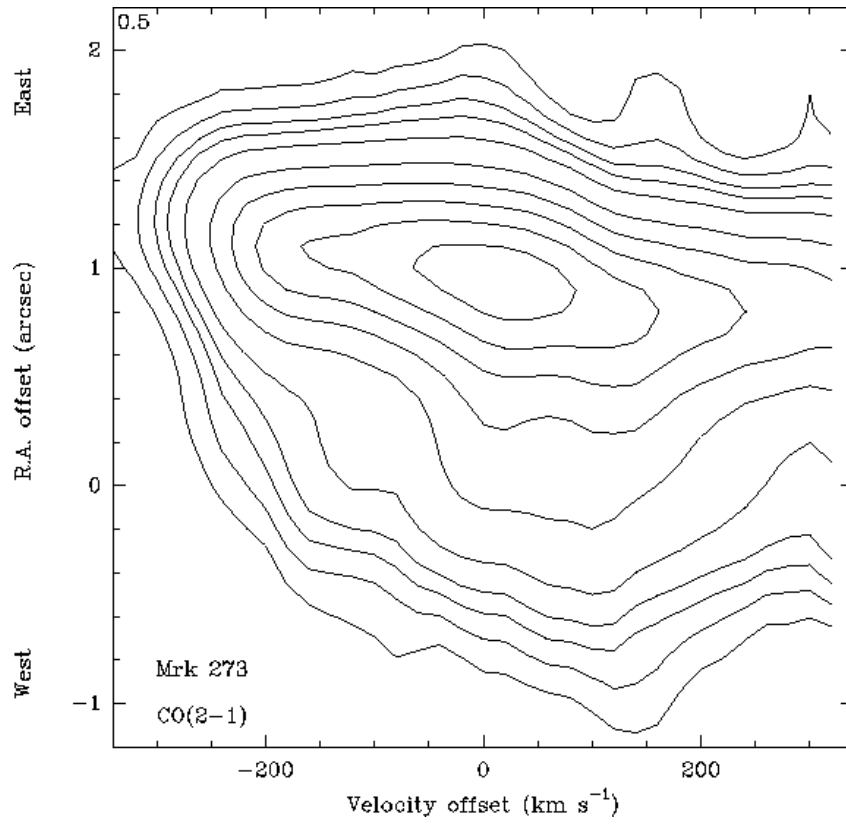
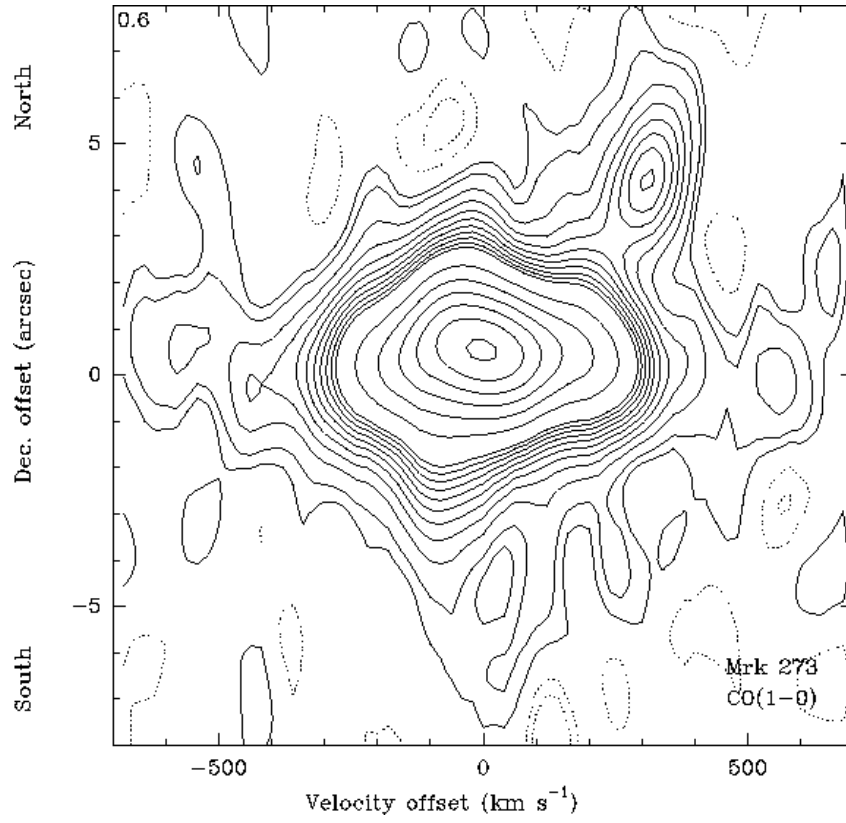


Fig. 17.— **Mrk 273** :

(a) CO(1–0) position-velocity diagram in declination, through the center of Mrk 273. Note at  $+300 \text{ km s}^{-1}$  the second CO complex  $4''$  north of the main CO peak. Contour levels:  $-2$ ,  $-1$ ,  $+1$ , then 2 to 20 by 2, and 20 to 160 by 10, in units of  $1.7 \text{ mJy beam}^{-1}$ , with  $T_b/S = 16 \text{ K/Jy}$ . Beam =  $2''.9 \times 2''.1$ . Velocity is relative to  $111.076 \text{ GHz}$  ( $c z_{\text{lsr}} = 11323 \text{ km s}^{-1}$ ). The (0,0) position is  $13^{\text{h}}44^{\text{m}}42.^{\text{s}}01$ ,  $55^{\circ}53'13.''0$  (J2000).

(b) CO(2–1) position-velocity diagram along the line of nodes of the nuclear disk (p.a.  $90^{\circ}$ , i.e., the R.A. axis). Contour levels: 3 to 15 by 3, then 20 to 70 by 10  $\text{mJy beam}^{-1}$ , with  $T_b/S = 66 \text{ K/Jy}$ . Beam =  $0''.6 \times 0''.6$ . Velocity is relative to  $222.176 \text{ GHz}$  ( $c z_{\text{lsr}} = 11283 \text{ km s}^{-1}$ ). The (0,0) position is  $13^{\text{h}}44^{\text{m}}42.^{\text{s}}01$ ,  $55^{\circ}53'13.''5$  (J2000).

Fig. 18.— **Arp 220** : *a*): CO(2–1) integrated intensity, velocity, linewidth (FWHM), and the 1.3 mm continuum. CO integration limits:  $(-320, +300 \text{ km s}^{-1})$ . Beam =  $0''.7 \times 0''.5$ .

Contours:

*integrated CO*: 1 to 10 by 1, in units of  $11.4 \text{ Jy beam}^{-1} \text{ km s}^{-1}$ , with  $T_b/S = 69 \text{ K/Jy}$ .

*CO velocity*:  $-225$  to  $+225 \text{ km s}^{-1}$ , in steps of  $25 \text{ km s}^{-1}$  relative to  $226.422 \text{ GHz}$  ( $cz_{\text{lsr}} = 5450 \text{ km s}^{-1}$ ). Labels are in  $\text{km s}^{-1}$ ;

*CO linewidth*:  $25$  to  $350 \text{ km s}^{-1}$  in steps of  $25 \text{ km s}^{-1}$ . Labels are in  $\text{km s}^{-1}$ .

*1.3 mm continuum*: 1 to 12 by 1, in units of  $5.7 \text{ mJy beam}^{-1}$ .

— *b*): CO(1–0) integrated intensity, velocity, linewidth (FWHM), and east streamer. For all maps, the beam is  $1''.6 \times 1''.1$ , with  $T_b/S = 55 \text{ K/Jy}$ , and velocities are relative to  $113.228 \text{ GHz}$  ( $cz_{\text{lsr}} = 5410 \text{ km s}^{-1}$ ). Contours:

*CO integrated from  $-320$  to  $+300 \text{ km s}^{-1}$* : 0.1, 0.25, 0.5, then 1 to 12 by 1, in units of  $11.4 \text{ Jy beam}^{-1} \text{ km s}^{-1}$ ;

*CO velocity*:  $-200$  to  $+260 \text{ km s}^{-1}$ , in steps of  $20 \text{ km s}^{-1}$ . Labels are in  $\text{km s}^{-1}$ ;

*CO linewidth*:  $25$  to  $350 \text{ km s}^{-1}$  in steps of  $25 \text{ km s}^{-1}$ . Labels are in  $\text{km s}^{-1}$ .

*CO east streamer, integrated from  $+85$  to  $+165 \text{ km s}^{-1}$* : 0.025 to 0.2 by 0.025, then 0.25, then 0.4 to 2.4 by 0.4, in units of  $11.4 \text{ Jy beam}^{-1} \text{ km s}^{-1}$ .

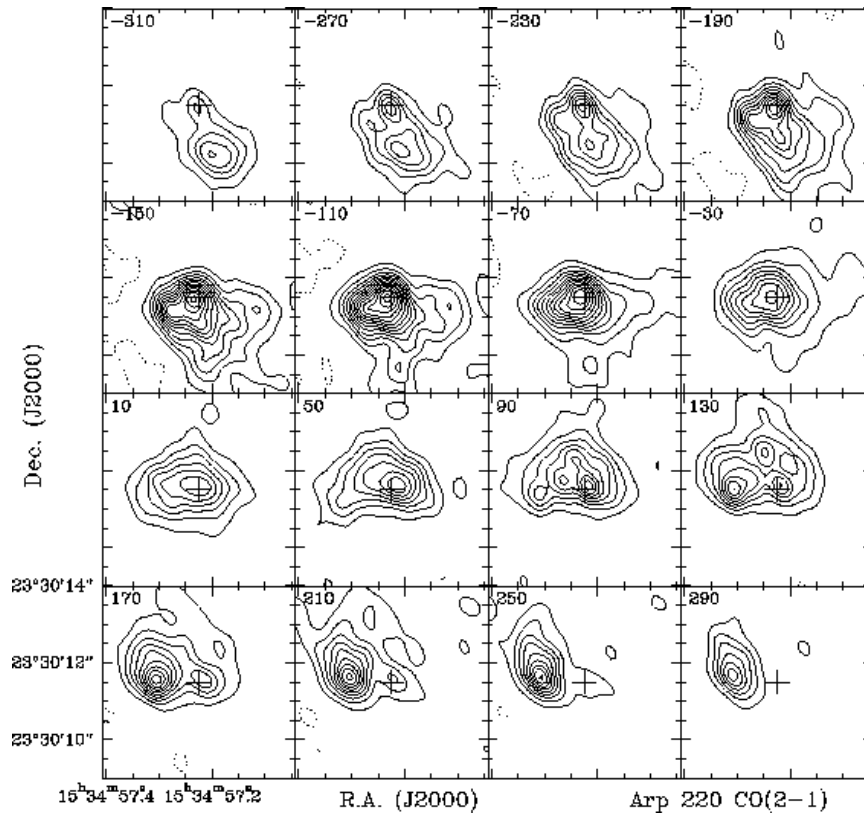
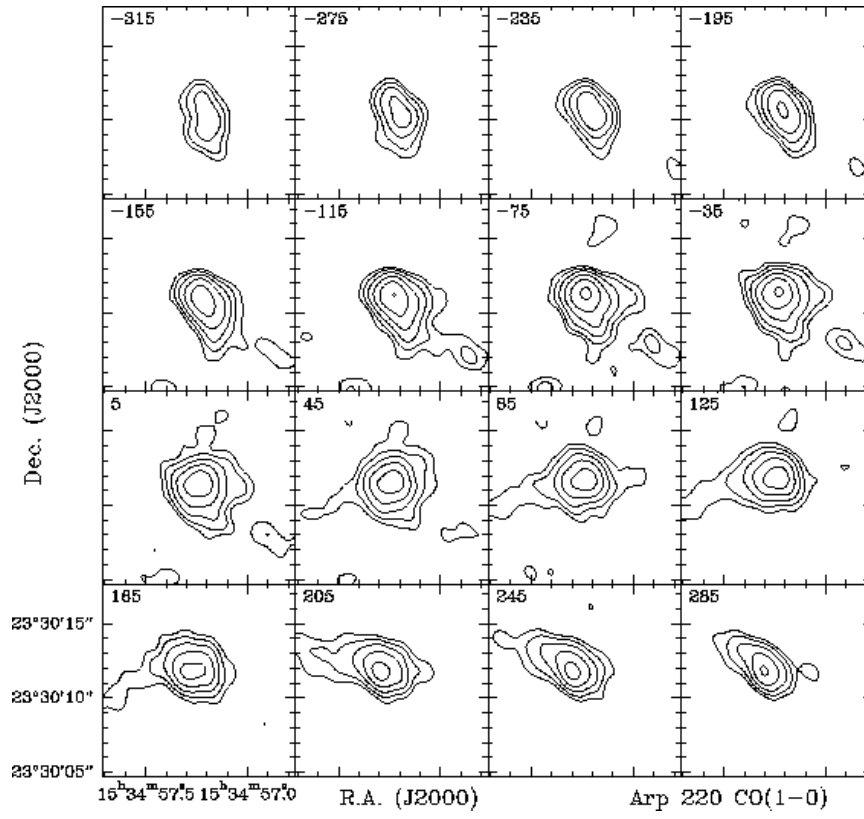


Fig. 19.— **Arp 220** : — (a) CO(1–0) maps in  $40 \text{ km s}^{-1}$  channels. Radial velocities ( $\text{km s}^{-1}$ , upper left of each box) are relative to  $113.228 \text{ GHz}$  ( $c z_{\text{lsr}} = 5410 \text{ km s}^{-1}$ ). Contours: 1, 2, 4, 8, 16, 32, in units of  $11.4 \text{ mJy beam}^{-1}$ , Beam =  $1''.6 \times 1''.1$  with  $T_b/S = 55 \text{ K/Jy}$ .  
— (b) CO(2–1) maps in  $40 \text{ km s}^{-1}$  channels. Radial velocities ( $\text{km s}^{-1}$ , upper left of each box) are relative to  $226.422 \text{ GHz}$  ( $c z_{\text{lsr}} = 5450 \text{ km s}^{-1}$ ). The cross marks the position of the integrated CO(2–1) west peak (Table 2). Beam =  $0''.7 \times 0''.5$  with  $T_b/S = 69 \text{ K/Jy}$ . The continuum has been subtracted from the CO maps. Contour unit:  $50 \text{ mJy beam}^{-1}$ . On this contour scale, the continuum from the west peak would be two contours.

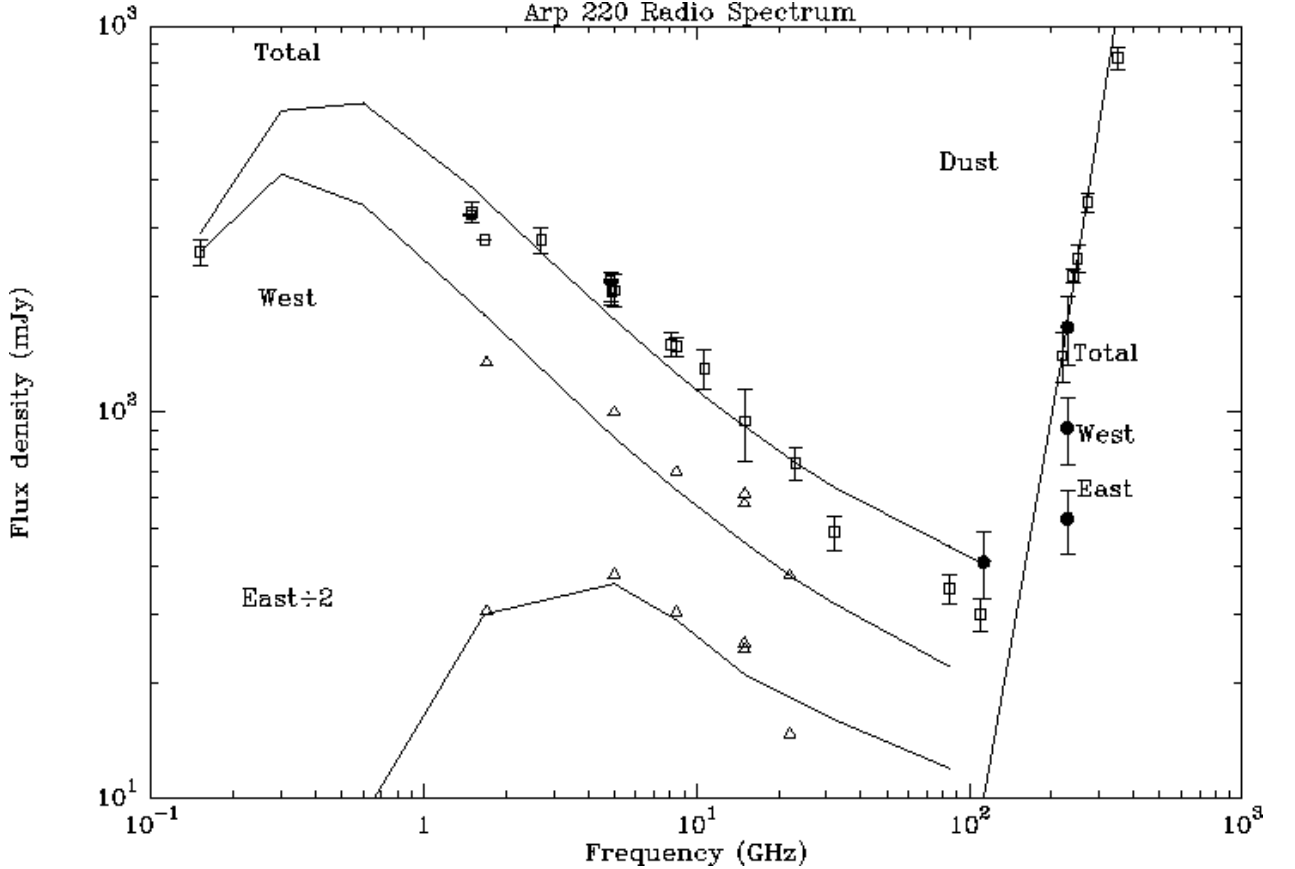


Fig. 20.— **Arp 220** : Radio continuum spectrum. The emission below 30 GHz is nonthermal (Norris et al. 1985; Becklin & Wynn-Williams 1987; Baan & Haschick 1987; Baan et al. 1987; Norris 1988; Condon et al. 1991; Sopp & Alexander 1991 and other references in their Table 3). Millimeter and sub-mm data show the increasing flux of dust emission (this paper (solid circles); Radford et al. 1991b; Scoville et al. 1991, 1997; Woody et al. 1989; Carico et al. 1992; Eales et al. 1989; and Rigopoulou et al. 1996). The curves are spectra of the form  $\nu^{2.1+\alpha}(1 + e^{-\tau})$ , normalized to the observed fluxes. The free-free opacity,  $\tau$ , has the form  $(\nu/\nu_0)^{-2.1}$ , where  $\nu_0$  is the turnover frequency. The curve for the dust spectrum is for an emissivity index  $n = 1.5$ .

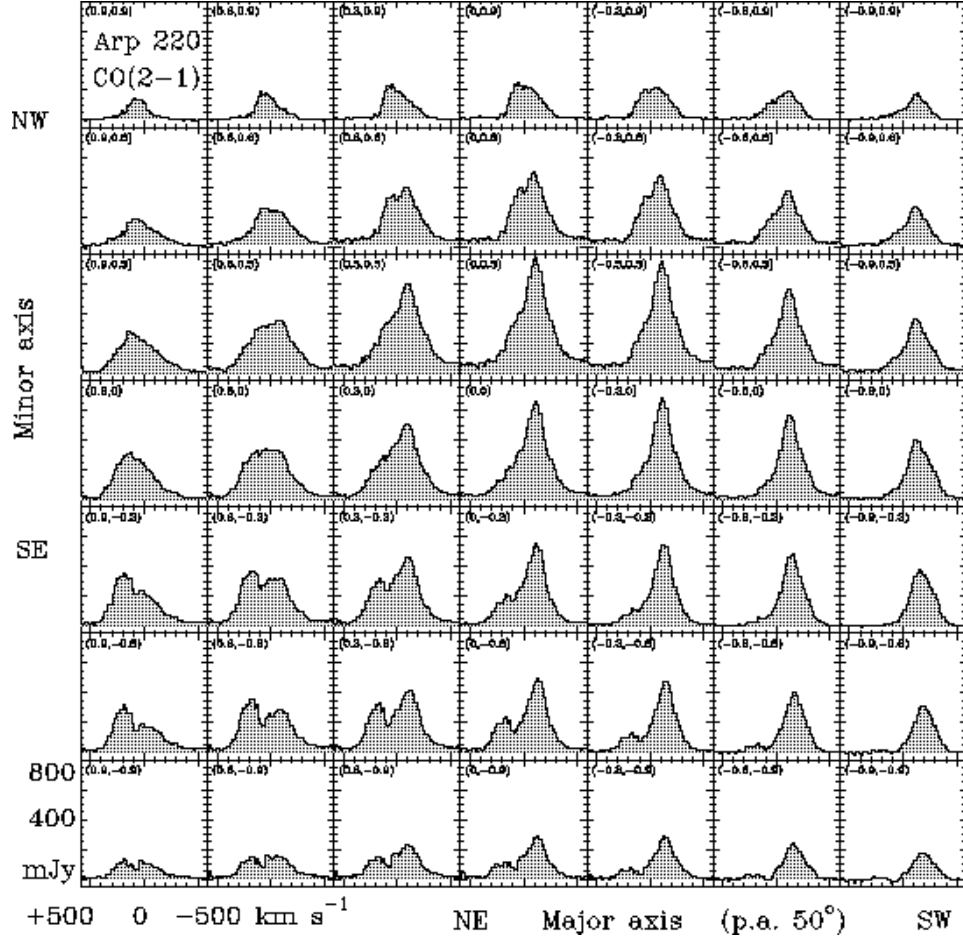
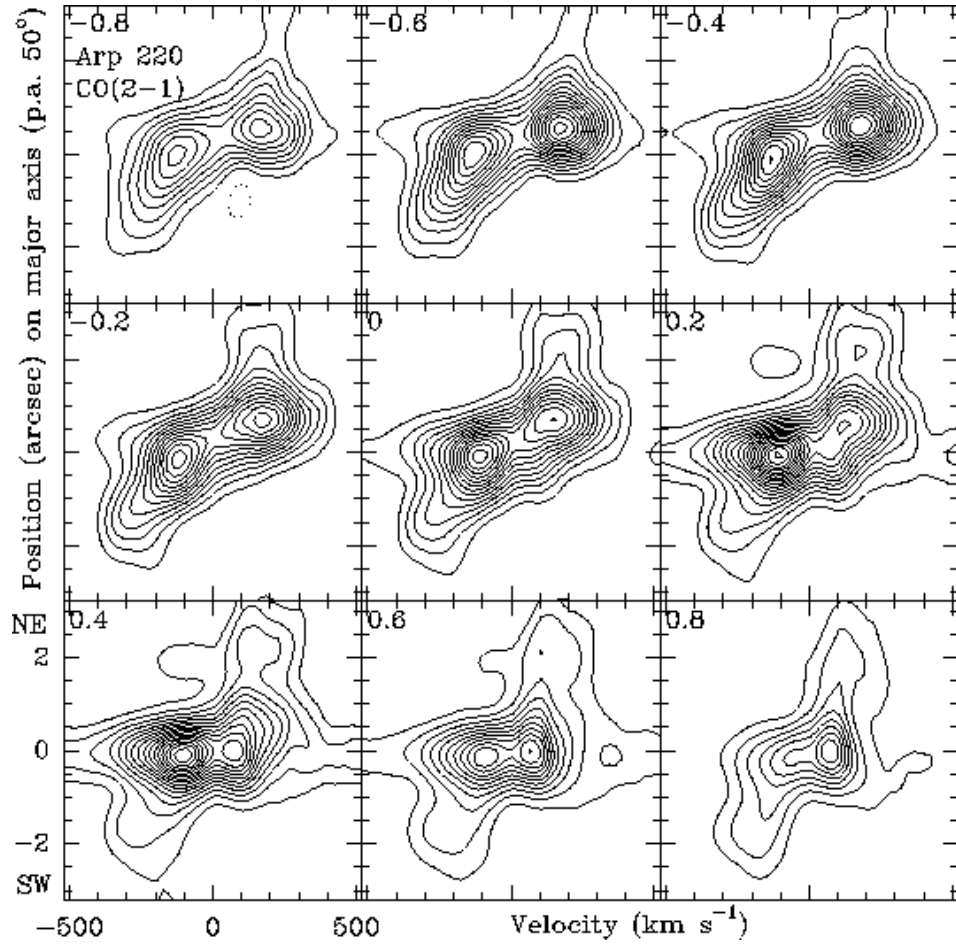
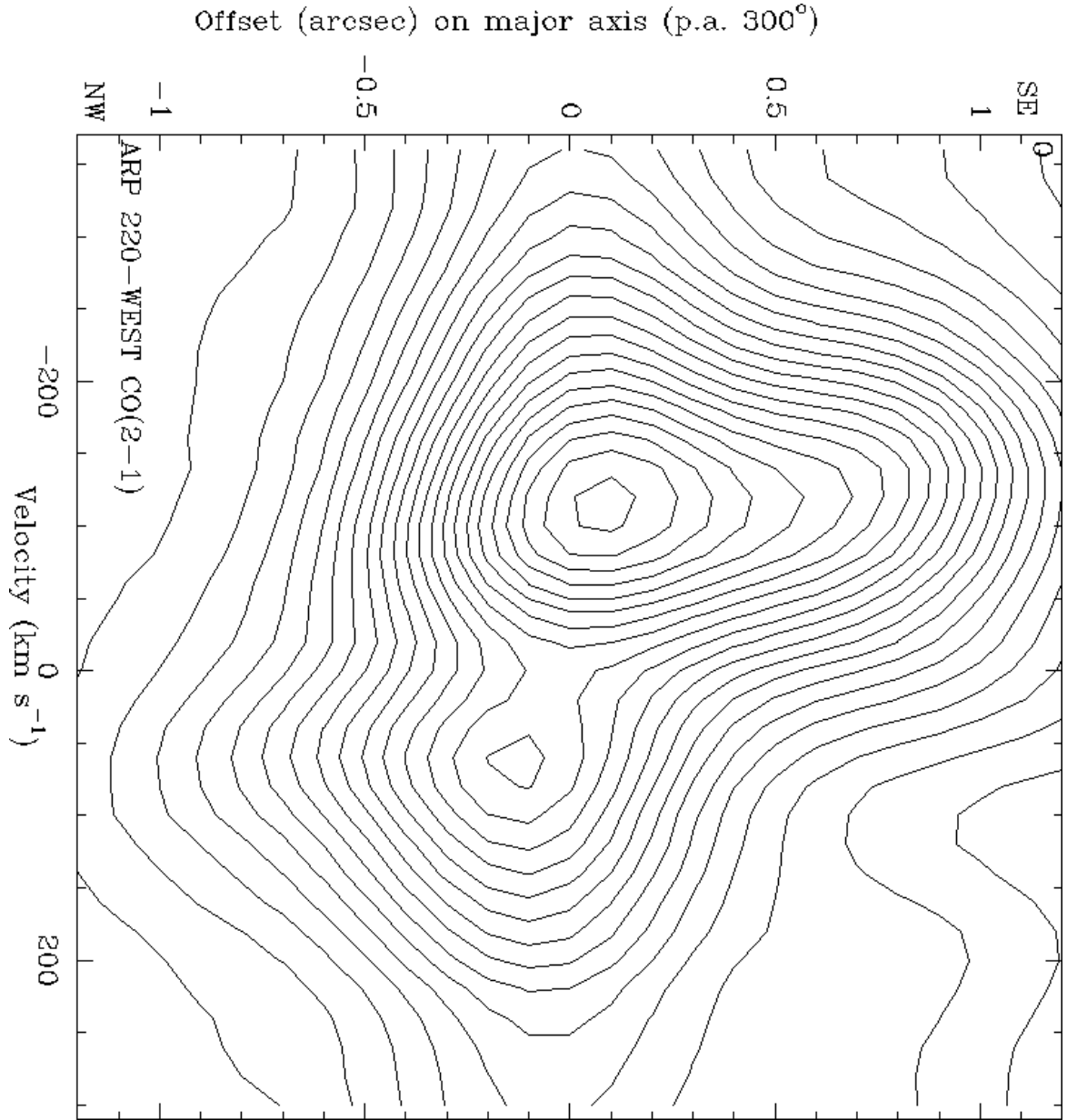


Fig. 21.— **Arp 220** : CO(2-1) spectra. In each box vertical axis is CO intensity, horizontal axis is radial velocity relative to 226.422 GHz ( $cz_{\text{lsr}} = 5450 \text{ km s}^{-1}$ ). In the upper left of each box are offsets (in steps of  $0.''3$ ) on the kinematic major and minor axes, relative to  $15^{\text{h}}34^{\text{m}}57.^{\text{s}}24$ ,  $23^{\circ}30'11.''2$  (J2000). Beam smoothed to  $= 1''.1 \times 0''.6$  at p.a.  $34^{\circ}$ , with  $T_b/S = 34 \text{ K/Jy}$ .







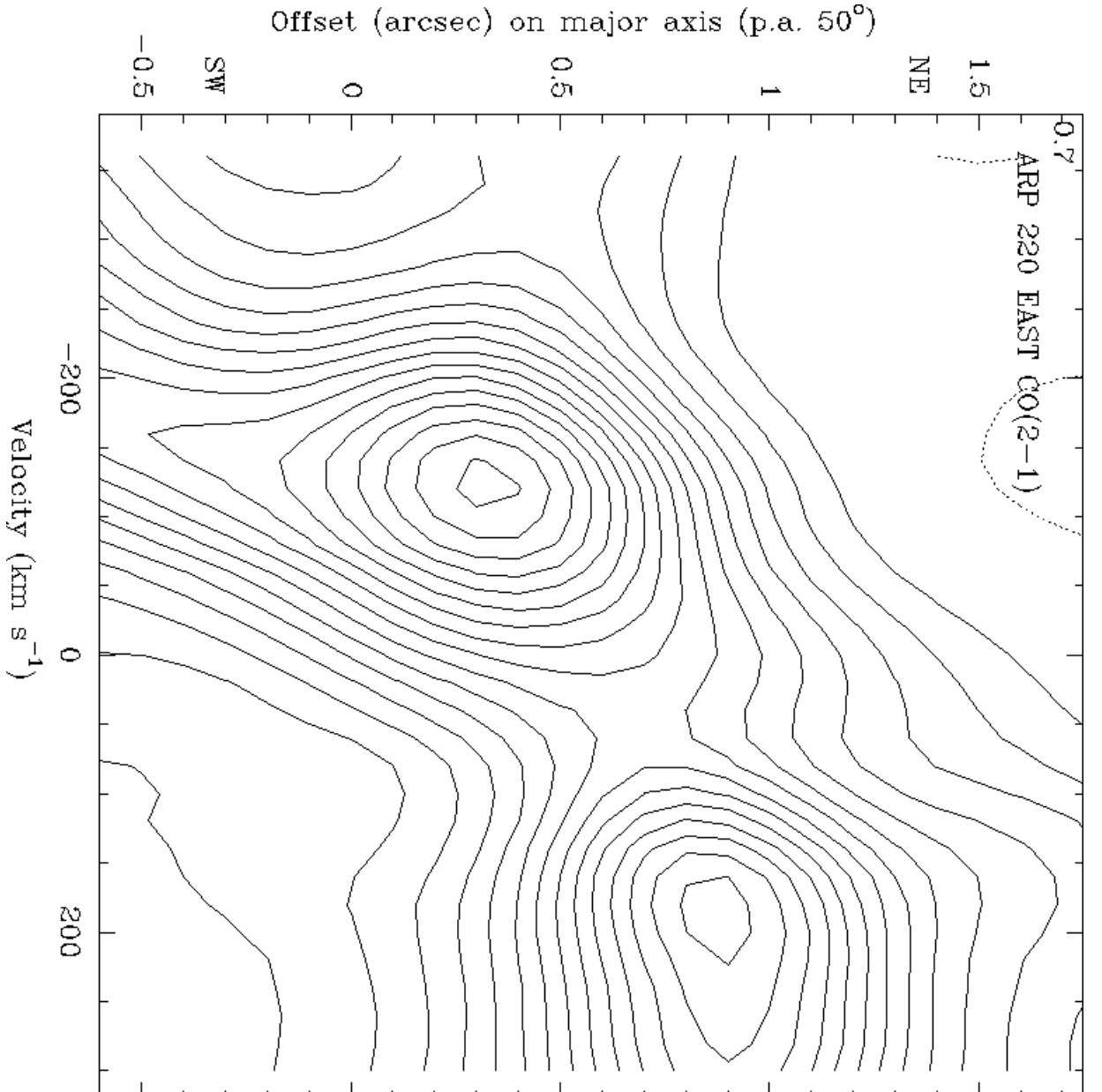


Fig. 22.— *a) Arp 220-disk* : CO(2–1) position-velocity cuts along the line of nodes (p.a.  $50^\circ$ ). Labels in the upper left of each box are offsets (arcsec) along the minor axis (northwest is positive, southeast is negative). The (0,0) position is  $15^{\text{h}}34^{\text{m}}57.^{\text{s}}24$ ,  $23^\circ30'11.''2$  (J2000). Contour levels are 1 to 17, in units of  $30 \text{ mJy beam}^{-1}$ , with  $T_b/S = 44 \text{ K/Jy}$ . Beam smoothed to  $= 1''.0 \times 0''.55$  at p.a.  $45^\circ$ .

*b) Arp 220-west*: CO(2–1) position-velocity cut through the Arp 220-west, along a possible major axis at p.a.  $300^\circ$  (see text). Contour interval  $17 \text{ mJy beam}^{-1}$ , with  $T_b/S = 80 \text{ K/Jy}$ . The source peak is  $280 \text{ mJy beam}^{-1}$ .

*c) Arp 220-east*: CO(2–1) position-velocity cut through Arp 220-east at p.a.  $50^\circ$ . Contour interval  $17 \text{ mJy beam}^{-1}$ , with  $T_b/S = 80 \text{ K/Jy}$ . The source peak is  $380 \text{ mJy beam}^{-1}$ . For diagrams *b)* and *c)*, the restoring beam was  $0''.6 \times 0''.5$  at p.a.  $120^\circ$ , and the (0,0) position is  $15^{\text{h}}34^{\text{m}}57.^{\text{s}}225$ ,  $23^\circ30'11.''5$  (J2000) (the western continuum peak). In all these position-velocity diagrams, velocity is relative to  $226.422 \text{ GHz}$  ( $cz_{\text{lsr}} = 5450 \text{ km s}^{-1}$ ).

Fig. 23.— (Plate) **Arp 220** : CO contours superposed on a false-color presentation of the HST *V* band image of Arp 220 (Shaya et al. 1994).

— *a*) CO(1–0) emission mapped with a beam of  $1''.6 \times 1''.1$ , with  $T_b/S = 55$  K/Jy, integrated in two different velocity ranges, relative to  $cz_{\text{lsr}} = 5410$  km s $^{-1}$ : — *left*: redshifted CO(1–0) emission integrated from +205 to +325 km s $^{-1}$ ; contours 0.75 to 1.75 by 0.25, 2, 2.5, 3, 4.5, 6, 9, 12, 15, 20, 25, in units of 1.14 Jy beam $^{-1}$  km s $^{-1}$ ; — *right*: blueshifted CO(1–0) emission integrated from –235 to +5 km s $^{-1}$ , with contours 0.75, 2.5, 3.5, 6, 12, 24, 36, 50, 60, 70, in units of 1.14 Jy beam $^{-1}$  km s $^{-1}$ .

*b*): CO(1–0) emission in the east streamer and CO(2–1) emission: — *left*: CO(1–0) emission in the east streamer integrated from +85 to +165 km s $^{-1}$ ; contours and beam as in Fig. 23*a*), *left*. — *right*: CO(2–1) emission integrated from –320 to +300 km s $^{-1}$ , relative to  $cz_{\text{lsr}} = 5450$  km s $^{-1}$ , with contours 20, 30 to 180 by 30, then 240, in units of 0.57 Jy beam $^{-1}$  km s $^{-1}$ ; beam =  $0''.7 \times 0''.5$ , with  $T_b/S = 69$  K/Jy.

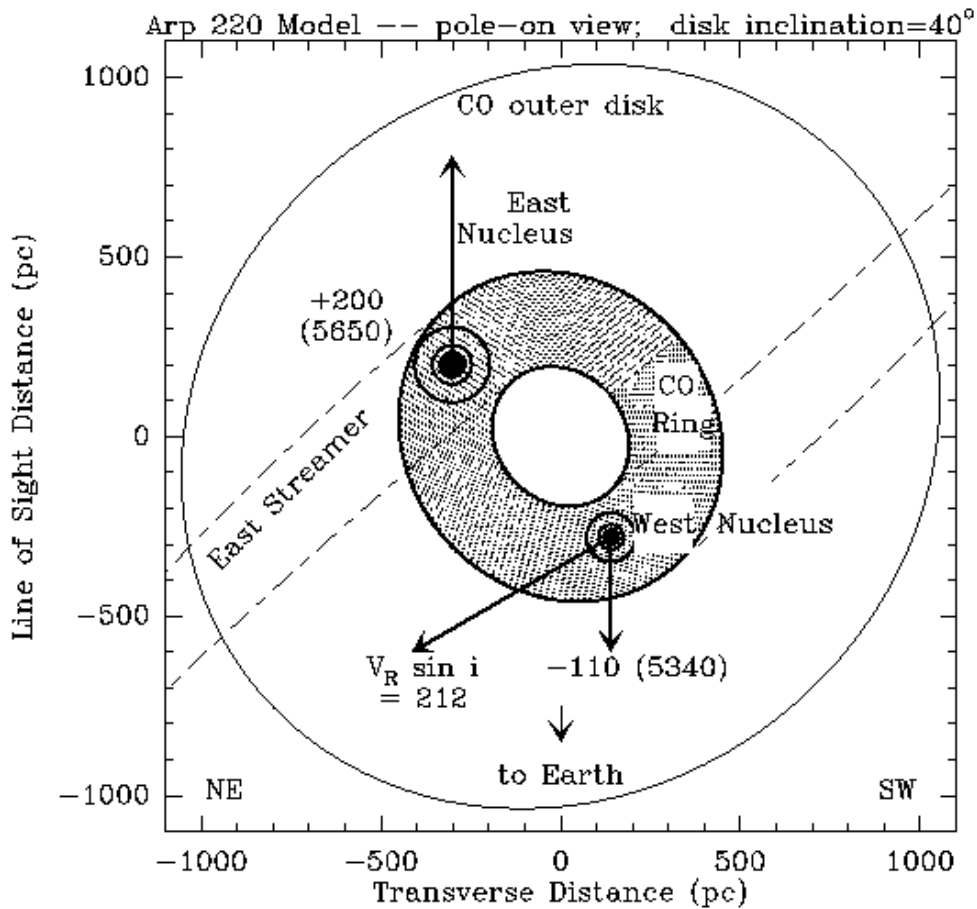


Fig. 24.— **Arp 220** : Model of the eastern and western nuclei in the molecular disk. The rotation velocity is  $330 \text{ km s}^{-1}$ , and the view is pole-on. The arrows indicate the observed radial components along the line of sight, at a disk inclination of  $40^\circ$  from face-on. Velocities are relative to a systemic velocity of  $c z_{\text{LSR}} = 5450 \text{ km s}^{-1}$ . Labels are  $\text{km s}^{-1}$ , values in parentheses are  $c z_{\text{LSR}}$ .

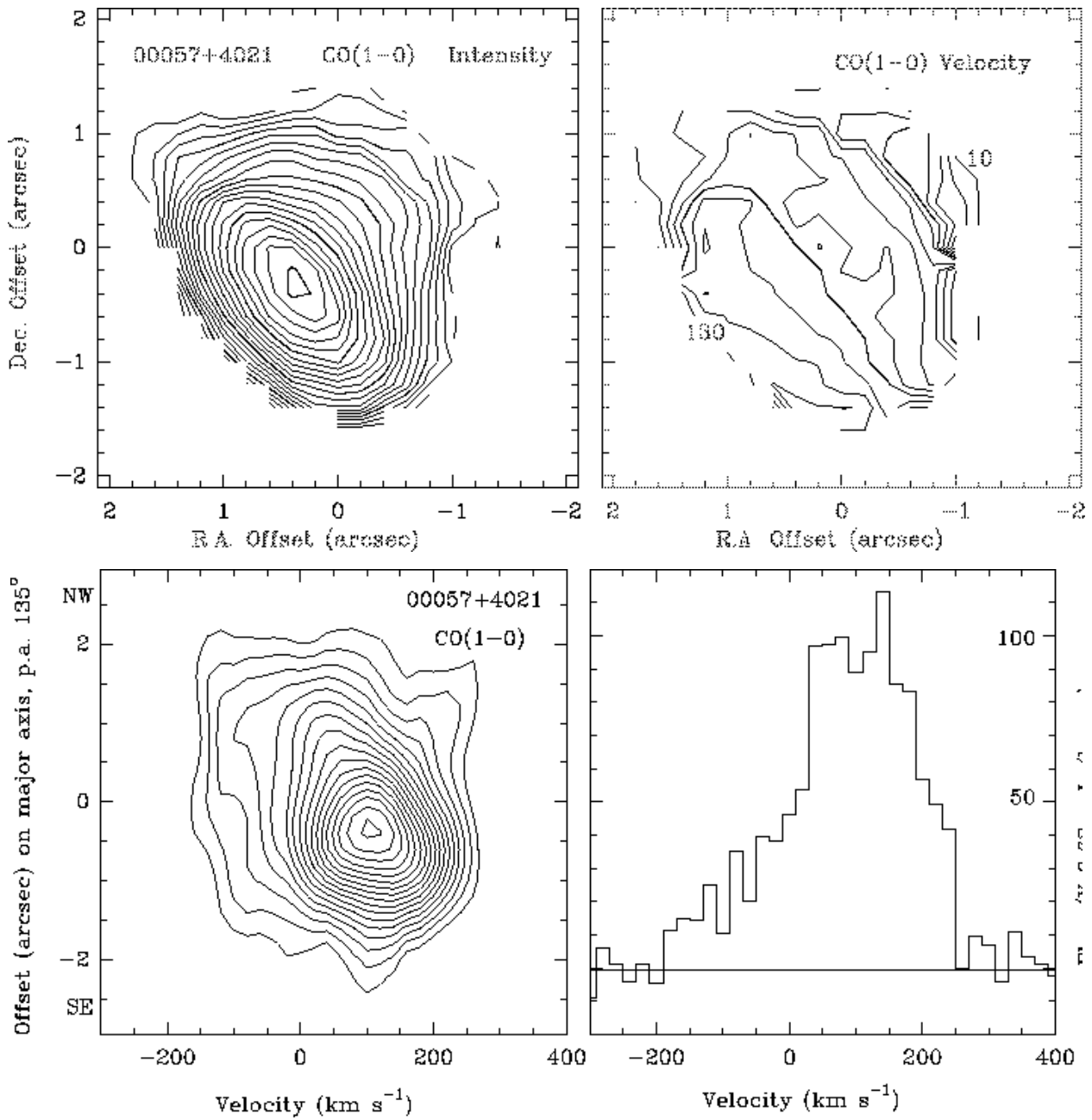


Fig. 25.— **00057+4021**: *upper left*: CO(1-0) integrated over  $(-160, +240 \text{ km s}^{-1})$ . Beam  $= 2''.2 \times 1''.1$ . Contour step  $= 0.63 \text{ Jy beam}^{-1} \text{ km s}^{-1}$ , with  $T_b/S = 40 \text{ K/Jy}$ . *upper right*: CO velocity contours in steps of  $10 \text{ km s}^{-1}$ . Labels are in  $\text{km s}^{-1}$ . *lower left*: CO(1-0) position-velocity diagram at p.a.  $135^\circ$ . Contours: 3 to 19 by 1, in units of  $3.1 \text{ mJy beam}^{-1}$ , with  $T_b/S = 40 \text{ K/Jy}$ . *lower right*: CO spectrum in the  $2''.2 \times 1''.1$  beam at the source peak. Position offsets are relative to  $00^{\text{h}}08^{\text{m}}20.^{\text{s}}58, +40^\circ37'55.''5$  (J2000), and velocity scales are relative to  $110.360 \text{ GHz}$  ( $cz_{\text{lsr}} = 13341 \text{ km s}^{-1}$ ).

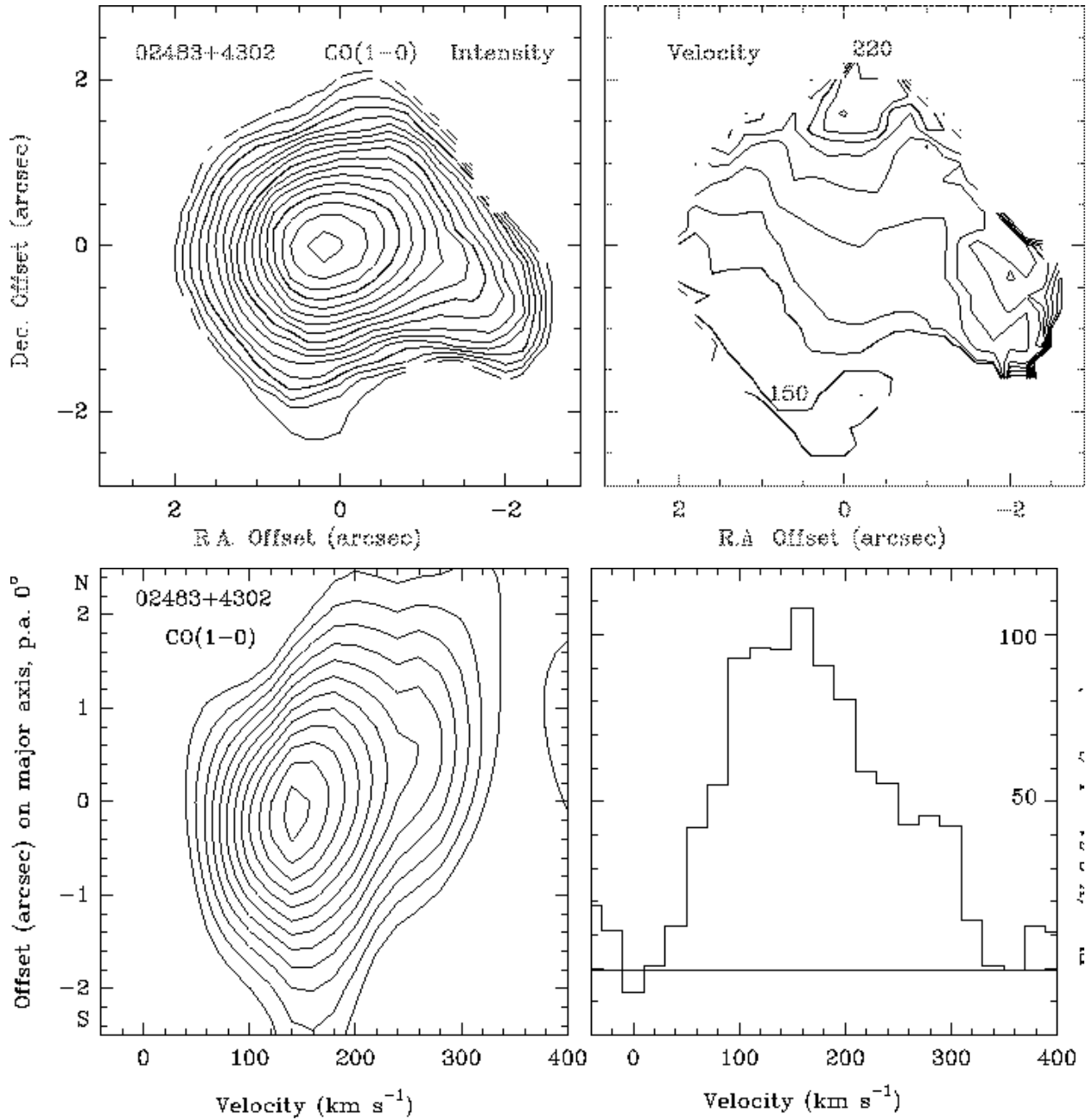


Fig. 26.— **02483+4302** : *upper left*: CO(1-0) integrated over (+40, +340 km s<sup>-1</sup>). Beam = 2".0 × 2".0. Contour step = 0.61 Jy beam<sup>-1</sup> km s<sup>-1</sup>, with  $T_b/S = 25$  K/Jy. *upper right*: CO isovelocity contours from +140 to +220 km s<sup>-1</sup>, in steps of 10 km s<sup>-1</sup>. Labels are in km s<sup>-1</sup>. *lower left*: CO(1-0) position-velocity diagram at p.a. 0°. Contours: 3 to 14 by 1, in units of 3 mJy beam<sup>-1</sup>, with  $T_b/S = 32.5$  K/Jy. Beam = 2".5 × 1".3. *lower right*: CO spectrum at the source peak, in the 2".0 × 2".0 beam, with  $T_b/S = 25$  K/Jy. Position offsets are relative to 02<sup>h</sup>51<sup>m</sup>36.<sup>s</sup>01, +43°15'10."8 (J2000), and velocity scales are relative to 109.700 GHz ( $c z_{\text{lsr}} = 15225$  km s<sup>-1</sup>).

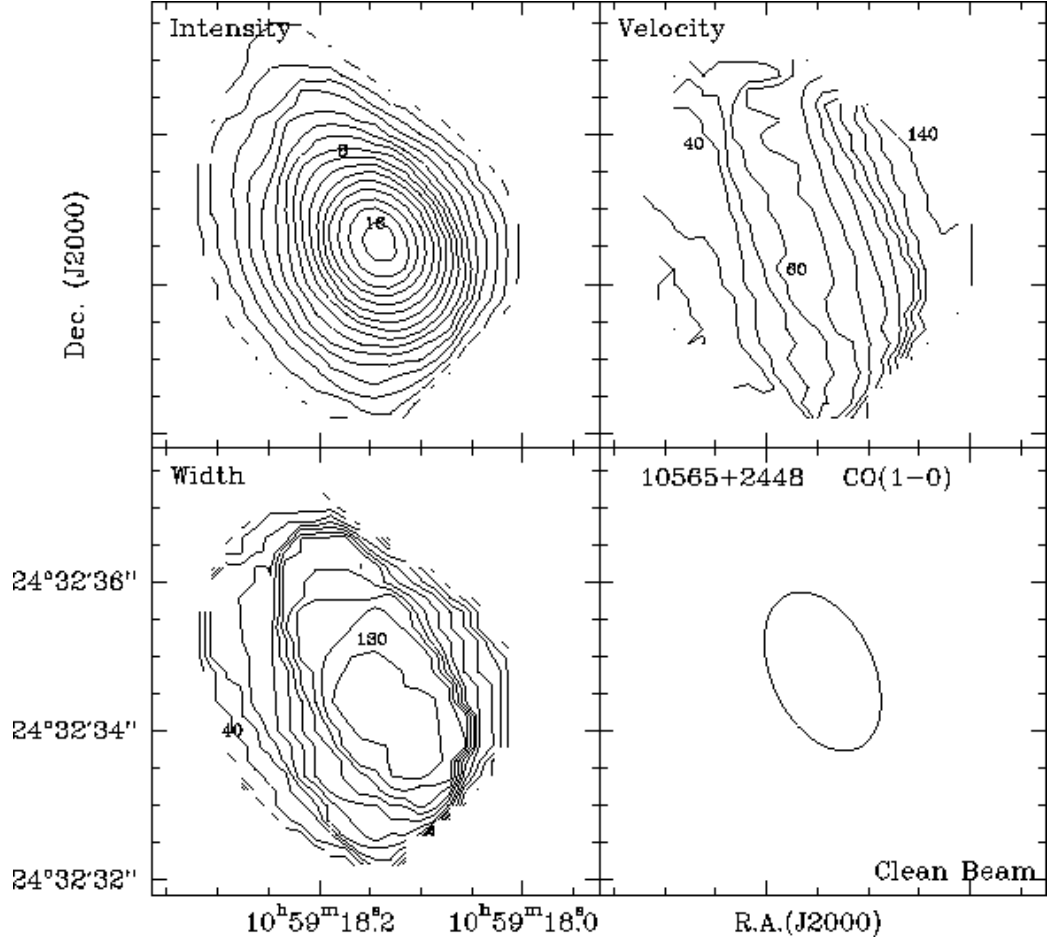


Fig. 27.— **10565+2448** : CO(1-0) integrated intensity, velocity, and linewidth (FWHM). Integration limits:  $(-100, +220 \text{ km s}^{-1})$ . Beam =  $2''.3 \times 1''.4$  (lower right). Contours: *integrated CO*: 1 to 16 by 1, in units of  $1.47 \text{ Jy beam}^{-1} \text{ km s}^{-1}$ , with  $T_b/S = 32 \text{ K/Jy}$ ; *CO velocity*:  $+20$  to  $+140 \text{ km s}^{-1}$ , in steps of  $10 \text{ km s}^{-1}$  relative to  $110.535 \text{ GHz}$  ( $c z_{\text{lsr}} = 12846 \text{ km s}^{-1}$ ). Labels are in  $\text{km s}^{-1}$ ; *CO linewidth*:  $30$  to  $130 \text{ km s}^{-1}$  in steps of  $10 \text{ km s}^{-1}$ . Labels are in  $\text{km s}^{-1}$ .



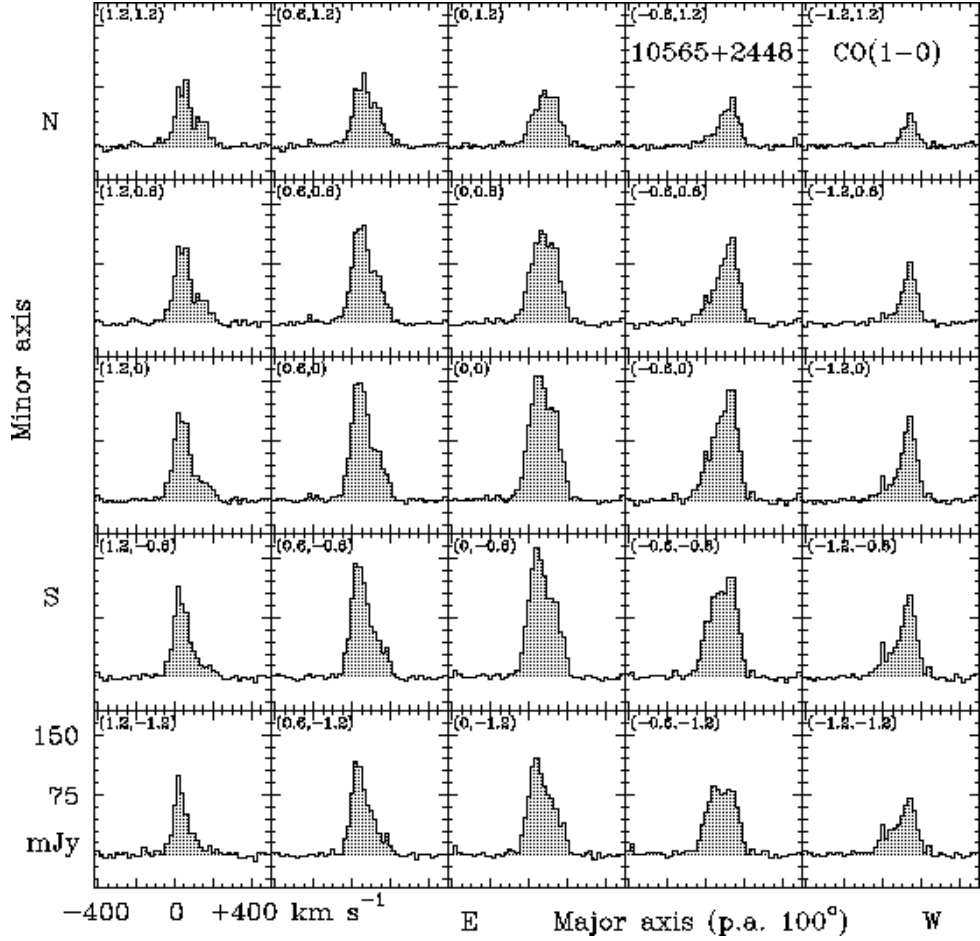


Fig. 28.— **10565+2448** : CO(1-0) spectra. In each box vertical axis is CO intensity and horizontal axis is radial velocity relative to 110.535 GHz ( $cz_{\text{lsr}} = 12846 \text{ km s}^{-1}$ ). In the upper left of each box are offsets (arcsec) on the kinematic major and minor axes, relative to the CO centroid listed in Table 2. Beam =  $2''.3 \times 1''.4$ , with  $T_b/S = 32 \text{ K/Jy}$ .

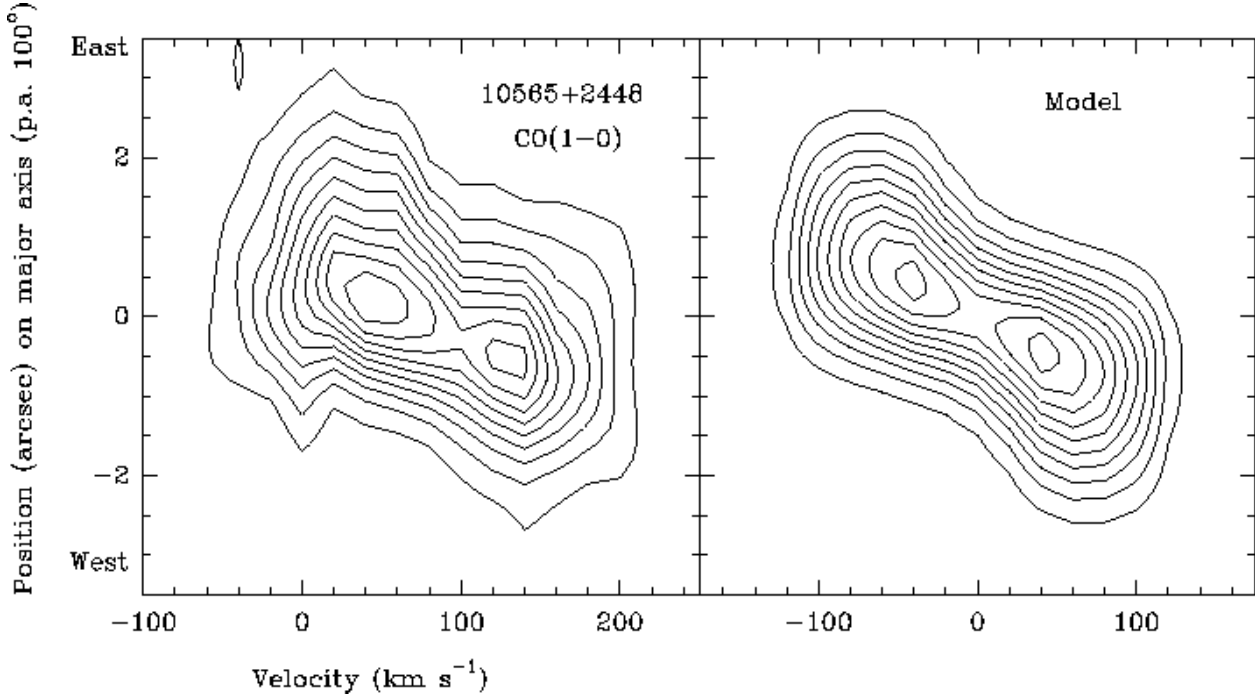


Fig. 29.— **10565+2448** : CO(1–0) position-velocity diagrams along the line of nodes (p.a.  $100^\circ$ ). *left*: — Observed data: Contour levels are 1 to 10, in units of  $15 \text{ mJy beam}^{-1}$ , with  $T_b/S = 32 \text{ K/Jy}$ . Beam =  $2''.3 \times 1''.4$ . The (0,0) position is listed in Table 2. Velocity is relative to  $110.535 \text{ GHz}$  ( $c z_{\text{lsr}} = 12846 \text{ km s}^{-1}$ ). *right*: — Ring/disk model with the parameters listed in the Tables. Contours and resolution are the same as for the observed data at the left.

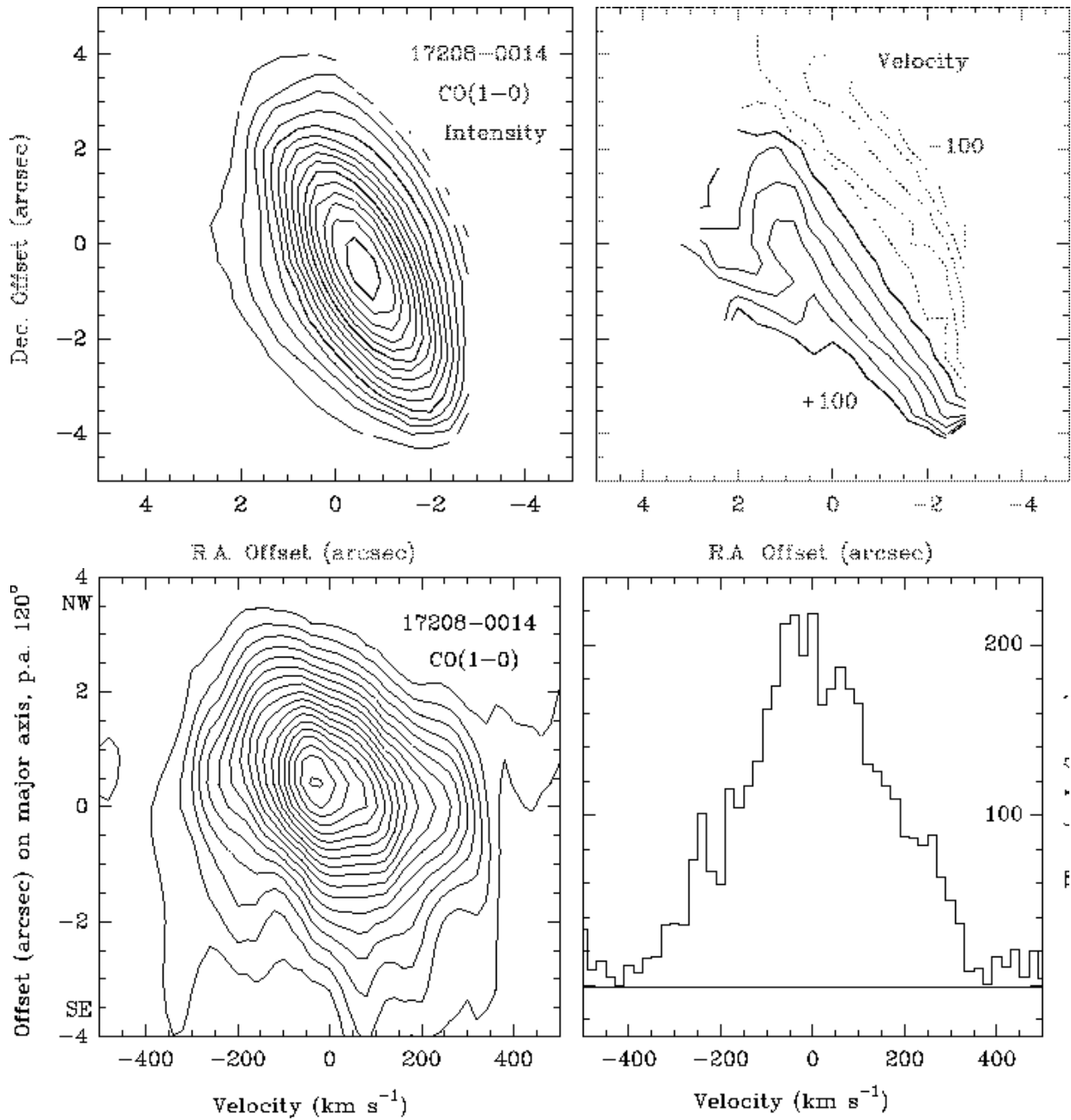


Fig. 30.— **17208-0014** : *upper left*: CO(1-0) integrated over  $(-360, +360 \text{ km s}^{-1})$ . Beam =  $5''.1 \times 1''.6$ . Contour step =  $5 \text{ Jy beam}^{-1} \text{ km s}^{-1}$ , with  $T_b/S = 12 \text{ K/Jy}$ . *upper right*: CO velocity contours in steps of  $20 \text{ km s}^{-1}$ . Labels are in  $\text{km s}^{-1}$ . *lower left*: CO(1-0) position-velocity diagram at p.a.  $120^\circ$ . Contours: 10 to 180, in steps of  $10 \text{ mJy beam}^{-1}$ , with  $T_b/S = 12 \text{ K/Jy}$ . *lower right*: CO spectrum in the  $5''.1 \times 1''.6$  beam at the source peak (Table 2). Position offsets are relative to  $17^{\text{h}}23^{\text{m}}21.^{\text{s}}99, -00^\circ17'00.''2$  (J2000), and velocity scales are relative to  $110.535 \text{ GHz}$  ( $c z_{\text{LSR}} = 12846 \text{ km s}^{-1}$ ).

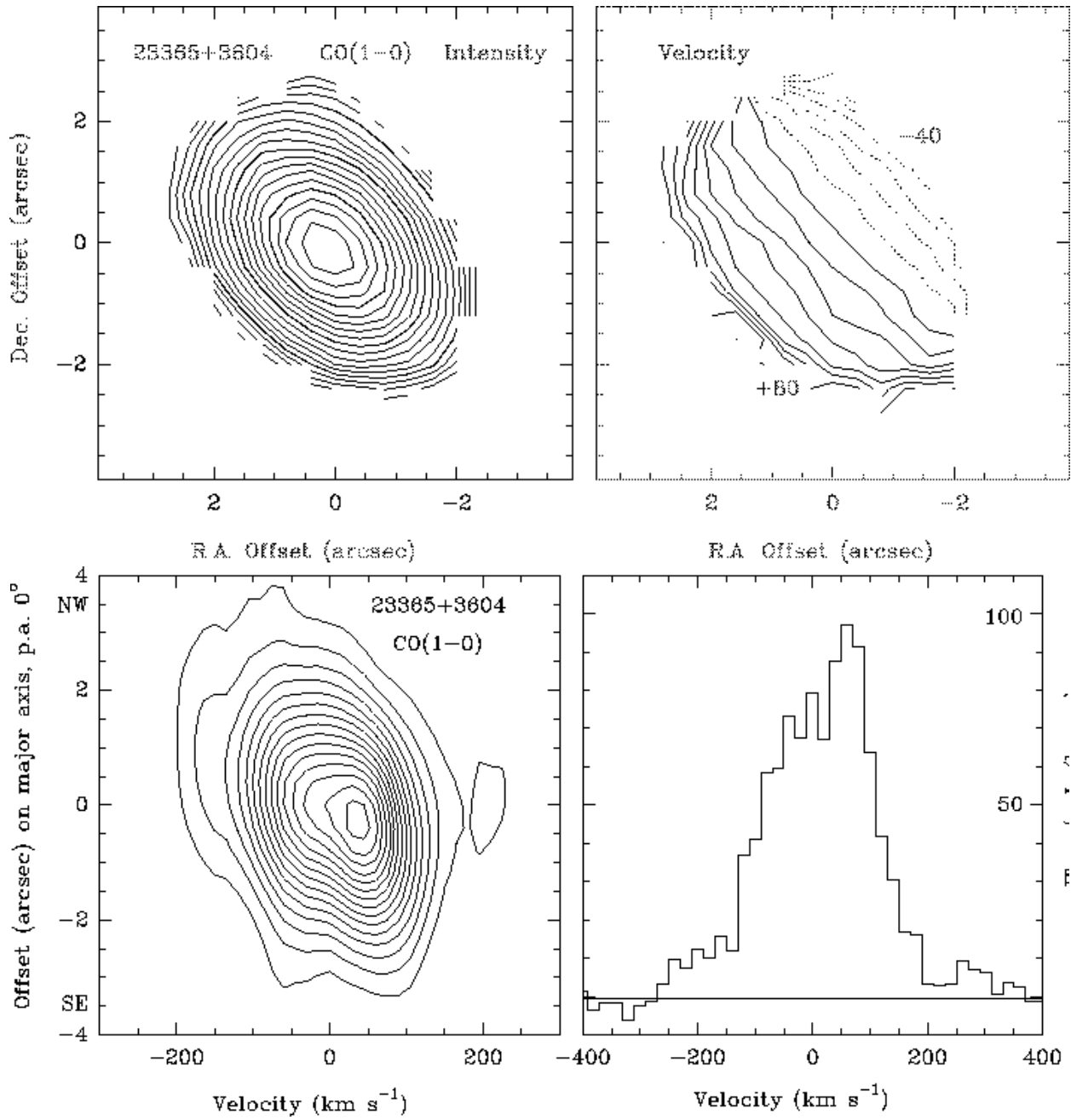


Fig. 31.— **23365+3604** : *upper left*: CO(1-0) integrated over  $(-240, +180 \text{ km s}^{-1})$ . Beam =  $3''.9 \times 2''.5$ . Contour step -  $2 \text{ Jy beam}^{-1} \text{ km s}^{-1}$ , with  $T_b/S = 11 \text{ K/Jy}$ . *upper right*: CO velocity contours in steps of  $10 \text{ km s}^{-1}$ . Labels are in  $\text{km s}^{-1}$ . *lower left*: CO(1-0) position-velocity diagram at p.a.  $135^\circ$ . Contour interval:  $3 \text{ mJy beam}^{-1}$ . *lower right*: CO spectrum at the source peak, in the  $3''.9 \times 2''.5$  beam. Position offsets are relative to  $23^{\text{h}}39^{\text{m}}01.^{\text{s}}25$ ,  $36^\circ21'08.''4$  (J2000), and velocity scales are relative to  $108.292 \text{ GHz}$  ( $c z_{\text{LSR}} = 19321 \text{ km s}^{-1}$ ).

Table 1. OBSERVING PARAMETERS

Source name	Date	Freq. (GHz)	Phase calibrator	Flux (Jy)	Clean beam (arcsec, p.a.)	Flux scale (K Jy <sup>-1</sup> )
00057+4021	06/94–11/94	110.360	0003+380	0.5	2.2 × 1.1, 47°	40
02483+4302	06/94–11/94	109.700	0234+285	1.4	2.2 × 1.7, 0°	27
VII Zw 31	03/96–05/96	109.380	0355+508	2.6	1.4 × 0.8, 58°	88
	03/96–05/96	218.650	0355+508	1.0	0.7 × 0.4, 46°	78
10565+2448	06/94–11/94	110.535	0923+392	5.5	2.3 × 1.4, 25°	32
Mrk 231	11/95–02/96	110.602	0923+392	4.4	1.3 × 1.1, 0°	70
	11/95–02/96	221.204	0923+392	2.7	0.7 × 0.5, 52°	75
Arp 193	06/96–02/98	112.641	1308+326	1.5	1.3 × 0.9, 37°	83
	05/97–02/98	225.282	1308+326	0.8	0.6 × 0.4, 33°	84
Mrk 273	03/96–05/96	111.076	1308+326	1.4	1.4 × 1.3, 116°	56
	03/96–05/96	222.176	1308+326	0.7	0.6 × 0.6, 0°	66
Arp 220	11/95–03/96	113.228	3C345	4.8	1.6 × 1.1, 25°	55
	11/95–03/96	226.422	3C345	2.4	0.7 × 0.5, 28°	69
17208–0014	06/94–10/94	110.535	1741–038	2.6	5.1 × 1.6, 47°	12
23365+3604	05/96–08/96	108.292	3C454.3	5.0	3.9 × 2.5, 45°	11

Note: The frequency is the zero of our velocity scales, not necessarily the CO line center.

Table 2. CO POSITIONS AND FLUXES

Source name	CO line	R.A. J2000 ( h m s)	Dec. J2000 ( ° ' ")	CO flux interferom. (Jy km s <sup>-1</sup> )	CO flux 30 m tel. (Jy km s <sup>-1</sup> )	Continuum freq.: flux (GHz): (mJy)
00057+4021	(1-0)	00 08 20.58	+40 37 55.5	47	45	110: < 10
02483+4302	(1-0)	02 51 36.01	+43 15 10.8	28	25	109: < 10
VII Zw 31	(1-0)	05 16 46.49	+79 40 12.6	87	92	109: < 2
	(2-1)	05 16 46.53	+79 40 12.4	135	280	219: < 10
10565+2448	(1-0)	10 59 18.15	+24 32 34.4	68	71	111: < 2
Mrk 231	(1-0)	12 56 14.21	+56 52 25.1	68	97	111: 63
	(2-1)	12 56 14.22	+56 52 25.1	276	280	221: 36
Arp 193	(1-0)	13 20 35.32	+34 08 22.2	161	162	110: < 5
disk	(2-1)	13 20 35.32	+34 08 22.2	360	—	228: 7
SE core	(2-1)	13 20 35.35	+34 08 21.7	90	—	228: 3
sum	(2-1)	—	—	450	415	228: 10
Mrk 273	(1-0)	13 44 42.12	+55 53 13.5	78	86	111: 11
disk	(2-1)	13 44 42.10	+55 53 13.4	197	—	222: < 10
core	(2-1)	13 44 42.12	+55 53 13.4	34	—	222: 8
sum	(2-1)	—	—	231	—	222: 8
Arp 220	(1-0)	15 34 57.24	+23 30 11.2	410	490	113: 41
west	(2-1)	15 34 57.221	+23 30 11.5	130	—	229: 90
east	(2-1)	15 34 57.29	+23 30 11.3	220	—	229: 30
disk	(2-1)	15 34 57.24	+23 30 11.2	750	—	229: 55
sum	(2-1)	—	—	1100	1100	229: 175
17208-0014	(1-0)	17 23 21.95	-00 17 00.7	132	162	111: < 5
23365+3604	(1-0)	23 39 01.25	+36 21 08.4	30	47	108: < 5

Errors: Positions at CO(1-0):  $\pm 0''.2$ , at CO(2-1):  $\pm 0''.1$ ; Fluxes:  $\pm 20\%$ ;

Table 3. MEASURED DIAMETERS OF THE *INTEGRATED* CO EMISSION

Source name	Angular diameter (arcsec)	P.A. E of N (deg.)	Ang.size distance (Mpc)	Redshift $cz_{\text{lsr}}$ ( $\text{km s}^{-1}$ )	Linear scale ( pc/'' )	Semi-maj.axis (pc)	Semi-min.axis (pc)
00057+4021	$1.1 \times < 0.6$	–22	165	13390	802	440	<240
02483+4302	$1.8 \times 1.7$	–4	188	15419	913	820	780
VII Zw 31	$2.4 \times 2.1$	–5	196	16260	949	1140	1000
10565+2448	$1.6 \times 1.4$	–26	160	12923	776	620	540
Mrk 231	$0.9 \times 0.8$	77	157	12650	761	340	300
Arp 193–disk	$2.8 \times 0.8$	–40	90	7000	436	610	170
Arp 193–SE core	$1.1 \times 0.5$	–40	90	7000	436	240	100
Mrk 273–tail	$3.1 \times 2.8$	5	142	11324	686	1060	960
Mrk 273–disk	$0.9 \times 0.6$	18	142	11324	686	310	210
Mrk 273–core	$0.35 \times < 0.2$	76	142	11324	686	120	<69
Arp 220–disk	$2.0 \times 1.6$	50	70	5450	341	340	270
Arp 220–west	$0.31 \times 0.28$	–14	70	5340	341	53	48
Arp 220–east	$0.9 \times 0.9$	—	70	5650	341	150	150
17208–0014	$1.8 \times 1.6$	7	159	12837	771	690	620
23365+3604	$1.0 \times 0.9$	–15	231	19330	1120	560	500

Diameters are FWHM from elliptical Gaussian fits to  $u, v$  data.

Diameters:  $\pm 0''.2$  ; position angles:  $\pm 10^\circ$ .

Table 4. DISK SIZES, FROM POSITION–VELOCITY DATA

Source name	Linear scale (pc/'')	Rotation curve turnover radius $R_0$ (pc)	half-power radius $R_{1/2}$ (pc)	Outer disk boundary $R_{\max}$ (pc)	Disk thickness $H$ (pc)
00057+4021	802	240	480	1000	50
02483+4302	913	270	730	1400	54
VII Zw 31	949	290	1100	3300	58
10565+2448	776	230	700	1600	47
Mrk 231	761	75	460	1100	23
Arp 193-disk	436	220	740	1300	65
Mrk 273-disk	686	70	400	1900	42
Arp 220-disk	341	200	480	1400	80
Arp 220-west	341	35	68	—	68
Arp 220-east	341	50	110	—	80
17208–0014	771	310	540	1500	62
23365+3604	1120	340	670	2200	67

Disk thickness  $H$  is FWHM perpendicular to the equator.



Table 5. ROTATION CURVES, FROM POSITION–VELOCITY DATA

Source name	Data: line of nodes E of N p.a. (deg)	Data: apparent rotation $V_{\text{rot}} \sin i$ (km s <sup>-1</sup> )	Model: inclination 0°=face-on $i$ (deg)	Model: rotation velocity $V_{\text{rot}}$ (km s <sup>-1</sup> )	Model: turbulent velocity $\Delta V$ (km s <sup>-1</sup> )
00057+4021	135	75	20	$250 r^\beta$	$100 r^{-0.5}$
02483+4302	0	70	15	$270 r^\beta$	$40 r^{0.0}$
VII Zw 31	0	100	20	$290 r^\beta$	$30 r^{0.0}$
10565+2448	100	75	20	$220 r^\beta$	$40 r^{0.0}$
Mrk 231	90	60	10	$345 r^\beta$	$60 r^{-0.3}$
Arp 193-disk	140	175	50	$230 r^\beta$	$40 r^{0.0}$
Mrk 273-disk	90	200	45	$280 r^\beta$	$140 r^{0.0}$
Arp 220-disk	40	212	40	$330 r^\beta$	$140 r^{-0.2}$
Arp 220-west	300	103	20	$300 r^\beta$	$100 r^{-0.3}$
Arp 220-east	50	300	60	$350 r^\beta$	$100 r^{-0.3}$
17208-0014	120	130	30	$260 r^\beta$	$150 r^{-0.2}$
23365+3604	135	130	30	$260 r^\beta$	$100 r^{-0.2}$

Model rotation curve:  $\beta = 1$  for  $r < 1$  and  $\beta = 0$  for  $r \geq 1$ , and  $r = R/R_0$ , where  $R_0$  is the rotation curve turnover radius (Table 4).

Turbulent velocity  $\Delta V =$  halfwidth to  $(1/e)$  level.  $\Delta V = 0.6 \text{ FWHM} = 1.4 \sigma$ , where  $\sigma =$  1-D velocity dispersion.

Turbulent velocities are valid for  $R_0 \leq R \leq R_{\text{max}}$  (Table 4).

Table 6. MODEL TEMPERATURES AND DENSITIES

Source name	Gas kinetic temperature (K)	$\langle n(\text{H}_2) \rangle$ at $R_0$ ( $\text{cm}^{-3}$ )	$\langle n(\text{H}_2) \rangle$ outer disk ( $\text{cm}^{-3}$ )
00057+4021	72 $r^{-0.5}$	400	40
02483+4302	50 $r^{-0.5}$	250	20
VII Zw 31	50 $r^{-0.5}$	450	10
10565+2448	60 $r^{-0.5}$	1200	30
Mrk 231	100 $r^{-0.5}$	3600	60
Arp 193–disk	40 $r^{-0.5}$	550	10
Mrk 273–disk	70 $r^{-0.5}$	1800	60
Arp 220–disk	64 $r^{-0.5}$	900	30
Arp 220–west	150 $r^{-0.5}$	22000	900
Arp 220–east	100 $r^{-0.5}$	20000	900
17208–0014	70 $r^{-0.5}$	600	60
23365+3604	67 $r^{-0.5}$	200	20

In the scaling laws,  $r = R/R_0$  where  $R_0$  is the turnover radius of the rotation curve (Table 4). At large radii, we adopted minimum gas kinetic temperatures of 10 K.

Gas densities  $\langle n(\text{H}_2) \rangle$  are averaged over the inner and outer disk volumes.

Table 7. CO(1–0) LINE PARAMETERS

Source name	Model: CO(1–0) opacity at $R_0$	Model: True $T_b$ at $R_0$ (K)	Beam FWHM (arcsec)	Model: Predicted $T_b$ in beam (K)	Data: Observed $T_b$ in beam (K)
00057+4021	4.8	16	$2.2 \times 1.1$	2.7	2.4
02483+4302	9.7	11	$2.2 \times 1.7$	1.9	1.4
VII Zw 31	7.8	18	$1.4 \times 0.8$	7.2	7.4
10565+2448	9.8	36	$2.3 \times 1.4$	4.6	4.5
Mrk 231	3.4	56	$1.3 \times 1.1$	13.5	14.0
Arp 193–disk	9.9	25	$1.7 \times 1.6$	5.0	6.9
Mrk 273–disk	3.7	36	$1.4 \times 1.3$	4.8	4.5
Arp 220–disk	5.9	29	$1.6 \times 1.1$	10.2	10.2
Arp 220–west	—	50	$1.6 \times 1.1$	10	—
Arp 220–east	—	50	$1.6 \times 1.1$	10	—
17208–0014	3.9	21	$5.1 \times 1.6$	2.5	2.2
23365+3604	6.0	10	$3.9 \times 2.5$	1.0	0.8

Model CO abundance:  $X_{\text{CO}}/(dv/dr) = 8 \times 10^{-5}$ .

All brightness temperatures are Rayleigh-Jeans.

Table 8. CO(2–1) LINE PARAMETERS

Source name	Model: CO(2–1) opacity at $R_0$	Model: True $T_b$ at $R_0$ (K)	Beam FWHM (arcsec)	Model: Predicted $T_b$ in beam (K)	Data: Observed $T_b$ in beam (K)	Data: CO(2–1) to (1–0) ratio in 3 mm beam
VII Zw 31	25	12	$1.1 \times 0.8$	5.4	5.4	$0.7 \pm 0.2$
Mrk 231	12	51	$0.7 \times 0.5$	30.3	28.5	$1.0 \pm 0.2$
Arp 193–disk	54	13	$0.7 \times 0.6$	8.2	8.1	$0.5 \pm 0.2$
Mrk 273–disk	11	34	$0.6 \times 0.6$	14	6.6	—
Arp 220–disk	15	23	$0.7 \times 0.5$	16.6	10.0	$0.6 \pm 0.2$
Arp 220–west	17	53	$0.7 \times 0.5$	18.8	17.0	—
Arp 220–east	9	70	$0.7 \times 0.5$	9.5	9.1	—

Model CO abundance,  $X_{\text{CO}}/(dv/dr) = 8 \times 10^{-5}$ .

All brightness temperatures are Rayleigh-Jeans.

Table 9. CO(1–0) LUMINOSITY, GAS MASS, AND DYNAMICAL MASS

Source name	radius pc	$L'_{\text{CO}}$ $10^9 L_l$	$M_{\text{gas}}$ $10^9 M_{\odot}$	$M_{\text{gas}}/L'_{\text{CO}}$ $M_{\odot}/L_l$	$M_{\text{dyn}}$ $10^9 M_{\odot}$	Mass ratio $M_{\text{gas}}/M_{\text{dyn}}$	$\mu/\mu_{\text{tot}}$ max.
00057+40 to $R_1$	480	2.3	0.6	0.3	7.0	0.09	0.31
to $R_{\text{max}}$	1000	4.0	1.4	0.4	14.5	0.10	—
02483+43 to $R_1$	730	2.0	1.2	0.6	12.4	0.10	—
to $R_{\text{max}}$	1400	3.2	1.9	0.6	23.6	0.08	—
VII Zw 31 to $R_1$	1100	3.2	3.0	0.9	21.5	0.14	0.22
to $R_2$	1900	5.5	5.2	1.0	37.3	0.14	—
to $R_{\text{max}}$	3670	8.5	8.3	1.0	71.5	0.12	—
10565+24 to $R_1$	700	2.3	1.8	0.8	7.8	0.23	0.28
to $R_2$	1150	3.4	3.0	0.9	13.1	0.23	—
to $R_{\text{max}}$	1600	5.5	4.0	0.7	17.4	0.23	—
Mrk 231 to $R_1$	460	2.8	1.8	0.7	12.7	0.14	0.20
to $R_2$	850	4.2	3.1	0.7	23.1	0.13	—
to $R_{\text{max}}$	1700	5.1	4.0	0.8	31.5	0.13	—
Arp 193 to $R_1$	740	1.4	1.7	0.8	9.1	0.19	—
to $R_2$	1100	2.1	2.6	0.8	15.0	0.16	—
to $R_{\text{max}}$	1300	2.6	3.4	0.9	16.1	0.21	—
Mrk 273 to $R_1$	400	4.1	2.1	0.5	8.7	0.24	0.28
to $R_2$	900	4.6	2.7	0.6	16.2	0.17	—
to $R_{\text{max}}$	1900	5.6	5.6	1.0	34.6	0.16	—
Arp 220 west	68	0.6	0.6	1.0	1.4	0.43	—
Arp 220 east	150	0.8	1.1	1.3	3.2	0.35	—
Arp 220 disk to $R_1$	480	2.7	2.0	0.8	12.1	0.17	0.30
Arp 220 disk to $R_2$	760	3.7	3.0	0.8	19.2	0.16	—
Arp 220 total	1360	5.9	5.2	0.9	34.5	0.15	—

Table 9—Continued

Source name	radius pc	$L'_{\text{CO}}$ $10^9 L_l$	$M_{\text{gas}}$ $10^9 M_{\odot}$	$M_{\text{gas}}/L'_{\text{CO}}$ $M_{\odot}/L_l$	$M_{\text{dyn}}$ $10^9 M_{\odot}$	Mass ratio $M_{\text{gas}}/M_{\text{dyn}}$	$\mu/\mu_{\text{tot}}$ max.
17208–00 to $R_1$	540	3.3	2.4	0.7	8.5	0.28	—
to $R_{\text{max}}$	1500	5.8	6.1	1.0	23.5	0.26	—
23365+36 to $R_1$	670	3.0	1.5	0.5	10.5	0.14	—
to $R_{\text{max}}$	2200	5.4	3.8	0.7	34.5	0.11	—

$L_l \equiv \text{K km s}^{-1} \text{pc}^2$ ;  $\mu = \text{gas (H}_2 + \text{He) surface density in } M_{\odot} \text{pc}^{-2}$ ;  $\mu_{\text{tot}} = \text{gas} + \text{stars}$ ;  $\mu/\mu_{\text{tot}}$  = peak ratio in the disk.

$R_1 = R_{\text{min}} + \Delta R$  is the inner disk’s half-power radius;  $R_2 = R_{\text{min}} + 2\Delta R$  is its zero-power radius;  $R_{\text{max}}$  is the boundary of the outer disk (eq. 1; Table 4).

Table 10. CONTINUUM EMISSION

Source name	2.6 mm Predicted dust flux (mJy)	2.6 mm Observed total flux (mJy)	1.3 mm Predicted dust flux (mJy)	1.3 mm Observed total flux (mJy)	Interpretation of observed flux at 1.3 mm
00057+4021	0.9	< 10	10.1	—	—
02483+4302	0.6	< 10	6.1	—	—
VII Zw 31	0.9	< 2	17.0	< 20	—
10565+2448	2.2	< 2	24.9	—	—
Mrk 231	2.4	63	7.0	36	80% nt, 20% d
Arp 193	3.8	< 5	39	10	>90% d
Mrk 273–core	1.5	11	16	8	50% nt, 50% d
Arp 220–west	6.3	—	71	90	10% nt, 10% ff, 80% d
Arp 220–east	2.3	—	25	30	10% nt, 10% ff, 80% d
Arp 220–disk	4.8	—	54	55	10% nt, 90% d
Arp 220–total	13.4	41	150	175	15%nt, 5%ff, 80% d
17208–0014	3.5	5	40	—	—
23365+3604	1.0	< 5	11	—	—

Predicted fluxes are for the temperatures in Table 6 and dust emissivity index 1.5 .

Errors in observed fluxes:  $\pm 20\%$ ; nt = nonthermal, ff = free-free, d = dust.

Table 11. STARBURST CONSISTENCY CHECK: MASS IN GAS, NEW STARS, AND OLD BULGE STARS IN THE CENTRAL MOLECULAR DISKS

	Mrk 231 disk	Mrk 273 disk	Arp 220 disk
<i>Reference radius:</i>			
$R(\text{pc})$	460	400	480
<i>Luminosity:</i>			
$L_{\text{FIR}}(< R) (10^{12} L_{\odot})$	1.9	1.0	0.7
$L_{\text{IR}}/M_{\text{new}\star} (L_{\odot}/M_{\odot})$	500	500	300
<i>Deduced mass in new stars:</i>			
$M_{\text{new}\star}(< R) (10^9 M_{\odot})$	3.8	2.0	2.3
<i>Mass from CO model:</i>			
$M_{\text{dyn}}(< R) (10^9 M_{\odot})$	12.7	8.7	12.1
$M_{\text{gas}}(< R) (10^9 M_{\odot})$	1.8	2.1	1.9
<i>Deduced mass in old stars:</i>			
$M_{\text{old}\star}(< R) (10^9 M_{\odot})$	7.1	4.6	7.9

$L_{\text{IR}}/M_{\text{new}\star}$  = assumed luminosity-to-mass ratio in a rapid starburst.

$M_{\text{new}\star} = L_{\text{FIR}}(< R)/(L_{\text{IR}}/M_{\text{new}\star})$  = mass of new stars formed in the current starburst.

$M_{\text{old}\star} = M_{\text{dyn}} - M_{\text{gas}} - M_{\text{new}\star}$  = mass of bulge stars within  $R(\text{pc})$



Table 12. PROPERTIES OF EXTREME STARBURST REGIONS

	Arp 193 SE core	Mrk 273 core	Arp 220 west	Arp 220 east
<i>1) Reference radius:</i>				
$R(\text{pc})$	150	120	68	110
<i>2) Gas Mass:</i>				
$M_{\text{gas}}(< R) (10^9 M_{\odot})$	0.6	1.0	0.6	1.1
<i>3) Mean gas density:</i>				
$\langle N(\text{H}_2) \rangle (\text{cm}^{-3})$	$2 \times 10^3$	$5 \times 10^3$	$2 \times 10^4$	$8 \times 10^3$
<i>4) Total Mass (Gas plus stars):</i>				
$M_{\text{tot}}(< R) (10^9 M_{\odot})$	1.4	2.6	1.4	3.2
<i>5) Estimated mass in new stars:</i>				
$M_{\text{new}\star}(< R) (10^9 M_{\odot})$	0.8	1.6	0.8	2.1
<i>6) Luminosity:</i>				
$L_{\text{FIR}}(< R) (10^{12} L_{\odot})$	0.2	0.6	0.3	0.2
<i>7) Luminosity to mass ratio:</i>				
$L_{\text{FIR}}/M_{\text{new}\star} (L_{\odot}/M_{\odot})$	300	360	380	100

1) Radius from measurements (Table 3 or 4).

2)  $M_{\text{gas}} \approx 1.0L'_{\text{CO}}$  (Table 9).

3)  $\langle N(\text{H}_2) \rangle (\text{cm}^{-3}) = 0.1(M_{\text{gas}}/M_{\odot}) r_{\text{pc}}^3$  (cylinder).

4)  $M_{\text{tot}} = R\Delta V^2/G$ .

5)  $M_{\text{new}\star} = M_{\text{tot}} - M_{\text{gas}}$ .

6)  $L_{\text{IR}}/L_{\odot} = 0.13r_{\text{pc}}^2 T^4$ , with  $T$  from Table 6.

7)  $(L_{\text{FIR}}/M_{\text{new}\star})$  = luminosity-to-mass ratio of new stars formed in the current starburst.

This figure "f18a.gif" is available in "gif" format from:

<http://arxiv.org/ps/astro-ph/9806377v1>

This figure "f18b.gif" is available in "gif" format from:

<http://arxiv.org/ps/astro-ph/9806377v1>

This figure "f23a.gif" is available in "gif" format from:

<http://arxiv.org/ps/astro-ph/9806377v1>

This figure "f23b.gif" is available in "gif" format from:

<http://arxiv.org/ps/astro-ph/9806377v1>